Study of Pore Development in Silicon Oxycarbide Ceramics to Understand the Microstructural Evolution

Donald Joseph Erb

Thesis submitted to the faculty of Virginia Polytechnic Institute and State University in partial fulfillment of the requirements for the degree of

Master of Science
In
Materials Science and Engineering

Peizhen Lu, Chair
David E. Clark
Carolina Tallon Galdeano

July 27, 2018
Blacksburg, VA

Keywords: Silicon Oxycarbide, Crosslinking, Pyrolysis, Porous Ceramic, Porosity

Study of Pore Development in Silicon Oxycarbide Ceramics to Understand the Microstructural Evolution

Donald Joseph Erb

Abstract

Silicon oxycarbide (SiOC) is a polymer derived ceramic consisting of SiO_2 nanodomains, disordered carbon, and SiC crystallites. Porous SiOC has shown great promise for applications such as lithium ion battery anodes, gas separation membranes, thermal barriers, and catalyst supports. The properties and microstructure of the SiOC heavily depend on the polymer precursor and the processing conditions. In this thesis, bulk SiOC is fabricated using a base polysiloxane system with different pyrolysis atmospheres, different organic additives to change the initial polymer chemistry or architectures, and polymers with different functional groups. Porosity was introduced into the SiOC ceramics through either etching the resulting SiOC with hydrofluoric acid, removing the SiO_2 nanodomains and producing micropores (pore sizes less than 2 nm) and mesopores (pore sizes between 2 nm and 50 nm), or through selective decomposition of polymers, producing macropores (pore sizes greater than 50 nm). All of the various processing parameters had effects on the pore volume and pore size within the SiOC ceramics, which can be correlated back to differences in the microstructure during pyrolysis.

Study of Pore Development in Silicon Oxycarbide Ceramics to Understand the Microstructural Evolution

Donald Joseph Erb

General Audience Abstract

Silicon oxycarbide (SiOC) is a ceramic obtained through the heating of a polymer precursor, which undergoes partial decomposition to go from an organic polymer to an inorganic ceramic. The microstructure of SiOC is not uniform at the nanometer scale, and contains nanometer sized silicon dioxide, carbon, and silicon carbide. Porous SiOC has shown great promise in applications such as lithium ion batteries, gas separation, and thermal barriers. The microstructure, and thus the properties of the SiOC, is influenced by the initial polymer and the processing conditions. In this thesis, SiOC is fabricated using a base polysiloxane polymer using different gases during heating, different additives that change the initial polymer chemical composition or polymer shape, and polymers with different reactive groups. Porosity was introduced into the SiOC ceramics through either etching the SiOC with hydrofluoric acid, which removes the silicon dioxide and produces pores with diameters less than 20 nanometers, or through decomposition during heating of a certain polymer in a two polymer mixture, producing pores that are dozens of microns in diameter. The effects of the processing parameters on the porosity and pore size are used to understand the differences in the microstructure during pyrolysis.

Acknowledgements

I would like to acknowledge the great guidance and support of my advisor, Professor Kathy Lu. I am quite thankful to Dr. Lu for giving me the opportunity to pursue my Master degree, and appreciate all of the time and thoughtful discussions throughout my time at Virginia Tech. I would also like to thank my other committee members, Dr. David Clark and Dr. Carolina Tallon, for their help and patience.

I would like to thank my former and present colleagues: Kaustubh Bawane, Michelle Gervasio, Zhihao Hu, Hongfei Ju, Yifeng Lin, Dr. Ruixin Ma, Dr. Kaijie Ning, Dr. Kris Shen, Dr. Lixia Wang, and Ni Yang. Their help, knowledge, and companionship were greatly appreciated and made my life much easier. I would also like to extend my thanks to Dr. Thomas Staley, Dr. Carlos Suchicital, and Hesham Elmkharram for their help in training me on the various equipment in the Materials Science and Engineering (MSE) laboratories, and to Dr. Weinan Leng for his help and patience in training me to conduct nitrogen adsorption experiments.

Further, I would like to thank the MSE department for funding me as a teaching assistant, and to the entire MSE faculty and staff for their help throughout my graduate research.

Lastly, and most importantly, I would like to thank my family for their continual support and guidance throughout my life. They have helped keep me grounded in times both good and bad.

The author would like to acknowledge the financial support for this research from the National Science Foundation under grant number CMMI-1634325.

Table of Contents

List of Figures

List of Tables

1 Introduction

1.1 Polymer Derived Ceramics

Polymer derived ceramics represent a very promising category of ceramics that combine the exceptional properties of ceramic materials, such as high elastic modulus and chemical inertness, while allowing for easier processing due to the availability of liquid based processing techniques to produce the polymer precursors and lower processing temperatures [1-3]. Further, the use of preceramic polymers allows for a wide range of available ceramic systems, such as SiC, SiOC, SiCN, and SiBCN, some of which are unable to be fabricated through traditional ceramic processing techniques [1, 2].

1.2 Silicon Oxycarbide

Silicon oxycarbide (SiOC) is one type of polymer derived ceramic obtained through pyrolysis of polysiloxanes, polysilsesquioxanes, and polycarbosiloxanes [1]. SiOC is stable at high temperatures, resistant to crystallization, stable in oxidative and corrosive environments, has good mechanical properties, and can possess many functional properties such as electrical conductivity and piezoresistivity [1, 2, 4-6]. The fabrication of polymer derived SiOC ceramics is composed of three stages: the crosslinking of the polymer precursor, the polymer-to-ceramic conversion, and the high temperature phase formation.

The first stage in preparing polymer derived ceramics involves the shaping and crosslinking of the polymer precursors. The liquid precursors can be fabricated into the desired shape through traditional polymer processing techniques, such as casting, drawing, injection molding, and infiltration [2]. The shaped precursors are then cured to produce highly crosslinked polymers. The polymer precursors for SiOC were historically synthesized through sol-gel processing involving the hydrolysis and condensation of molecular precursors such as tetraethyl orthosilicate [7-9]. More recently, the use of crosslinking polymer precursors has gained significant attention, due to the ability to create dense polymers through hydrosilylation [10-14]. A polysiloxane crosslinked through hydrosilylation is shown in Fig. 1.1(a).

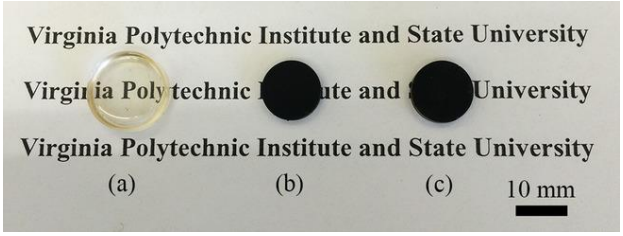

Fig. 1.1 (a) Crosslinked polysiloxane, (b) SiOC after pyrolysis, and (c) SiOC after etching with hydrofluoric acid [17]. (Reprinted from *J Am Ceram Soc*, 98, Li JK, Lu K. Highly porous SiOC bulk ceramics with water vapor assisted pyrolysis, 2357-2365, Copyright (2015), with permission from John Wiley and Sons.)

In more detail, the hydrosilylation reaction between hydrogen and vinyl bonds in organosilicon species produces carbon linkages between the silicon atoms [15, 16]. An example of the hydrosilylation reaction between a polyhydromethylsiloxane and polyvinylmethylsiloxane is shown in Fig. 1.2, which shows the two possible products from hydrosilylation. One of the most common catalysts for the hydrosilylation reaction is Karstedt's catalyst, which is a platinum catalyst and greatly favors the production of the β-product shown in Fig. 1.2 [10, 15, 16]. Other bonds that are present in the organosilicon species, such as methyl or phenyl bonds, remain unchanged during hydrosilylation and do not reduce in concentration after crosslinking [10, 15]. The advantages of using hydrosilylation over sol-gel techniques are the absence of acidic or basic chemicals, the potential to not use any solvent, and the absence of any unwanted byproducts [10].

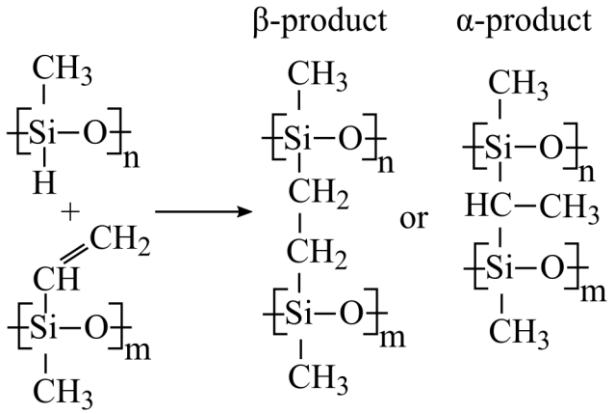

Fig. 1.2 The hydrosilylation reaction between hydrogen and vinyl bonds producing a crosslink between the two silicon atoms.

After crosslinking, the polymer precursors are heated in inert or reactive atmospheres to produce the desired ceramics in a process called pyrolysis. There are several stages of mass loss, depending on the chemical composition and side groups within the polymer. In general, at temperatures between room temperature and 400°C, no significant decomposition occurs and the only change in mass is due to additional crosslinking reactions. At temperatures between 400°C-800°C, the majority of mass loss occurs due to the release of cyclic siloxane species and hydrocarbons such as methane, ethane, ethylene, and styrene [18-20]. This release of gaseous species creates significant microporosity within the material, which is not maintained at higher temperatures due to free radical reactions on the pore surfaces resulting in viscous flow and densification of the sample [11, 21]. Above 800°C, the only mass loss is from residual hydrogen [18, 20].

The microstructure within the SiOC ceramics at pyrolysis temperatures between ~800°C-1100°C is composed of an amorphous SiOC matrix, in which Si is tetrahedrally bonded to either O or C to form SiO_xC_{4-x} bonds, and potentially a disordered carbon phase that is termed free carbon [22-24]. The specific elemental composition of the SiOC can be written as $Si_xO_yC_z$ and then plotted on a ternary elemental diagram such as that shown in Fig. 1.3 [25-27]. Although the elemental diagram is not a true phase diagram, it can be used to estimate the possible phases that can form [26]. If the composition of the SiOC phase lies on the tie line between SiO_2 and SiC, then the resulting SiOC material will be composed entirely of an amorphous SiOC phase without the presence of free carbon [8]. However, if the carbon content is significant, the resulting ceramic will be composed of both a SiOC phase and a free carbon phase. The majority of technologically significant SiOC ceramics contain an excess concentration of carbon and fall into the latter category [6, 12, 28-31].

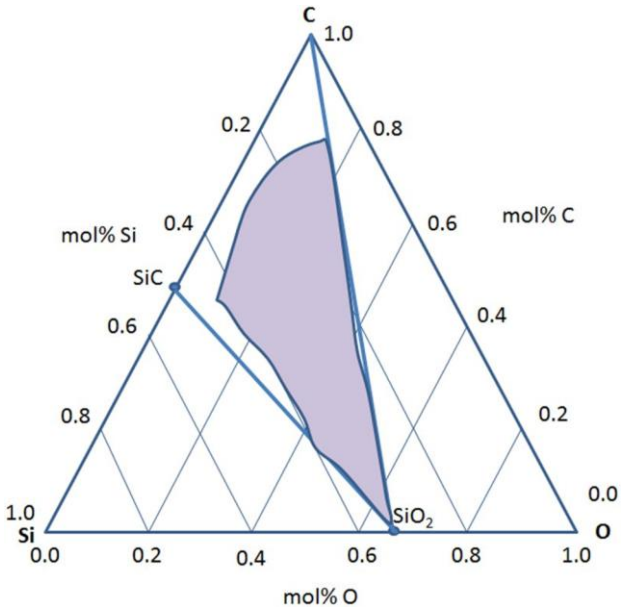

Fig. 1.3 Elemental composition diagram for the SiOC system; the shaded region represents SiOC compositions in literature [25]. (Reprinted from *Mater Sci Eng R Rep*, 97, Lu K. Porous and high surface area silicon oxycarbide-based materials – A review, 23-49, Copyright (2015), with permission from Elsevier.)

The most widely accepted description for the nanostructure of SiOC is a continuous graphitic network with SiO_2-rich nanodomains dispersed throughout. Between the graphitic and SiO_2 regions are the mixed SiO_xC_{4-x} bonds, as shown in Fig. 1.4 [27]. The proposed microstructure matches with the experimental findings for the viscoelastic behavior of SiOC, its high temperature creep resistance, and the resistance of the SiO_2 phase against crystallization at temperatures as high as 1400°C [27, 28, 32]. Further, the existence of the SiO_2 nanodomains has been confirmed through small-angle X-ray scattering and by nitrogen adsorption after selectively etching the SiO_2 phase using hydrofluoric acid [27, 33-36].

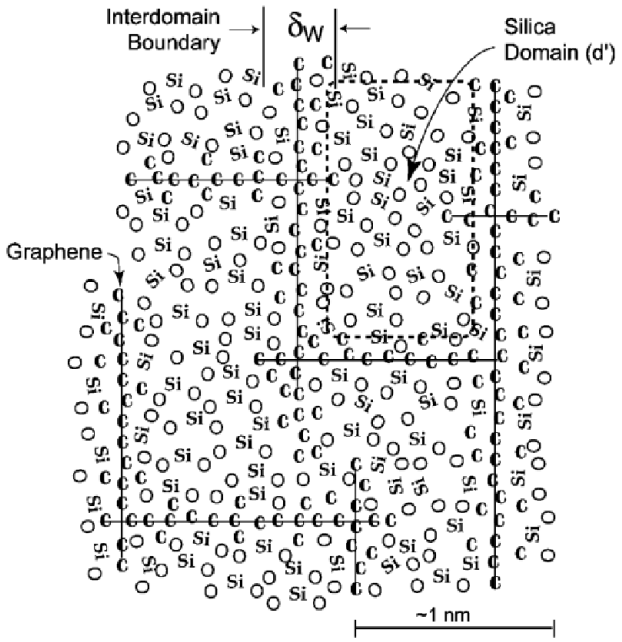

Fig. 1.4 Nanodomain model of the microstructure within SiOC [27]. (Reprinted from *J Am Ceram Soc*, 89, Saha A, Raj R, Williamson DL. A model for the nanodomains in polymer-derived SiCO, 2188-2195, Copyright (2006), with permission from John Wiley and Sons.)

At temperatures greater than ~1300°C, the SiOC phase begins to undergo phase separation into amorphous SiO_2, nanocrystalline β-SiC, and disordered carbon [23]. The SiC and carbon phase can be readily seen under TEM, as shown in Fig. 1.5, but the amorphous SiOC and SiO_2 phases cannot be distinguished. The SiO_2 phase does not crystallize, which is attributed to the presence of free carbon in the material, which hinders diffusion [23]. At temperatures above ~1400°C, the SiO_2 and carbon phases react to form SiC and gaseous byproducts [1, 23, 37].

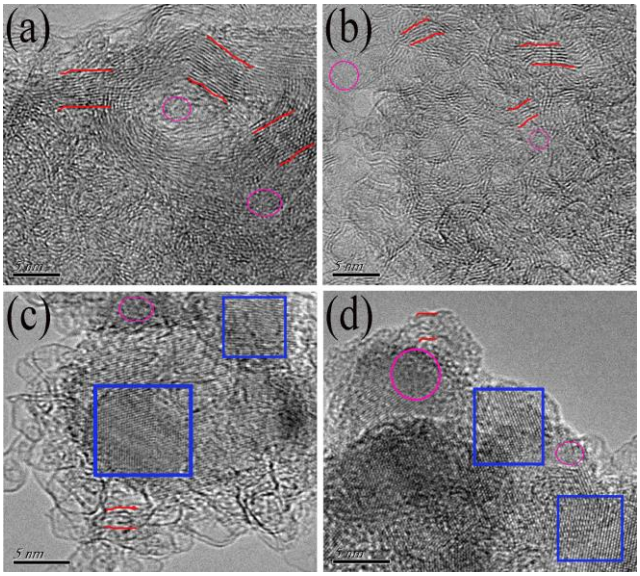

Fig. 1.5 Microstructure of SiOC showing graphitic carbon (red lines), silicon carbide (blue squares), and amorphous silicon oxycarbide (purple circles) [38]. (Reprinted from *J Eur Ceram Soc*, 34, Pan J, Pan J, Cheng X, Yan X, Lu Q, Zhang C. Synthesis of hierarchical porous silicon oxycarbide ceramics from preceramic polymer and wood biomass composites, 249-256, Copyright (2014), with permission from Elsevier.)

The phase formation within SiOC can be controlled through a number of ways. The simplest method is through varying the ratio of Si, O, and C within the polymer precursors, which effectively changes where on the elemental diagram (Fig. 1.3) the resulting SiOC ceramic will lie [37]. As already discussed, the amount of free carbon within the ceramic can be increased by moving the composition away from the SiO_2-SiC tie line [12, 28]. Further, the specific distribution of SiO_xC_{4-x} bonds can also be controlled by adjusting the composition of the starting polymer. For polymers with higher carbon concentration, the SiOC ceramic after pyrolysis contains more carbon-rich SiO_xC_{4-x} bonds [8, 24, 26, 37]. Likewise, increasing the O:Si ratio within the polymer results in more oxygen-rich bonds in the ceramic [39].

A second route to control phase formation within SiOC is through the use of reactive atmospheres during pyrolysis, such as hydrogen (H_2), ammonia (NH_3), and water vapor (H_2O), [17, 40-45]. H_2 and NH_3 are both used to remove carbon within the material during pyrolysis, resulting in pure SiOC ceramics without a free carbon phase [40, 41]. A H_2O atmosphere not only can react with carbon, but can also react with Si-C bonds within the material to form Si-O bonds. This results in

a significant reduction of SiC formation at higher pyrolysis temperatures and an increased SiO_2 content [17, 43, 44].

A third influence on the phase formation within SiOC, which has not been thoroughly studied, is the structure of the initial polymer. After pyrolysis of cyclic and linear siloxane polymers with the same chemical composition, the SiO_2 phase within the cyclic-derived SiOC partially crystallized into cristobalite while the SiO_2 remained amorphous in the linear-derived SiOC [16, 46]. The effects of other polymer architectures, such as caged or ladder structures, on the phase formation within SiOC has not been studied.

1.3 Porous Silicon Oxycarbide

Due to its high temperature stability, chemical and oxidation resistance, and good mechanical properties, porous SiOC is quite a promising material in several applications, such as anodes in lithium ion batteries, thermal barriers, filtration, and catalyst supports [3, 25]. Porosity can be introduced into the SiOC systems throughout the fabrication process, during the crosslinking of the polymer precursor, during pyrolysis, or even after pyrolysis, resulting in a high degree of control of the size and distribution of pores. Microporous (pore sizes less than 2 nm), mesoporous (pore sizes between 2 nm and 50 nm), and macroporous (pore sizes greater than 50 nm) SiOC can be produced, depending on the specific technique used. During crosslinking of the preceramic polymer, techniques such as freeze casting, foaming, and sacrificial organic additives can be used, all of which produce macropores [3, 25, 47, 48]. During pyrolysis, decomposition of a specific polymer after phase separation in a polymer blend can be used to create porosity ranging from micropores to macropores [11, 49, 50]. After pyrolysis, the SiO_2 phase can be selectively etched using HF, while the remaining SiOC, SiC, and carbon phases are resistant to HF etching [34, 51]. The pore size after etching ranges between micropores and mesopores, and is dependent on several processing parameters such as pyrolysis temperature and the SiOC composition [16, 33, 36].

The porosity produced through phase separation, introduced either by etching ceramic phases after pyrolysis or selective polymer decomposition, can also serve as a means to understand the complex microstructural evolution during pyrolysis. The SiO_2 phase can be etched using HF, leaving a porous template with pore sizes directly correlating to the original SiO_2 size, [34, 35, 46]. As previously mentioned, the pore size after HF etching, measured with nitrogen adsorption, and the

estimated size of the SiO_2 nanodomains before etching, measured with small-angle X-ray scattering, show good correlation [27, 34]. Likewise, the pores produced by polymer decomposition can be used to understand how the polymer was bonded to the matrix before decomposition [11]. Thus, by thoroughly investigating the effects of various processing parameters on the resulting pore sizes, in combination with other characterization techniques, a fundamental understanding of the microstructure evolution can be obtained to further improve the processing of SiOC ceramics.

1.4 Characterization of Porous Materials

1.4.1 Microscopy

The size and distribution of pores within materials can be qualitatively or quantitatively studied using either scanning electron microscopy (SEM) or transmission electron microscopy (TEM) depending on the pore size. For macroporous materials, pores are readily visible using SEM. If the pores and surrounding material have significant contrast differences, the pores size and pore size distribution can be obtained quantitatively using image processing software, such as ImageJ [52]. First, a threshold is applied to the original image to only select regions within a specific grey value range. Then the resulting area and diameter of each region is recorded. The pore size distribution is given as the derivative of the cumulative pore area rather than based on counts in order to more accurately reflect the contribution of each pore to the total porosity. An example of obtaining a pore size distribution from a SEM image is shown in Fig. 1.6. By repeating the process for several images of a sample, a reliable pore size distribution can be obtained.

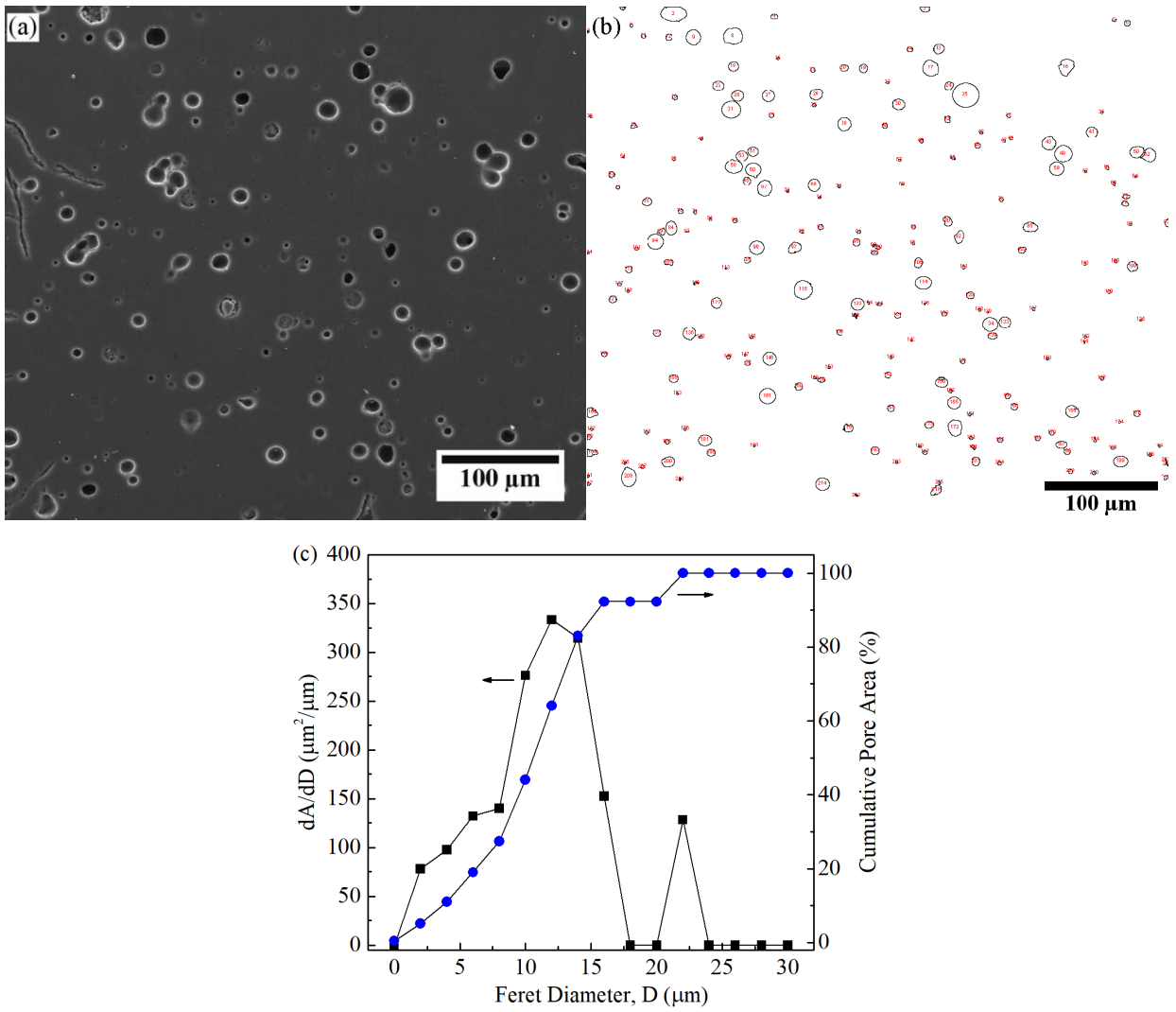

Fig. 1.6 (a) SEM image of a sample cross section, (b) the image after processing, and (c) the resulting pore size distribution and cumulative pore area.

For microporous/mesoporous SiOC materials however, obtaining usable information from microscopy images can be challenging and often misleading due to several factors. Due to the mainly amorphous microstructure of SiOC, the contrast between the SiOC matrix and any pores can be quite low. Further, since the SiOC materials are usually crushed from bulk samples for TEM imaging, the majority of the sample is too thick to image except for on the edges where the free surface may allow pores to appear larger than in the bulk of the sample. For example, in Fig. 1.7(a)-(d), the imaged samples all contain significant porosity in the micropore and mesopore range, but the pores are difficult to distinguish except in a few regions [44]. Further, although the sample in Fig. 1.7(c) seems to contain more porosity than the sample in Fig. 1.7(d), their measured

pore volumes are 0.574 cm^3/g and 1.024 cm^3/g, respectively [17]. Thus, quantification of the pore size and distribution can be quite erroneous if based off of TEM images, so TEM was not heavily used in this thesis.

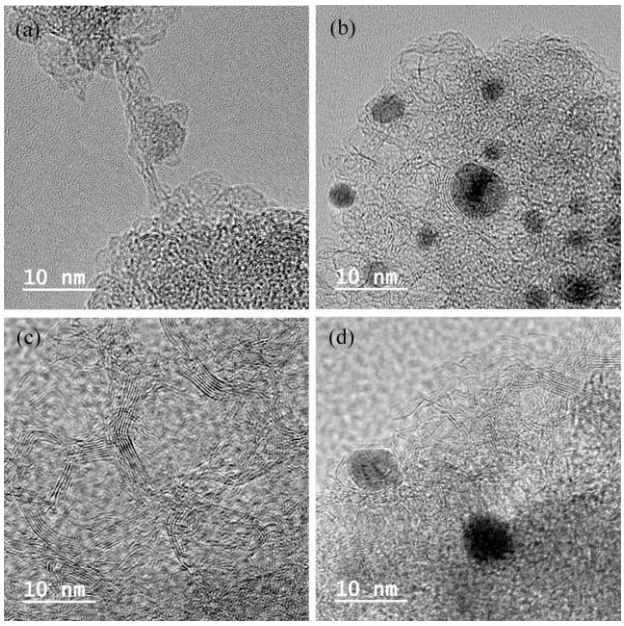

Fig. 1.7 SiOC samples with no water injection (a), water injection during 500–700 °C with no holding (b and c), and with water injection during 500–700 °C with 5 h holding (d). All the samples are etched using HF [44]. (Reprinted from *J Eur Ceram Soc*, 36, Lu K. Fundamental understanding of water vapor effect of SiOC evolution during pyrolysis, 411-422, Copyright (2016), with permission from Elsevier.)

1.4.2 Nitrogen Adsorption

Nitrogen adsorption is a popular characterization technique used to measure specific surface area, pore volume, and pore size distribution. With this technique, the sample and testing chamber are cooled to the boiling point of nitrogen (77.4 K) and nitrogen gas (N_2) is introduced, which physically adsorbs onto the sample surface. The amount of N_2 that is adsorbed onto the sample surface is measured at different relative pressures, giving information on the pore characteristics of the sample [53].

The specific surface area, with units of m^2/g, can be calculated from the nitrogen isotherms by application of the Brunauer-Emmett-Teller (BET) equation, which is given as [54]:

$$\frac{1}{W[P/P_0 - 1]} = \frac{1}{W_m C} + \frac{C - 1}{W_m C}(P/P_0) \tag{1.1}$$

where W is the adsorbed weight, W_m is the monolayer weight, P/P_0 is the relative pressure, and C is a constant that is related to the energy of adsorption. Plotting the left side of Eq. (1.1) versus the relative pressure should give a linear plot as shown in Fig. 1.8. The constant C and the monolayer weight can be calculated from the plot as [53, 54]:

$$C = \frac{s}{i} + 1 \tag{1.2}$$

$$W_m = \frac{1}{s+i} \tag{1.3}$$

where *s* is the slope of the plot and *i* is the intercept. Finally, the specific surface area, SSA, for the tested sample can be calculated [53, 54]:

$$SSA = \frac{W_m N_A A_a}{M_a} \tag{1.4}$$

where N_A is Avogadro's number (6.02×10^{23} 1/mol), A_a is the cross-sectional area of the adsorbate molecule (16.2 $Å^2$ for N_2), and M_a is the adsorbate molecular weight (28.01 g/mol for N_2) [53].

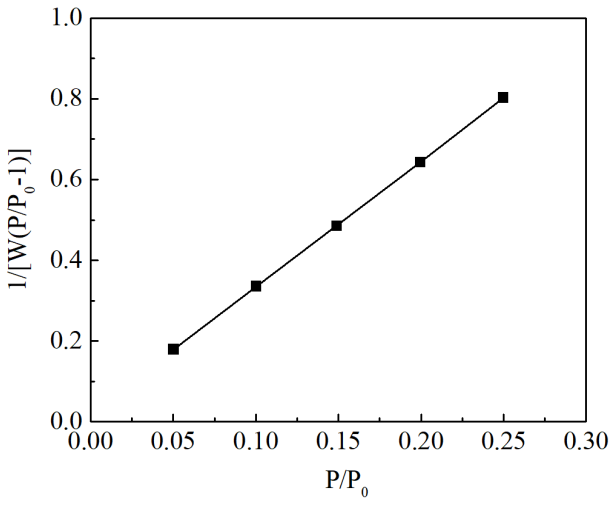

Fig. 1.8 Plot showing application of the BET equation.

The relative pressure range typically used for calculation of the specific surface area from adsorption isotherms is 0.05 – 0.30. Over this relative pressure range, the adsorbing gas molecules

should form several layers on the surface of the material according to the BET theory. If the sample contains micropores, however, the pores may be filled with the adsorbate well before reaching such large relative pressures. Use of the BET equation with microporous materials can often give negative intercepts and negative C values as a result, which have no physical meaning [53]. Thus, determining the correct relative pressure range for applying the BET equation is critical to obtain accurate values for the specific surface areas of microporous materials. Rouquerol et. al[55] proposed a method to determine the correct relative pressure range to use for microporous materials. According to this method, the specific volume adsorbed at each relative pressure is multiplied by $(1-P/P_0)$, and that quantity is plotted versus the relative pressure. The plot should reach a maximum value, which is the highest relative pressure that should be used for the BET equation [55]. An example of such a plot is shown in Fig. 1.9, and according to Rouquerol's method, the highest relative pressure to use for that sample would be 0.25.

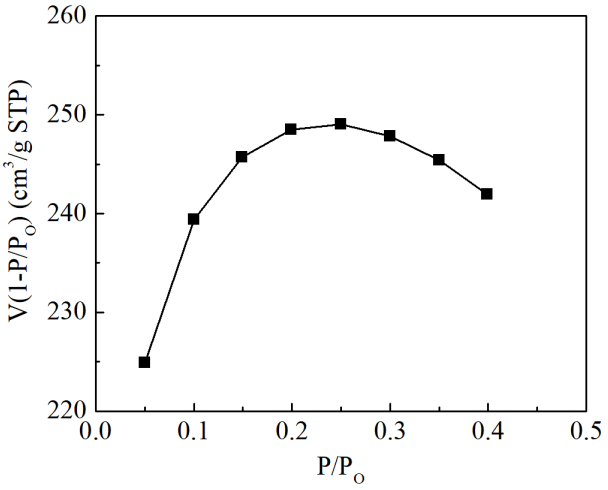

Fig. 1.9 Application of Rouquerol's method to determine the correct relative pressure range.

The pore size distribution can also be obtained from the adsorption isotherms. Traditionally, the Barrett-Joyner-Halenda (BJH) method has been used, which calculates the pore size distribution using the Kelvin equation [56]. The BJH method works well for mesoporous materials, but it cannot account for the overlapping of the surface potentials as the pore size reaches micropore size and thus underestimates the pore size [53]. In recent years, the use of theoretical models using non-local density functional theory (NLDFT) has become more available and useful

in accurately fitting the pore size distributions for porous materials containing both micropores and mesopores [53, 57].

1.5 Thesis Objectives and Overview

The overall objective of this thesis is to fabricate porous SiOC ceramics, with the pore size ranging from micropores to macropores, in order to correlate different pore characteristics to differences in the SiOC microstructural evolution. This is achieved through various studies:

i) The effects of different pyrolysis atmospheres and additives are studied for a polysiloxane (PSO). The two atmospheres used are inert argon, and an argon and water vapor mixture which will react with the polymer precursor. The different molecules added to the base PSO are polymethylphenylsiloxane, polydimethylsiloxane, polyhydromethylsiloxane, tetraethyl orthosilicate, and tetramethyl orthosilicate to vary the Si:O:C ratios in the preceramic polymer to study their effects on phase formation in SiOC. Both the atmosphere and additive effects are studied after pyrolysis at 1400°C. The SiO_2 phase is etched with hydrofluoric acid (HF) to produce micropores/mesopores and further study the SiO_2 phase size and distribution in the different ceramics.

ii) 2,4,6,8-tetramethyl-2,4,6,8-tetravinylcyclotetrasiloxane and octavinyl-polyhedral oligomeric silsesquioxane, which exhibit cyclic and caged molecular structures, respectively, are added to a base PSO to investigate the effects of the polymer architecture on the formation of SiO_2 nanodomains after pyrolysis. The SiOC ceramics are etched with HF to study the SiO_2 evolution within the ceramics as functions of both additive concentration and pyrolysis temperature.

iii) Polydimethylsiloxane (PDMS) polymers with or without vinyl bonds are added to base polymers with or without excess hydrogen bonds to study the effects of the vinyl bonds on the polymer phase separation during crosslinking and decomposition during pyrolysis. The differences in the porosity left after the PDMS decomposition reflect the differences in bonding caused by the vinyl bonds.

References

1. Colombo P, Mera G, Riedel R, Soraru GD. Polymer-derived ceramics: 40 years of research and innovation in advanced ceramics. *J Am Ceram Soc* **2010**, *93*, 1805-1837.
2. Greil P. Polymer derived engineering ceramics. *Adv Eng Mater* **2000**, *2*, 339-348.
3. Colombo P. Engineering porosity in polymer-derived ceramics. *J Eur Ceram Soc* **2008**, *28*, 1389-1395.
4. Lu K, Erb D, Liu M. Thermal stability and electrical conductivity of carbon-enriched silicon oxycarbide. *J Mater Chem C* **2016**, *4*, 1829-1837.
5. Lu K, Erb D, Liu MY. Phase transformation, oxidation stability, and electrical conductivity of TiO_2-polysiloxane derived ceramics. *J Mater Sci* **2016**, *51*, 10166-10177.
6. Roth F, Schmerbauch C, Ionescu E, Nicoloso N, Guillon O, Riedel R. High-temperature piezoresistive C/SiOC sensors. *J Sens Sens Syst* **2015**, *4*, 133-136.
7. Brequel H, Enzo S, Walter S, Soraru GD, Badheka R, Babonneau F. Structure/property relationship in silicon oxycarbide glasses and ceramics obtained via the sol-gel method. *Metastable, Mechanically Alloyed and Nanocrystalline Materials* **2002**, *386-3*, 359-364.
8. Brequel H, Parmentier J, Soraru GD, Schiffini L, Enzo S. Study of the phase separation in amorphous silicon oxycarbide glasses under heat treatment. *Nanostruct Mater* **1999**, *11*, 721-731.
9. Singh AK, Pantano CG. The role of Si-H functionality in oxycarbide glass synthesis. *Mater Res Soc Symp Proc* **1992**, *271*, 795-800.
10. Nyczyk-Malinowska A, Wojcik-Bania M, Gumula T, Hasik M, Cypryk M, Olejniczak Z. New precursors to SiCO ceramics derived from linear poly(vinylsiloxanes) of regular chain composition. *J Eur Ceram Soc* **2014**, *34*, 889-902.
11. Blum Y, Soraru GD, Ramaswamy AP, Hui D, Carturan SM. Controlled mesoporosity in SiOC via chemically bonded polymeric "spacers". *J Am Ceram Soc* **2013**, *96*, 2785-2792.
12. Blum YD, Macqueen DB, Kleebe H-J. Synthesis and characterization of carbon-enriched silicon oxycarbides. *J Eur Ceram Soc* **2005**, *25*, 143-149.
13. Gregori G, Kleebe HJ, Blum YD, Babonneau F. Evolution of C-rich SiOC ceramics - part ii. Characterization by high lateral resolution techniques: Electron energy-loss spectroscopy, high-resolution TEM and energy-filtered TEM. *Int J Mater Res* **2006**, *97*, 710-720.

14. Kleebe HJ, Gregori G, Babonneau F, Blum YD, Macqueen DB, Masse S. Evolution of C-rich SiOC ceramics - part i. Characterization by integral spectroscopic techniques: Solid-state NMR and Raman spectroscopy. *Int J Mater Res* **2006**, *97*, 699-709.
15. Sakaki S, Mizoe N, Sugimoto M. Theoretical study of platinum(0)-catalyzed hydrosilylation of ethylene. Chalk-Harrod mechanism or modified chalk-harrod mechanism. *Organometallics* **1998**, *17*, 2510-2523.
16. Dibandjo P, Dire S, Babonneau F, Soraru GD. Influence of the polymer architecture on the high temperature behavior of SiCO glasses: A comparison between linear- and cyclic-derived precursors. *J Non-Cryst Solids* **2010**, *356*, 132-140.
17. Li JK, Lu K. Highly porous SiOC bulk ceramics with water vapor assisted pyrolysis. *J Am Ceram Soc* **2015**, *98*, 2357-2365.
18. Hourlier D, Venkatachalam S, Ammar MR, Blum Y. Pyrolytic conversion of organopolysiloxanes. *J Anal Appl Pyrolysis* **2017**, *123*, 296-306.
19. Camino G, Lomakin SM, Lageard M. Thermal polydimethylsiloxane degradation. Part 2. The degradation mechanisms. *Polymer* **2002**, *43*, 2011-2015.
20. Soraru GD, Pederiva L, Latournerie M, Raj R. Pyrolysis kinetics for the conversion of a polymer into an amorphous silicon oxycarbide ceramic. *J Am Ceram Soc* **2002**, *85*, 2181-2187.
21. Wan JL, Gasch MJ, Mukherjee AK. In situ densification behavior in the pyrolysis consolidation of amorphous Si-N-C bulk ceramics from polymer precursors. *J Am Ceram Soc* **2001**, *84*, 2165-2169.
22. Brequel H, Parmentier J, Walter S, Badheka R, Trimmel G, Masse S, Latournerie J, Dempsey P, et al. Systematic structural characterization of the high-temperature behavior of nearly stoichiometric silicon oxycarbide glasses. *Chem Mater* **2004**, *16*, 2585-2598.
23. Kleebe HJ, Turquat C, Soraru GD. Phase separation in an SiCO glass studied by transmission electron microscopy and electron energy-loss spectroscopy. *J Am Ceram Soc* **2001**, *84*, 1073-1080.
24. Turquat C, Kleebe HJ, Gregori G, Walter S, Soraru GD. Transmission electron microscopy and electron energy-loss spectroscopy study of nonstoichiometric silicon-carbon-oxygen glasses. *J Am Ceram Soc* **2001**, *84*, 2189-2196.

25. Lu K. Porous and high surface area silicon oxycarbide-based materials-a review. *Mater Sci Eng R Rep* **2015**, *97*, 23-49.
26. Saha A, Raj R. Crystallization maps for SiCO amorphous ceramics. *J Am Ceram Soc* **2007**, *90*, 578-583.
27. Saha A, Raj R, Williamson DL. A model for the nanodomains in polymer-derived SiCO. *J Am Ceram Soc* **2006**, *89*, 2188-2195.
28. Kleebe HJ, Blum YD. SiOC ceramic with high excess free carbon. *J Eur Ceram Soc* **2008**, *28*, 1037-1042.
29. Martinez-Crespiera S, Ionescu E, Kleebe HJ, Riedel R. Pressureless synthesis of fully dense and crack-free SiOC bulk ceramics via photo-crosslinking and pyrolysis of a polysiloxane. *J Eur Ceram Soc* **2011**, *31*, 913-919.
30. Liu GW, Kaspar J, Reinold LM, Graczyk-Zajac M, Riedel R. Electrochemical performance of DVB-modified SiOC and SiCN polymer-derived negative electrodes for lithium-ion batteries. *Electrochim Acta* **2013**, *106*, 101-108.
31. Dibandjo P, Graczyk-Zajac M, Riedel R, Pradeep VS, Soraru GD. Lithium insertion into dense and porous carbon-rich polymer-derived SiOC ceramics. *J Eur Ceram Soc* **2012**, *32*, 2495-2503.
32. Scarmi A, Sorarù GD, Raj R. The role of carbon in unexpected visco(an)elastic behavior of amorphous silicon oxycarbide above 1273k. *J Non-Cryst Solids* **2005**, *351*, 2238-2243.
33. Biasetto L, Pena-Alonso R, Soraru GD, Colombo P. Etching of SiOC ceramic foams. *Adv Appl Ceram* **2008**, *107*, 106-110.
34. Peña-Alonso R, Sorarù GD, Raj R. Preparation of ultrathin-walled carbon-based nanoporous structures by etching pseudo-amorphous silicon oxycarbide ceramics. *J Am Ceram Soc* **2006**, *89*, 2473-2480.
35. Pena-Alonso R, Mariotto G, Gervais C, Babonneau F, Soraru GD. New insights on the high-temperature nanostructure evolution of SiOC and B-doped SiBOC polymer-derived glasses. *Chem Mater* **2007**, *19*, 5694-5702.
36. Soraru GD, Pena-Alonso R, Leoni M. C-rich micro/mesoporous Si(B)OC: In situ diffraction analysis of the HF etching process. *Microporous Mesoporous Mater* **2013**, *172*, 125-130.

37. Soraru GD, Dandrea G, Campostrini R, Babonneau F, Mariotto G. Structural characterization and high-temperature behavior of silicon oxycarbide classes prepared from sol-gel precursors containing Si-H bonds. *J Am Ceram Soc* **1995**, *78*, 379-387.
38. Pan J, Pan J, Cheng X, Yan X, Lu Q, Zhang C. Synthesis of hierarchical porous silicon oxycarbide ceramics from preceramic polymer and wood biomass composites. *J Eur Ceram Soc* **2014**, *34*, 249-256.
39. Corriu RJP, Leclercq D, Mutin PH, Vioux A. Si-29 nuclear-magnetic-resonance study of the structure of silicon oxycarbide glasses derived from organosilicon precursors. *J Mater Sci* **1995**, *30*, 2313-2318.
40. Dire S, Borovin E, Narisawa M, Soraru GD. Synthesis and characterization of the first transparent silicon oxycarbide aerogel obtained through H-2 decarbonization. *J Mater Chem A* **2015**, *3*, 24405-24413.
41. Narisawa M, Funabiki F, Iwase A, Wakai F, Hosono H. Effects of atmospheric composition on the molecular structure of synthesized silicon oxycarbides. *J Am Ceram Soc* **2015**, *98*, 3373-3380.
42. Narisawa M, Watase S, Matsukawa K, Dohmaru T, Okamura K. White Si-O-C(-H) particles with photoluminescence synthesized by decarbonization reaction on polymer precursor in a hydrogen atmosphere. *Bull Chem Soc Jpn* **2012**, *85*, 724-726.
43. Liang T, Li Y-L, Su D, Du H-B. Silicon oxycarbide ceramics with reduced carbon by pyrolysis of polysiloxanes in water vapor. *J Eur Ceram Soc* **2010**, *30*, 2677-2682.
44. Lu K, Li J. Fundamental understanding of water vapor effect on SiOC evolution during pyrolysis. *J Eur Ceram Soc* **2016**, *36*, 411-422.
45. Galusek D, Reschke S, Riedel R, Dressler W, Sajgalik P, Lencees Z, Majling J. In-situ carbon content adjustment in polysilazane derived amorphous SiCN bulk ceramics. *J Eur Ceram Soc* **1999**, *19*, 1911-1921.
46. Dibandjo P, Dire S, Babonneau F, Soraru GD. New insights into the nanostructure of high-C SiOC glasses obtained via polymer pyrolysis. *Glass Technol: Eur J Glass Sci Technol, Part A* **2008**, *49*, 175-178.
47. Vakifahmetoglu C, Zeydanli D, Innocentini MDD, Ribeiro FD, Lasso PRO, Soraru GD. Gradient-hierarchic-aligned porosity SiOC ceramics. *Sci Rep* **2017**, *7*,

48. Zeschky J, Hofner T, Arnold C, Weissmann R, Bahloul-Hourlier D, Scheffler M, Greil P. Polysilsesquioxane derived ceramic foams with gradient porosity. *Acta Mater* **2005**, *53*, 927-937.
49. Vakifahmetoglu C, Colombo P. A direct method for the fabrication of macro-porous SiOC ceramics from preceramic polymers. *Adv Eng Mater* **2008**, *10*, 256-259.
50. Yan X, Su D, Han SS. Phase separation induced macroporous SiOC ceramics derived from polysiloxane. *J Eur Ceram Soc* **2015**, *35*, 443-450.
51. Soraru GD, Modena S, Guadagnino E, Colombo P, Egan J, Pantano C. Chemical durability of silicon oxycarbide glasses. *J Am Ceram Soc* **2002**, *85*, 1529-1536.
52. Schneider CA, Rasband WS, Eliceiri KW. NIH image to ImageJ: 25 years of image analysis. *Nat Methods* **2012**, *9*, 671-675.
53. Lowell S, Shields JE, Thomas MA, Thommes M. Characterization of porous solids and powders: Surface area, pore size and density. Dordrecht, The Netherlands: Springer; 2004.
54. Brunauer S, Emmett PH, Teller E. Adsorption of gases in multimolecular layers. *J Am Chem Soc* **1938**, *60*, 309-319.
55. Rouquerol J, Llewellyn P, Rouquerol F. Is the BET equation applicable to microporous adsorbents? *Stud Surf Sci Catal* **2006**, *160*, 49-56.
56. Barrett EP, Joyner LG, Halenda PP. The determination of pore volume and area distributions in porous substances. I. Computations from nitrogen isotherms. *J Am Chem Soc* **1951**, *73*, 373-380.
57. Ravikovitch PI, Neimark AV. Characterization of nanoporous materials from adsorption and desorption isotherms. *Colloids Surf, A* **2001**, *187*, 11-21.

2 Additive and Pyrolysis Atmosphere Effects on Polysiloxane-Derived Porous SiOC Ceramics

2.1 Abstract

Porous silicon oxycarbide (SiOC) is emerging as a much superior ultrahigh surface area material that can be stable up to high temperatures with great tailorability through composition and additive modifications. In this study, bulk SiOCs were fabricated from a base polysiloxane (PSO) system by using different organic additives and pyrolysis atmospheres followed by hydrofluoric acid (HF) etching. The additives modify the microstructural evolution by influencing the SiO_2 nanodomain formation. The SiOC ceramics contain significantly less SiC and more SiO_2 with $Ar+H_2O$ atmosphere pyrolysis compared to Ar atmosphere pyrolysis. Water vapor injection during pyrolysis also causes a drastic increase in specific surface areas. The addition of 10 wt% tetraethyl orthosilicate (TEOS) with $Ar+H_2O$ pyrolysis produces a specific surface area of 1953.94 m^2/g, compared to 880.09 m^2/g for the base PSO pyrolyzed in Ar. The fundamental processes for the composition and phase evolutions are discussed as a novel pathway to creating ultrahigh surface area materials. The ability to drastically increase the specific surface area through the use of pyrolysis atmosphere and organic additives presents a promising processing route for highly porous SiOC ceramics.

2.2 Introduction

Polymer derived ceramics are a family of materials with widely tailorable properties and compositions, including SiOC, SiCN, and SiBCN, for which polymer precursors undergo thermal decomposition and bond breaking/rearrangement, resulting in amorphous or nanocrystalline ceramics, depending on the pyrolysis temperature, with a wide range of never-before properties, such as high temperature stability, oxidation resistance, and electrical conductivity [1-3]. One such system is porous SiOC, which can be used as catalyst supports, thermal barriers, gas separation membranes, and lightweight components [4]. SiOC can be fabricated with a wide range of porosity from macropores to micropores using several different processing routes such as sacrificial templating, sacrificial filler [5], direct foaming, polymer precursor phase separation [6, 7], and removal

of certain phases after pyrolysis [8]. Out of all these methods, only phase separation and/or phase removal after pyrolysis can create uniformly distributed pores with single nanometer sizes (diameter < 10 nm).

In detail, single nanometer pores resulting from phase separation can be introduced using two different methods. The first is through phase separation of the polymer precursors during crosslinking. Using immiscible polymers as precursors, it is possible to have two distinct phases after crosslinking. One of the phases then decomposes during pyrolysis, leaving behind pores. The resulting ceramics have high specific surface areas at temperatures around 600°C [6]. However, depending on the specific precursors, the specific surface area may decrease as the temperature increases above 600°C, due to the sintering of transient pores [6, 9]. The second method is by controlling the phase separation and/or crystallization during pyrolysis. At temperatures above 1100°C, the amorphous SiOC ceramic phase separates into free carbon and amorphous SiO_2 nanodomains. Annealing at higher temperatures results in further growth of the SiO_2 phase, as well as nanocrystalline SiC formation [10, 11]. If these ceramic phases can be controlled to have homogenous nucleation and growth, high concentration, and single nanometer size, they can be etched away using hydrofluoric acid (HF) or chlorine gas, respectively, leaving behind single nanometer pores [1, 12].

Controlling the chemistry of the polymer precursors can have drastic effects on the extent of phase separation during the crosslinking and pyrolysis of the SiOC. In previous studies with C-rich precursors, the resulting ceramic does not experience extensive phase separation even at high temperatures; instead the system remains mostly amorphous SiOC and free carbon [2, 13]. Alternatively, Si-rich precursors result in little to no free carbon and extensive crystallization of SiC and Si phases [10]. Turquat et al. [14] varied the Si, O, and C compositions of the polymer precursors through the use of triethoxysilane (TREOS) and dimethyldiethoxysilane (MDES). When the TREOS/MDES ratio is 1, giving a carbon rich polymer precursor, the resulting ceramic after pyrolysis and annealing at 1400°C contains only a small volume fraction of SiC; free carbon is dispersed within the amorphous SiOC. When the TREOS/MDES ratio is 9, representing a Si rich polymer, the ceramic after 1400°C annealing shows more SiC and Si nanocrystallites ranging from 20 nm to 50 nm in size. Thus, the size and amount of the nanodomains, and ultimately the pores after etching, can be controlled by varying the compositions of the precursors.

The second method to control the phases formed during pyrolysis is by introducing reactive species into the pyrolysis atmosphere, such as H_2 or H_2O [15-18]. Previous work in our lab demonstrated that injecting water vapor during the temperature range at which precursor bond (chain) breaking occurs results in a dramatic decrease in carbon precipitation and an increase in Si-O-Si bond formation [8, 17, 18]. The resulting SiOC sample pyrolyzed at 1300°C after HF etching has a specific surface area of 2391.6 m^2/g, much greater than the specific surface area of the sample pyrolyzed in Ar at the same temperature, which was 630.41 m^2/g. Liang et al. [15] investigated water vapor injection effects on the chemistry and atomic bonding of SiOC from 500°C to 1000°C. The samples pyrolyzed in the water vapor atmosphere have only about half of the carbon content compared to the samples pyrolyzed in Ar, resulting in a reduction of SiC_4 and SiC_2O_2 structural units and an increase in SiO_4 units.

In this work, micro- and meso-porous SiOC ceramics with open porosity are fabricated using different additives and pyrolysis atmospheres from polysiloxane (PSO)-based precursors. After pyrolysis, the ceramics are etched with a HF solution to create single nanometer pores. The effects of the additives and pyrolysis atmospheres on the resulting pyrolysis behavior, phase evolution, specific surface area, and pores of the SiOC ceramic are studied. The fundamental microstructural evolution mechanisms are proposed.

2.3 Experimental Procedures

A commercial polysiloxane (PSO, $[-Si(C_6H_5)_2O-]_3[-Si(CH_3)(H)O-]_2[-Si(CH_3)(CH=CH_2)O-]_2$, viscosity ~ 2-10 Pa s, SPR-684, Starfire Systems, Inc., Schenectady, NY) with alkyl, aryl, hydrogen, and vinyl side groups was chosen as the base of the precursor and 2.1-2.4% platinum-divinyltetramethyldisiloxane complex in xylene (Pt catalyst, Gelest Inc., Morrisville, PA) was used as the catalyst. The chemicals used as additives were polymethylphenylsiloxane (PMPS, $[-Si(CH_3)(C_6H_5)O-]_n$, viscosity ~ 0.45-0.55 Pa s, Sigma-Aldrich, St. Louis, MO), polydimethylsiloxane (PDMS, $[-Si(CH_3)_2O-]_n$, Sylgard 184 10:1 base to curing agent, MW ~ 60000 g/mol[19], Dow Corning, Auburn, MI), polyhydromethylsiloxane (PHMS, $[-Si(CH_3)(H)O-]_n$, MW ~ 1400-1800 g/mol, Gelest Inc., Morrisville, PA), tetraethyl orthosilicate (TEOS, $Si(OC_2H_5)_4$, Sigma-Aldrich, St. Louis, MO), and tetramethyl orthosilicate (TMOS, $Si(OCH_3)_4$, Sigma-Aldrich, St. Louis, MO).

First, PSO and one of the five additives were mixed in a 9:1 weight ratio and magnetically stirred at approximately 350 rpm for 20 minutes to form a homogeneous mixture. Next, the Pt catalyst (1 wt% relative to PSO) was added, the mixture was magnetically stirred again at 350 rpm for 5 minutes, and then poured into an aluminum foil mold. In order to reduce cracking caused by the bubbles from the mixing of the precursors, the mixture was placed into a vacuum chamber and vacuumed for 30 minutes to approximately 1500 mTorr. After that, the mixture was put in an oven to crosslink at 50°C for 12 hrs and then at 120°C for 6 hrs. The samples with either TMOS or TEOS additives initially had slightly greater than 10 wt% of the additive added in order to account for the evaporation of the additives in the vacuum chamber. The TMOS and TEOS samples were also sealed during the curing process to prevent further evaporation. The samples designated as 100PSO corresponded to the pure PSO sample; the samples with additives were labelled as 10X, where X was either PMPS, PDMS, PHMS, TEOS, or TMOS.

To prepare the samples for pyrolysis, the crosslinked polymers were first cut and polished into circular pieces roughly 10 mm in diameter and 2 mm in thickness. Next, the samples were placed into a zirconia crucible, covered on both sides with graphite mats in order to reduce friction during shrinkage and prevent warping [20, 21], and put into a tube furnace (1730-20 Horizontal Tube Furnace, CM Furnaces Inc., Bloomfield, NJ). The samples were heated up to 1400°C at a rate of 1°C/min, held for 2 hrs, cooled to 400°C with a rate of 1°C/min, and finally cooled to 50°C with a rate of 2°C/min. The Ar gas flow rate was held constant at about 500 std cm^3/min; for the samples with water vapor atmosphere, the Ar gas was bubbled through water at 60°C when the furnace was at 500°C-700°C, giving a gas flow with a Ar:H_2O molar ratio of approximately 5:1 (partial pressure of water vapor ≈ 0.2 atm). The 500°C-700°C water vapor injection temperature range was chosen because it corresponded to the temperature range at the majority of the decomposition occurs for both the base material [21] and the additives [6, 22], allowing the water vapor to penetrate the entire sample due to micropores created by the decomposition [15].

Etching of the bulk SiOC samples after pyrolysis was done using a solution of HF (20 wt% HF in water). The HF solution was magnetically stirred at room temperature until the SiOC samples had no significant mass loss, taking approximately 4 days. The SiOC samples were then rinsed with deionized water and dried at 120°C. The mass loss due to etching was calculated by dividing the change in mass after etching by the original mass.

Volumetric shrinkage and ceramic yield were calculated by measuring the dimensions and mass, respectively, of the samples before and after the pyrolysis; density was calculated by dividing the mass after pyrolysis with the measured volume and through the use of Archimedes method with ethanol as the medium. The phase compositions of the pyrolyzed samples were analyzed in an X'Pert PRO diffractometer (PANalytical B.V., EA Almelo, the Netherlands) with Cu Kα radiation. The JCPDS reference cards used to identify the crystalline phases were 00-039-1425 for SiO_2, 00-029-1129 for SiC, and 01-075-1621 for C. The chemical bonding was evaluated using Fourier Transform Infrared Spectroscopy (FT-IR) (Nicolet 8700 with Pike GladiATR attachment, Thermo Scientific, Waltham, MA), which recorded between 500 and 4000 cm^{-1} wavenumber with a resolution of 4 cm^{-1} and averaged between 64 scans; the powder samples for the FT-IR were prepared by grinding the bulk samples with a mortar and pestle. The specific surface area, pore size distribution, and pore volume of the pyrolyzed samples were evaluated using nitrogen adsorption at 77 K with a Quantachrome Autosorb-1 (Quantachrome Instruments, Boynton Beach, FL), and the samples were degassed before testing for 3 hrs at 300°C. The pore size distribution and pore volume were derived by applying the Non Local Density Functional Theory (NLDFT) to the adsorption branch of the data [23]. The partial pressure range used to calculate the BET specific surface area was selected following the guidelines established by Rouquerol et al.[24] Assuming cylindrical pores, the average pore size was estimated using 4000V/A, where V is the pore volume and A is the specific surface area [25]. The TEM sample was prepared by grinding the etched sample in a mortar and then dispersing in absolute ethanol; the microstructure was examined by a field emission analytical transmission electron microscope (JEOL 2100, JEOL USA**,** Peabody, MA).

2.4 Results and Discussion

2.4.1 Pyrolysis Behavior

The volume shrinkage, ceramic yield, and density values for the samples after pyrolysis are shown in Table 2.1. For the samples pyrolyzed in Ar, the volume shrinkage ranges from 50.19% - 56.70%, the ceramic yield ranges from 61.16% - 69.40%, and the density ranges from 1.81 g/cm^3 - 1.89 g/cm^3. Likewise, the samples pyrolyzed with water vapor have shrinkage values

from 49.33% - 53.07 %, ceramic yield values between 66.50% - 71.93%, and densities in the range of 1.75 g/cm^3 - 1.82 g/cm^3.

Table 2.1 Volume shrinkage, ceramic yield, and density of the SiOC samples after 1400°C pyrolysis.

Sample	Volumetric Shrinkage (%)		Ceramic Yield (%)		Density (g/cm^3) ± 0.02*	
	Ar	Ar + H_2O	Ar	Ar + H_2O	Ar	Ar + H_2O
100PSO	53.33 ± 1.15	53.07 ± 1.16	67.08 ± 0.71	66.71 ± 1.04	1.87	1.80
10PMPS	56.09 ± 0.62	49.33 ± 1.44	63.01 ± 1.06	66.62 ± 1.32	1.85	1.75
10PDMS	56.50 ± 1.74	52.46 ± 1.49	65.38 ± 1.97	68.39 ± 1.49	1.87	1.78
10PHMS	50.19 ± 0.64	50.63 ± 0.82	69.40 ± 2.15	71.93 ± 1.52	1.89	1.82
10TEOS	56.70 ± 1.48	50.30 ± 1.03	61.16 ± 0.30	66.50 ± 0.84	1.89	1.80
10TMOS	52.25 ± 3.34	50.43 ± 1.05	68.14 ± 4.78	71.30 ± 1.41	1.81	1.82

*Estimated error using Archimedes method.

The shrinkage and mass loss of the samples during pyrolysis are due to the release of hydrocarbons and hydrogen present in the preceramic [21]. During the pyrolysis in the Ar atmosphere, polymer preceramics containing higher amounts of hydrocarbons should experience greater shrinkage and lower ceramic yield. The volumetric shrinkage and ceramic yield values in Table 2.1 agree with this general trend. The preceramic containing the additive with the lowest hydrocarbon mass, PHMS, has the least shrinkage (50.19 %) and the highest yield (69.40 %), while the preceramic containing the additive with the highest hydrocarbon concentration, TEOS, shows the highest shrinkage (56.70 %) and the lowest yield (61.16 %). Further, the higher yield and low shrinkage for the 10PHMS sample may also arise due to reactions between the excess hydrogen bonds and either residual vinyl bonds or methyl bonds that occur between 500-700°C, forming additional Si-CH_2-Si bonds and strengthening the polymer network [26]. The volumetric shrinkage, ceramic yield, and densities for the samples are comparable to those SiOCs derived from carbon rich precursors, and the densities are lower than other carbon poor SiOC systems due to a high amount of disordered carbon (density = 1.45 g/cm^3) [17, 18, 21].

Compared to the Ar pyrolysis, the SiOC samples pyrolyzed with water vapor injection generally show less volume shrinkage, higher ceramic yield, and lower density. The decrease in shrinkage and density for the Ar+H_2O samples is due to more extensive formation of the less dense SiO_2 (density = 2.2 g/cm^3) phase rather than SiC (density = 3.2 g/cm^3). The increase in ceramic yield for the Ar+H_2O pyrolysis is due to the incorporation of more oxygen within the SiOC in place of carbon, as to be discussed in Section 2.4.2.

2.4.2 Phase Evolution

To understand the effect of the additives on the bonding differences after crosslinking, the FT-IR spectra of the crosslinked polymers are shown in Fig. 2.1. All samples show sharp peaks at approximately 695, 715, and 740 cm^{-1}, which are characteristic of silicon bonded with two phenyl side groups, found only in the base PSO, as well as a broad peak between 1000 and 1100 cm^{-1} assigned to Si-O-Si [27]. As to be explained later in Section 2.4.2, the main bonds that contribute to the reactions with water vapor are Si-H, Si-CH_3, Si-C_6H_5, Si-CH=CH_2, which are found within the base PSO and/or the additives, as well as Si-CH_2-CH_2-Si due to the hydrosilylation reaction between hydrogen and vinyl groups [28], and Si-CH_2-Si due to reactions between hydrogen, methyl, and Si-CH_2-CH_2-Si groups occurring at 500°C-700°C [26, 29].

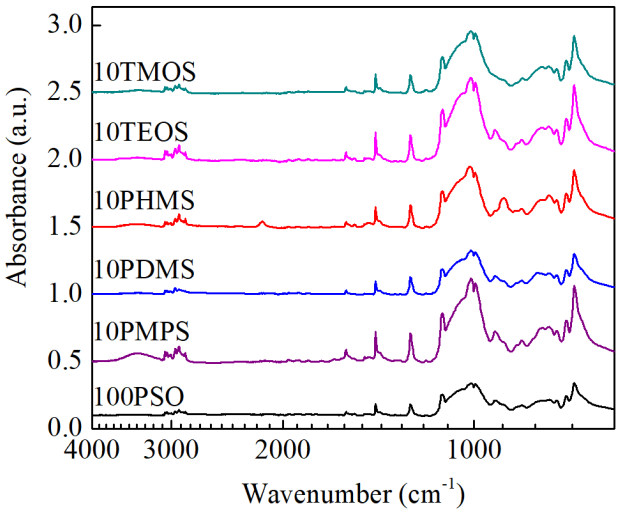

Fig. 2.1 FT-IR spectra for the polymer precursors after crosslinking.

The base PSO polymer contains equal molar amounts of hydrogen and vinyl groups, so the Si-H and Si-CH=CH_2 groups should be consumed during crosslinking [28]. Indeed, none of the polymers show the characteristic Si-H peak at 2160 cm^{-1} except for 10PHMS, due to the additional hydrogen bonds in the PHMS additive. The vinyl side group, which shows peaks at 1600 cm^{-1}, 3050 cm^{-1}, and 3070 cm^{-1} [18], is hard to distinguish for these polymers due to their overlap with the peaks of the phenyl side group; however, due to the lack of the Si-H peaks for all the samples except for the 10PHMS, it can be assumed that the majority of vinyl groups have been likewise consumed during crosslinking. Thus, the major bonds present in the samples that will react with water vapor during pyrolysis are Si-CH_3, Si-C_6H_5, Si-CH_2-CH_2-Si, and Si-CH_2-Si, as well as Si-H for the 10PHMS sample. The main bonds found in the FT-IR spectra for the polymers are summarized in Table 2.2.

Table 2.2 Major FT-IR peaks identified in the crosslinked polymers.[27, 30]

Wavenumber (cm^{-1})	Functional Group
693	Si-phenyl
715	Si-phenyl
739	Si-phenyl
950-1100	Si-O-Si
1130	Si-phenyl
1259	Si-CH_3
1426	Si-phenyl
1590	C=C in phenyl
2150	Si-H
2890-2976	C-H_x
3000-3100	C-H in phenyl
3100-3700	-OH

Fig. 2.2(a) shows the XRD patterns for the SiOC samples pyrolyzed in Ar at 1400°C. All the samples show an amorphous SiO_2 halo centered around ~23° and SiC peaks at 35.6°, 60°, and 72° [25]. In addition, all the samples exhibit a peak at ~44°, which corresponds to the (100) plane of graphite [25, 31-33]. Based on the lack of other diffraction peaks of graphite, the carbon phase can be

considered to be turbostratic carbon, in which the hexagonal graphene layers are misaligned compared to the ideal stacking in graphite [33]. The presence of the SiO_2, SiC, and carbon diffraction peaks for the samples after pyrolysis occurs due to the phase separation of SiOC, as well as the carbothermal reduction of SiO_2 into SiC. The main reactions that produce SiO_2, SiC, and C within the ceramics are given by the following reactions [11, 34]:

$$2SiOC \rightarrow SiO_2(amorphous) + SiC(\beta) + C \quad (2.1)$$

$$SiO_2(amorphous) + 3C \rightarrow SiC(\beta) + 2CO\uparrow \quad (2.2)$$

Comparison of the intensity of the SiO_2 halo to that of the SiC peak at 35.6° for each sample shows that the 10PMPS sample has the highest SiC to SiO_2 ratio with a value of 2.0, while the 10PHMS sample has the lowest with a ratio of 1.5; this result is due to the higher concentration of carbon for the 10PMPS sample, which leads to more carbothermal reduction of SiO_2.

Fig. 2.2(b) shows the XRD patterns for the SiOC samples pyrolyzed in Ar+H_2O at 1400°C. All samples show reduced SiC peaks at 35.6°, 60°, and 72° compared to the samples pyrolyzed in Ar due to the decrease of Si-C bonds in the water vapor environment [15]. With the presence of water vapor between 500°C and 700°C, the polymer to ceramic transformation occurs with the following additional possible reactions [15, 17]:

$$Si\text{-}H + H_2O \rightarrow Si\text{-}OH + H_2\uparrow \quad (2.3)$$

$$Si\text{-}CH_3 + H_2O \rightarrow Si\text{-}OH + CH_4\uparrow \quad (2.4)$$

$$Si\text{-}CH_2\text{-}Si + H_2O \rightarrow Si\text{-}OH + Si\text{-}CH_3 \quad (2.5)$$

$$Si\text{-}CH_2\text{-}CH_2\text{-}Si + 2H_2O \rightarrow 2Si\text{-}OH + C_2H_6\uparrow \quad (2.6)$$

$$Si\text{-}CH{=}CH_2 + H_2O \rightarrow Si\text{-}OH + C_2H_4\uparrow \quad (2.7)$$

$$Si\text{-}C_6H_5 + H_2O \rightarrow Si\text{-}OH + C_6H_6\uparrow \quad (2.8)$$

The Si-OH bonds further condense to form Si-O-Si bonds:

$$Si\text{-}OH + Si\text{-}OH \rightarrow Si\text{-}O\text{-}Si + H_2O\uparrow \quad (2.9)$$

In addition, free carbon that precipitates between 500°C and 700°C also oxidizes following the reaction [15, 18, 35]:

$$C_{free} + H_2O \rightarrow H_2\uparrow + CO\uparrow \quad (2.10)$$

According to Eqs. (2.3)-(2.10), water vapor facilitates Si-O bond formation while reducing Si-C bonds and consuming free carbon; the diffraction patterns in Fig. 2.2(b) for all of the samples clearly reflect this.

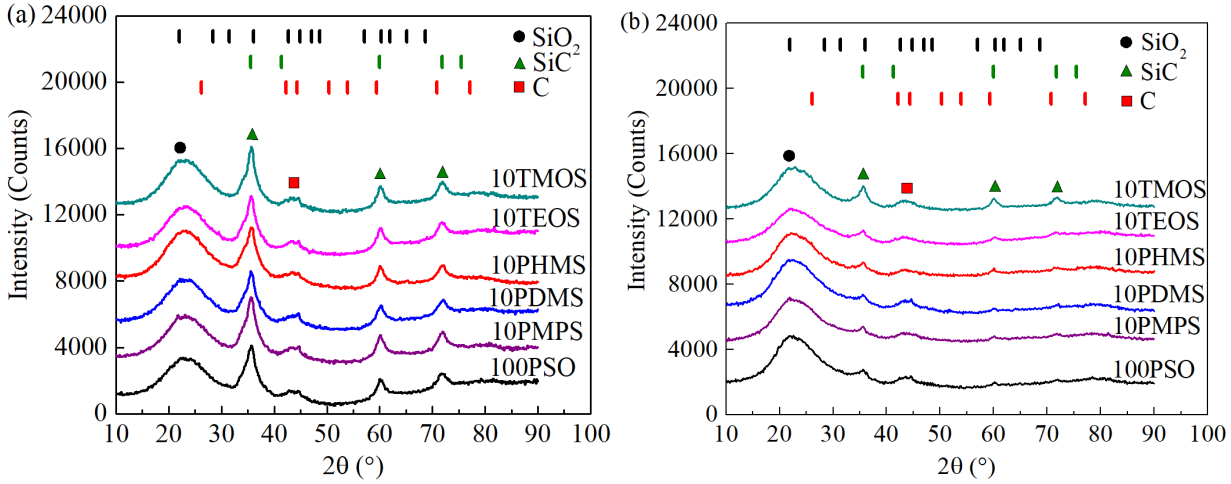

Fig. 2.2 XRD patterns for different polymer precursors after 1400°C pyrolysis in (a) Ar and (b) Ar+H_2O.

The XRD patterns for the SiOC samples pyrolyzed at 1400°C in Ar and Ar+H_2O after the HF etching are shown in Fig. 2.3(a) and Fig. 2.3(b), respectively. Dotted lines show the original position of the amorphous hump before etching. The samples no longer show the amorphous SiO_2 hump around 23°; rather, the center of the diffused peak shifts to approximately 24.5°, due to the contributions of both the remaining SiOC and the turbostratic carbon which has a peak at 26° from the (002) plane [32, 33, 36]. The etching of the SiO_2 nanodomains by the HF solution follows the reaction[18]:

$$SiO_2 + 6HF \rightarrow H_2SiF_6 + 2H_2O \quad (2.11)$$

Thus, the shift of the 23° hump in Fig. 2.3(a) and Fig. 2.3(b) signifies that the SiO_2 nanodomains are removed by HF, while the remaining SiOC, SiC, and C are largely unaffected [37]. In addition, a new diffraction peak emerges after etching at approximately 78°, which corresponds to the (110) plane of carbon [33]. The increase in the intensity of the SiC and C peaks after the HF etching, especially for the Ar+H_2O samples, is due to the removal of SiO_2 from the sample, which effectively increases the concentration of the remaining phases.

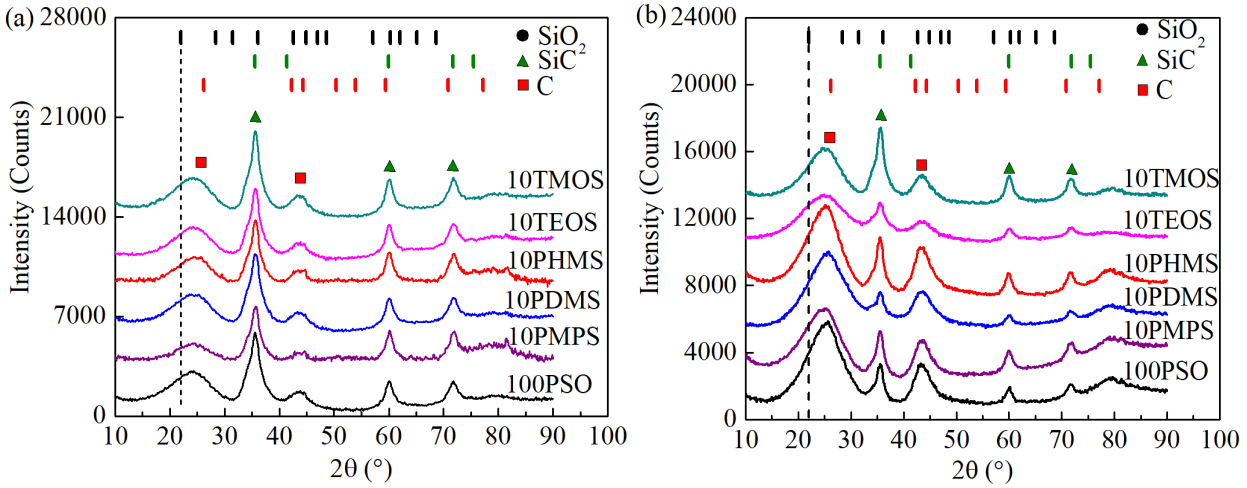

Fig. 2.3 XRD patterns after the HF etching of the SiOC samples pyrolyzed in (a) Ar and (b) Ar+H_2O.

The amount of mass loss due to the HF etching for the samples pyrolyzed in Ar and Ar+H_2O are shown in Fig. 2.4. For the samples pyrolyzed in Ar, the mass loss from the HF etching ranges from 27.7 - 39.1%. For the samples with water vapor injection, the mass loss after etching increases for all the samples and ranges from 33.9 - 62.5%. The increase in the mass loss with the water vapor atmosphere can be attributed to SiO_2 enrichment due to Si-C bonds being converted to Si-O bonds, as discussed previously. The impact is significant, up to 77% increase in the mass loss. Interestingly, the 10TMOS sample shows similar mass losses for both the Ar and Ar+H_2O atmospheres. This means that the TMOS additive does not contribute significantly to the SiO_2 formation. It is likely that the molecular mixing with the PSO precursor leads to more SiOC formation than SiO_2 formation, which is also supported by the nitrogen adsorption data in Section 2.4.3.

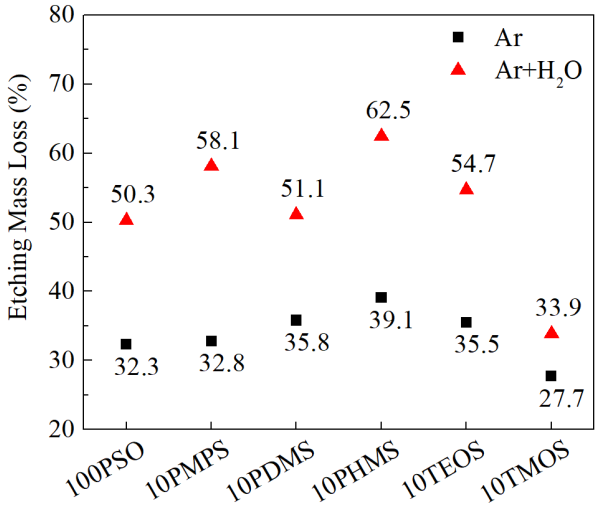

Fig. 2.4 Mass loss after the HF etching for both the Ar and Ar+H_2O pyrolysis conditions.

The FT-IR patterns for two of the SiOC samples, 100PSO and 10TMOS, after pyrolysis at 1400°C in Ar and Ar+H_2O, are shown in Fig. 2.5(a) and Fig. 2.5(b), respectively. No other samples were tested due to their similar phase behaviors with the 100PSO sample in both of the atmospheres as already seen with the XRD results in Fig. 2.2 and Fig. 2.3. Both the 100PSO and 10TMOS samples pyrolyzed in Ar show peaks around 1050 cm^{-1} and 800 cm^{-1}, corresponding to Si-O-Si and Si-C bonds, respectively [38]. The relative intensities of the peaks show no major difference between the two precursors; the 1050 cm^{-1}:800 cm^{-1} peak intensity ratio for 100PSO and 10TMOS is 1.8 and 2.1, respectively. For the pure PSO sample pyrolyzed in Ar+H_2O, there is a drastic increase in the height of the Si-O-Si peak relative to the Si-C peak compared to the sample pyrolyzed in Ar. The 10TMOS sample, however, does not show such a drastic difference between the Ar and Ar+H_2O conditions, as also seen in Fig. 2.2(b), due to a lesser extent of reaction between H_2O and the polymer. For the Ar+H_2O pyrolyzed samples, the 1050 cm^{-1}:800 cm^{-1} peak intensity ratios for 100PSO and 10TMOS are 4.2 and 3.1, respectively. After etching with HF, both samples show a drastic decrease in the Si-O-Si peak due to the HF removal of SiO_2 as explained earlier. As a matter of fact, the Si-O-Si peak for all the HF etched samples almost disappears.

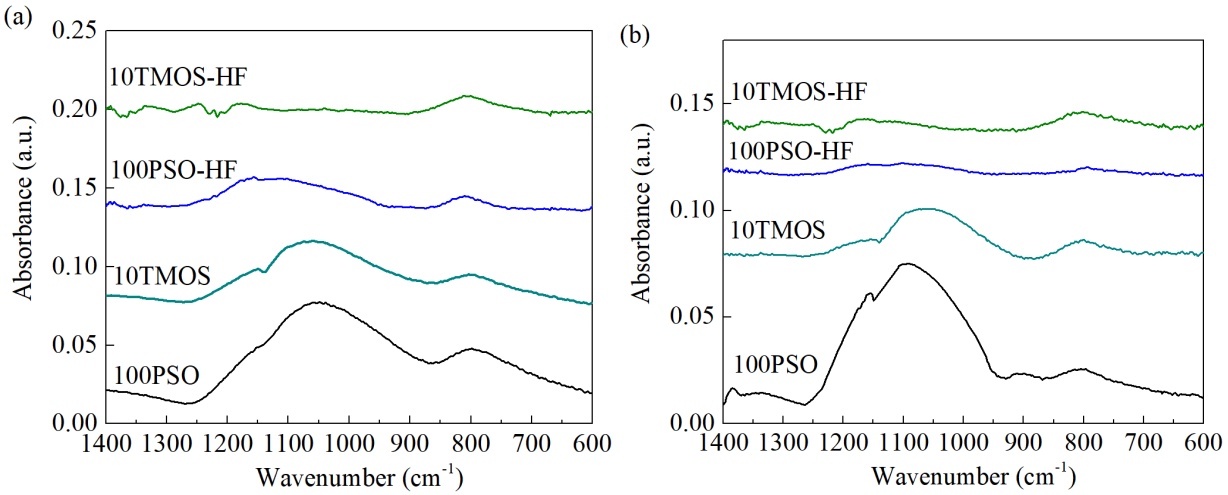

Fig. 2.5 FT-IR patterns for the SiOC samples with different additives pyrolyzed in (a) Ar and (b) Ar + H_2O before and after the HF etching.

2.4.3 Specific Surface Areas and Pores

Fig. 2.6(a) and Fig. 2.6(b) show the nitrogen adsorption curves for the samples pyrolyzed in Ar and Ar+H_2O, respectively. It should be noted that the tested samples were not powdered before testing, so all of the porosity from the HF etching is open porosity. All the samples pyrolyzed in Ar show a large adsorption volume at low relative pressures, followed by a relatively constant adsorption volume at higher relative pressures; this adsorption behavior corresponds to the Type I isotherm, according to the IUPAC classification, which indicates that the samples are prominently microporous with only monolayer adsorption [39]. The 10TMOS sample also displays more adsorption at higher relative pressures, indicative of a broader pore size distribution. In general, the adsorbed volume is from 252.8 cm^3/g to 311.4 cm^3/g at $P/P_o=1$.

For the samples pyrolyzed in Ar+H_2O, the 100PSO, 10PHMS, and 10PMPS samples display similarly large adsorption volumes at low relative pressures, followed by a further increase in adsorption at higher relative pressures due to multilayer gas adsorption. These adsorption characteristics correspond closer to the Type IV isotherm, indicative of materials containing both micropores and mesopores [39]. The 10TMOS, 10TEOS, and 10PDMS samples still display the Type I isotherm adsorption behavior after the Ar+H_2O atmosphere pyrolysis. This means that the Ar+H_2O atmosphere creates significant mesopores for the more C-rich additive systems but not for the more O-rich additives. As a result, the adsorption volume is from 324.3 cm^3/g to 662.3

cm^3/g at $P/P_o=1$, varying greatly compared to that of the Ar atmosphere pyrolyzed samples. In general, the adsorption volumes are much higher (100PSO, 10PMPS, and 10PHMS samples are more than 100% higher) than those of the samples pyrolyzed in the Ar atmosphere. Alternatively, the 10TEOS sample for the $Ar+H_2O$ condition shows a much greater adsorption volume at low relative pressures due to a large number of micropores and the volume adsorbed does not increase significantly as the relative pressure increases, indicating that mesopores are not widely present in the sample.

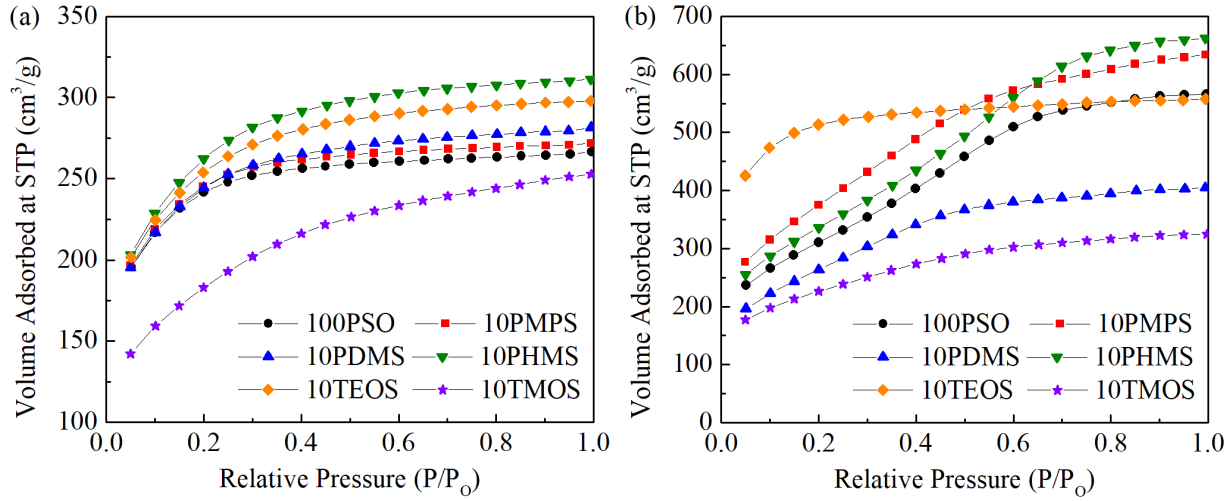

Fig. 2.6 Nitrogen adsorption curves for the samples pyrolyzed at 1400°C in (a) Ar and (b) $Ar+H_2O$.

The specific surface area, average pore size, micropore volume, and total pore volume for all of the samples in the Ar and the $Ar+H_2O$ pyrolysis atmospheres are summarized in Table 2.3.

Table 2.3 Nitrogen adsorption results for the SiOC ceramics pyrolyzed in Ar and $Ar+H_2O$ after the HF etching.

Sample	Specific surface area (m^2/g)		Micropore volume (cm^3/g)[a]		Total pore volume (cm^3/g)		Average pore size (nm)	
	Ar	$Ar+H_2O$	Ar	$Ar+H_2O$	Ar	$Ar+H_2O$	Ar	$Ar+H_2O$
100PSO	880.1	1108.5	0.39	0.75	0.39	0.84	1.77	3.03
10PMPS	892.1	1356.9	0.40	0.82	0.40	0.93	1.79	2.74
10PDMS	886.9	952.9	0.41	0.54	0.41	0.59	1.85	2.48

10PHMS	952.6	1200.0	0.45	0.86	0.45	0.98	1.89	3.27
10TEOS	921.1	1953.9	0.43	0.81	0.44	0.81	1.91	1.66
10TMOS	653.4	804.2	0.35	0.45	0.37	0.48	2.27	2.39

[a]From t-plot analysis.

For the samples pyrolyzed in Ar, the specific surface area ranges from 653.41 - 952.64 m^2/g. The addition of PMPS and PDMS has little effect on the specific surface area of the base PSO, and the addition of TEOS and PHMS increases the specific surface area slightly by 40-70 m^2/g; TMOS greatly reduces the specific surface area by ~300 m^2/g from 952.64 m^2/g to 653.41 m^2/g. Pyrolysis with water vapor, however, drastically increases the specific surface area for all the samples, with the specific surface areas ranging from 804.24 m^2/g - 1953.94 m^2/g. This means that water vapor pyrolysis can significantly facilitate the SiO_2 cluster formation during the pyrolysis and thus the resulting porous SiOC specific surface area, as to be discussed in Section 2.4.4.

After pyrolysis in Ar, the average pore sizes range from 1.77 - 2.27 nm. In general, the average pore size increases as the carbon content of the polymer precursor decreases (100PSO→10PMPS→10PDMS→10PHMS→10TEOS→10TMOS). For the Ar+H_2O atmosphere pyrolysis, all the samples except for 10TEOS experience an increase in average pore size, ranging from 1.66 - 3.27 nm. Also, the average pore size for the samples generally decreases as the precursor carbon content decreases, with the exception of the 10PHMS sample; the 10TMOS sample has similar average pore sizes for both pyrolysis conditions, and the 10TEOS sample actually experiences a decrease in the average pore size after the Ar+H_2O pyrolysis. The reason for this phenomenon can be understood as follows. During the Ar+H_2O atmosphere pyrolysis, TEOS has a high amount of Si-O bonds available to form new SiO_2 clusters independently. These SiO_2 clusters are small yet numerous in number. After the HF etching, the average pore size from the SiOC matrix-induced SiO_2 nanoclusters and the TEOS-induced SiO_2 nanoclusters is smaller than the SiO_2 size from the SiOC matrix only. This compounding effect is also reflected from the pore volume results. The pore volume for the Ar+H_2O pyrolyzed sample is higher than that for the Ar atmosphere pyrolyzed sample; it is also much higher than the pore volume with the TMOS additive. Based on these results, it can be stated that for an additive to increase the specific surface area, separate SiO_2 nucleation must be activated yet controlled so that the new SiO_2 final size is

no larger than the SiOC phase separation induced SiO_2 size. Any additive that simply facilitates the SiOC matrix-based SiO_2 formation and growth is not desired. This is conjectured to be what happens to the TMOS additive, which likely has an intimate mix with the PSO matrix. TMOS may hydrolyze (as described in Eq. (2.12)) yet cannot lead to independent SiO_2 nucleation. Subsequently, it leads to more advanced SiOC matrix-induced SiO_2 nucleation and growth. As a result, the SiO_2 nanodomain size is larger than that without TMOS, and the specific surface areas for both the Ar and Ar+H_2O atmosphere pyrolysis conditions are lower; the pore volumes are similarly smaller. In addition, the pore size distribution is wider (as seen in Fig. 2.6 and Fig. 2.7(f)).

The significant dependence of the specific surface area on the pore size can be seen by comparing the 100PSO and 10TEOS samples. Both samples have approximately the same pore volume (0.84 cm^3/g and 0.81 cm^3/g, respectively), but the specific surface areas vary significantly (1108.50 m^2/g versus 1953.94 m^2/g) due to the smaller pore size for the 10TEOS sample.

For the samples pyrolyzed in Ar, the total pore volume ranges from 0.37 cm^3/g - 0.45 cm^3/g. The micropore volumes for the Ar samples are very close to the total pore volumes, indicating that all the samples are predominantly microporous (pore size < 2 nm). For the samples with water vapor injection, the total pore volume increases for all the samples and ranges from 0.48 cm^3/g - 0.98 $cm^3/$. The micropore volumes for all of the samples with the Ar+H_2O atmosphere, except for 10TEOS, are slightly less than the total pore volume, indicating that mesopores (pore size 2 – 50 nm) are also present in the samples. The increase in total pore volume with the water vapor atmosphere can be attributed to the SiO_2 enrichment as discussed previously. The 10PHMS and 10PMPS samples have the largest pore volumes, 0.98 cm^3/g and 0.93 cm^3/g, respectively. However, the correlation of the pore volume increase after the HF etching with the additive type is a complex one because pore volume is a convoluted function of pore number density and pore size; it is also possible that some pore volume changes are not a simple result of SiO_2 removal if some C or SiOC is washed away during the HF etching due to their discontinuous distribution in the matrix [25].

Fig. 2.7 shows the pore size distributions and cumulative pore volumes for all the samples. For the additives that have the same Si/O ratio as the base PSO but different Si/C ratios (10PHMS, 10PDMS, 10PMPS), the pore size distributions for the Ar pyrolysis show that the polymers with higher carbon content (100PSO, 10PMPS) lead to narrower pore size distributions with smaller average pore sizes than the polymer with a lower carbon content (10PHMS). After the pyrolysis

in Ar, the 10PHMS sample shows a slightly broader pore size distribution with pore widths up to approximately 6 nm while the 100PSO and 10PMPS samples have no pores larger than ~4 nm. This can be explained using the nanodomain model proposed by Saha et al. [40], and experimentally shown using small angle X-ray scattering [40] and nitrogen adsorption of etched SiOC [3, 25]. According to this model, the SiO_2 clusters within the SiOC are separated by layers of turbostratic carbon. The carbon boundary layers effectively prevent nucleation and subsequently growth of the amorphous SiO_2 nanodomains by slowing diffusion [34]. Thus, the samples that are lower in carbon content (PHMS) produce larger SiO_2 domains, and larger pores after the HF etching. The effect of carbon preventing SiO_2 growth is further demonstrated from the results with water vapor pyrolysis: the 10PMPS sample again has a much narrower pore size distribution than the 10PHMS sample.

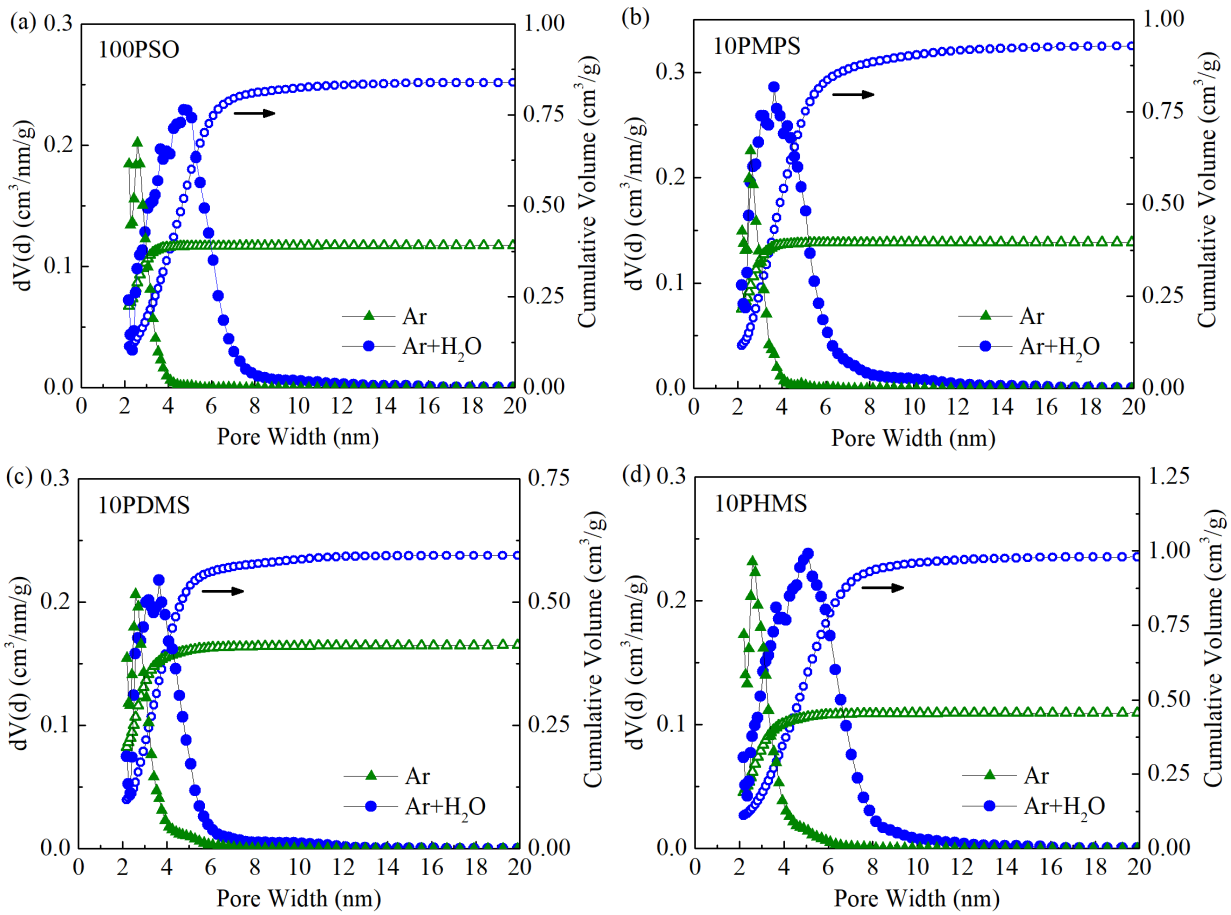

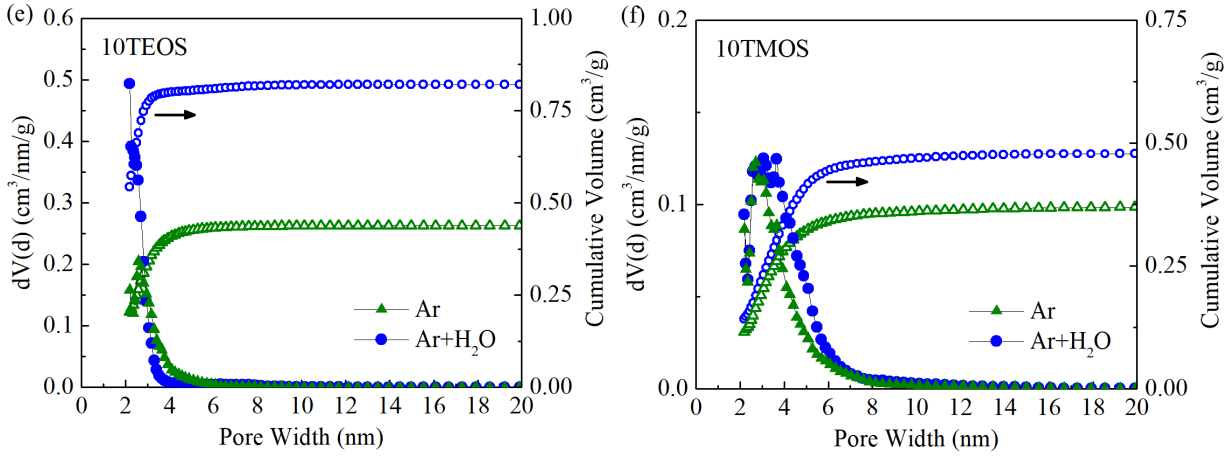

Fig. 2.7 Pore size distribution (filled symbols) and cumulative pore volume (unfilled symbols) for (a) 100PSO, (b) 10PMPS, (c) 10PDMS, (d) 10PHMS, (e) 10TEOS, and (f) 10TMOS.

From the cumulative pore volume plots in Fig. 2.7, only 10TMOS and 10TEOS show an increase in pore volume at pores < 2.1 nm from the Ar+H_2O pyrolysis compared to the Ar pyrolysis. In addition, the Ar+H_2O pyrolysis causes all the samples except for 10TEOS to have a larger average pore size and a wider pore size distribution, although the pore size distribution of the 10TMOS sample only slightly widens. This difference between the effects of the water vapor treatment on the 10TEOS and 10TMOS samples compared to the rest of the samples can be attributed to the reaction differences for these additives with water vapor. In addition to the reactions in Eqs. (2.3)-(2.8), the TEOS and TMOS additives themselves may also hydrolyze in the presence of water vapor:

$$\text{Si-O-R} + H_2O \rightarrow \text{Si-OH} + \text{ROH} \tag{2.12}$$

Where R is either CH_3 or C_2H_5. The Si-OH groups will then further condense into Si-O-Si following Eq. (2.9). This additional reaction for the 10TEOS and 10TMOS samples promotes further nucleation of SiO_2-rich regions within the samples after the Ar+H_2O pyrolysis at 700°C, which leads to a higher number of SiO_2 domains after pyrolysis at 1400°C.

The pore number density within the SiOC can be estimated using the pore volume and average pore size results. Assuming cylindrical pores, the pore density *n* is proportional to the pore volume divided by the product of the square of the average pore diameter *d* and the pore length. Further assuming that the pore length is proportional to the pore diameter, the pore number density is then given as:

$$n = C\frac{V}{d^3} \tag{2.13}$$

where C is a numerical factor that depends on the exact geometry of the pore. Since all pores in the tested samples should have approximately the same shape, the value of C will not affect the relative differences between the pore number densities for the samples. Setting C to be 1, Eq. (2.13) is plotted in Fig. 2.8 using the pore volume and average pore diameter values listed in Table 2.3. For the samples pyrolyzed in Ar, the pore number density is nearly constant for all the samples except for 10TMOS, which has approximately half the pore number density of the other samples and is consistent with our earlier conjecture that TMOS hydrolysis contributes partly to the SiOC matrix-based SiO_2 nucleation and growth. For the Ar+H_2O pyrolysis, the 100PSO, 10PMPS, 10PDMS, and 10PHMS samples all have approximately half of the pore number density of that from the Ar pyrolysis, and the 10TMOS sample shows a pore number density approximately equal to that from the Ar pyrolysis. In contrast, the 10TEOS sample after Ar+H_2O pyrolysis has a pore number density nearly three times higher than that for the Ar pyrolysis. This significant increase can be attributed to the hydrolysis of TEOS in the Ar+H_2O atmosphere according to Eq. (2.12). Interestingly, the 10TMOS sample does not show the same increase with the Ar+H_2O atmosphere although it should also hydrolyze according to (Eq. 2.12).

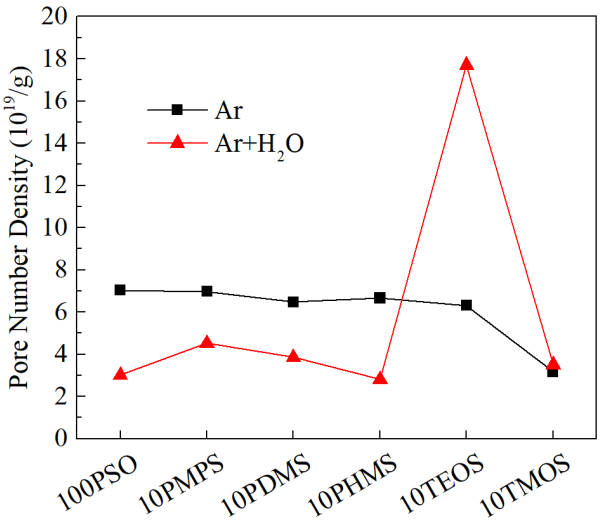

Fig. 2.8 Pore number density results calculated from Eq. (2.13) for the Ar and Ar+H_2O atmosphere pyrolyzed SiOC samples.

2.4.4 Fundamental Understanding

The effect of additives and pyrolysis atmosphere on the microstructural evolution of the SiOC is depicted in Fig. 2.9, taking into account the XRD, FT-IR, and nitrogen adsorption results. For PSO with different additives, pyrolysis in inert Ar produces very similar morphologies, with SiO_2 domains, amorphous SiOC surrounding SiO_2, and turbostratic carbon outside SiOC. The SiO_2 amount and size vary based on the additive used (as discussed in Section 2.4.3). Pyrolysis with water vapor injection, however, removes radical carbon species before they evolve into free carbon and are locked in the SiOC matrix. As a result, this reduces the turbostratic carbon layer thickness and converts more of the amorphous SiOC into SiO_2 rich domains [15]. For polymer precursors that are rich in carbon, the resulting ceramic is able to retain more of the free carbon and produce smaller sized SiO_2 domains compared to the carbon-poor samples. The addition of water-reactive species produces more SiO_2 nuclei with the water vapor pyrolysis, leading to a higher concentration of small SiO_2 domains after pyrolysis.

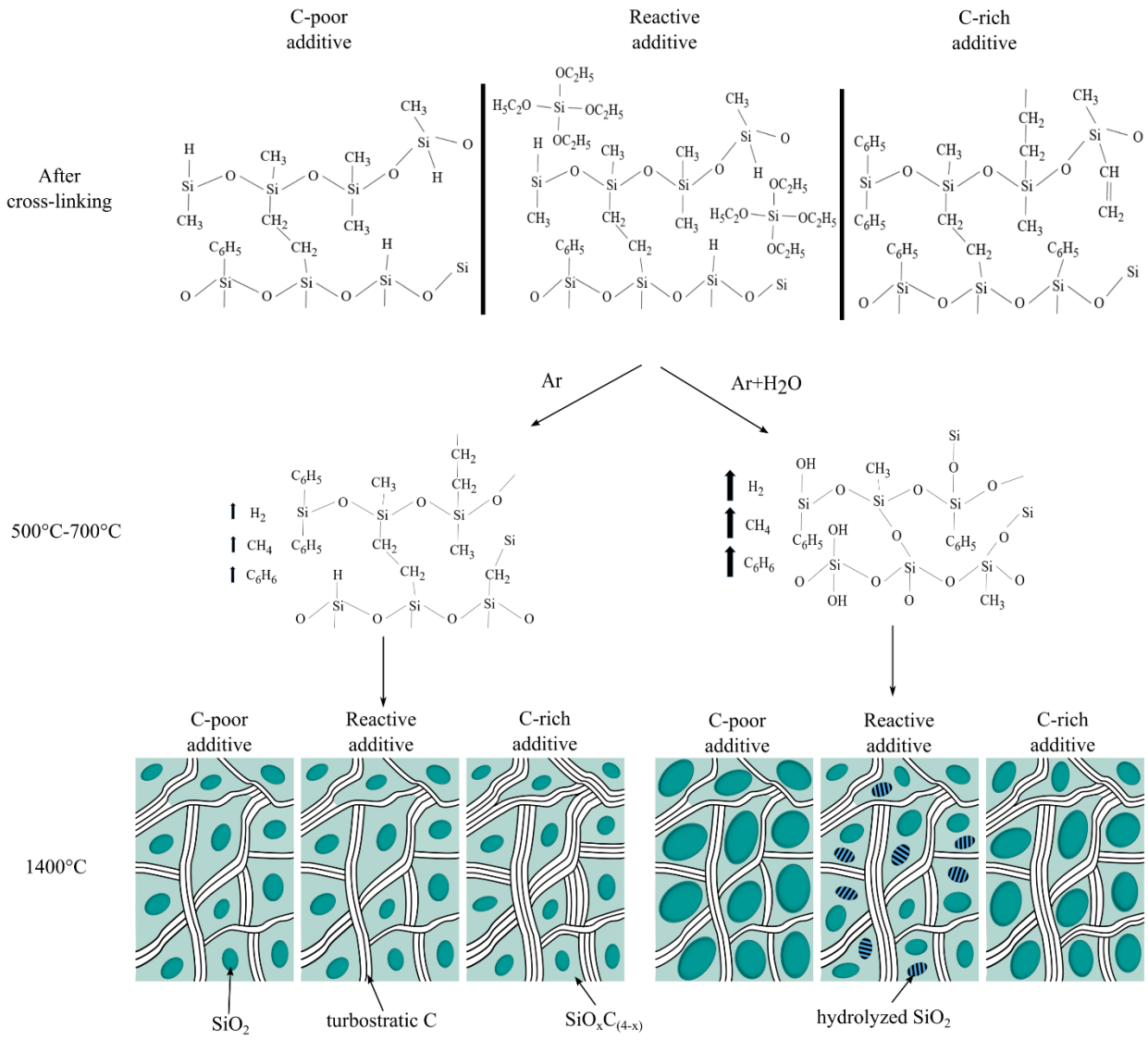

Fig. 2.9 Illustration showing the effect of additives and pyrolysis atmosphere on the microstructure of SiOC.

In the special case of the TEOS addition, TEOS itself can hydrolyze significantly and form independent SiO_2 clusters. As a result, the SiO_2 domains in the resulting SiOC matrix come from two sources: the SiOC matrix and the TEOS hydrolysis. Because of their small sizes (<2 nm), these SiO_2 nanodomains of different origins remain independent as depicted in Fig. 2.9 and lead to high specific surface areas after the HF etching. The pore morphology for the 10TEOS Ar+H_2O sample after the HF etching under TEM examination is shown in Fig. 2.10. Compared to the 100PSO sample, whose microstructure after the water vapor pyrolysis and HF etching is shown

by Lu et al.[17], the 10TEOS sample contains more numerous, small, independent pores which supports the microstructure formation shown in Fig. 2.9.

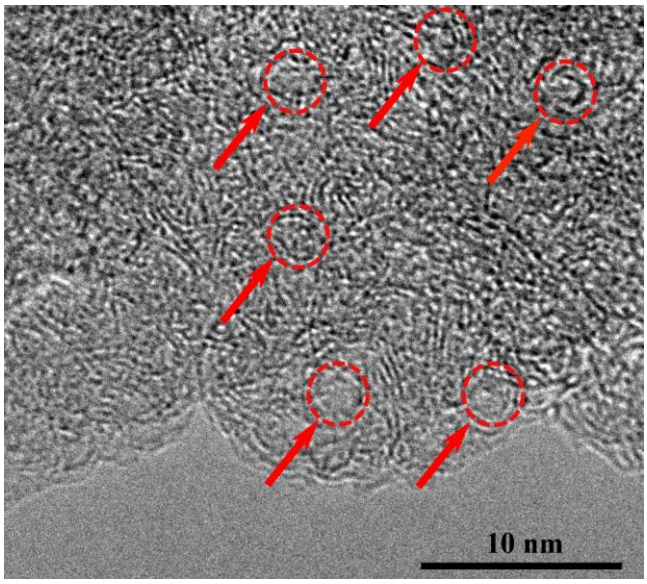

Fig. 2.10 TEM image of the 10TEOS Ar+H_2O sample after etching, with dashed circles and arrows indicating selected pores.

2.5 Conclusions

Highly porous SiOC ceramics are produced by pyrolysis in Ar and Ar+H_2O environments. The presence of water vapor during pyrolysis facilitates the formation of Si-O bonds, leading to significantly more SiO_2 after pyrolysis to 1400°C. SiO_2 formation in Ar creates an average pore size ranging from 1.77 nm to 2.27 nm. The specific surface area and pore volume values range from 653.41 m^2/g to 952.64 m^2/g and 0.37 cm^3/g to 0.45 cm^3/g, respectively. With water vapor pyrolysis, there is a significant difference in specific surface areas for different additives, ranging from 804.24 m^2/g for the 10TMOS sample to 1953.94 m^2/g for the 10TEOS sample; the average pore sizes remain in the < 4 nm range. The effects of the additives and atmosphere on the SiOC microstructural evolution are explained and the SiO_2 vs. SiC formation mechanisms are presented. The ability to drastically increase the specific surface area of the SiOC ceramics through additives and pyrolysis atmosphere presents a new and promising processing route for creating highly porous ceramics.

References

1. Colombo P, Mera G, Riedel R, Soraru GD. Polymer-derived ceramics: 40 years of research and innovation in advanced ceramics. *J Am Ceram Soc* **2010**, *93*, 1805-1837.
2. Lu K, Erb D, Liu M. Thermal stability and electrical conductivity of carbon-enriched silicon oxycarbide. *J Mater Chem C* **2016**, *4*, 1829-1837.
3. Lu K, Erb D, Liu MY. Phase transformation, oxidation stability, and electrical conductivity of TiO_2-polysiloxane derived ceramics. *J Mater Sci* **2016**, *51*, 10166-10177.
4. Juttke Y, Richter H, Voigt I, Prasad RM, Bazarjani MS, Gurlo A, Riedel R. Polymer derived ceramic membranes for gas separation. *Chem Eng Trans* **2013**, *32*, 1891-1896.
5. Li JK, Lu K, Lin TS, Shen FY. Preparation of micro-/mesoporous SiOC bulk ceramics. *J Am Ceram Soc* **2015**, *98*, 1753-1761.
6. Blum Y, Soraru GD, Ramaswamy AP, Hui D, Carturan SM. Controlled mesoporosity in SiOC via chemically bonded polymeric "spacers". *J Am Ceram Soc* **2013**, *96*, 2785-2792.
7. Colombo P. Engineering porosity in polymer-derived ceramics. *J Eur Ceram Soc* **2008**, *28*, 1389-1395.
8. Lu K. Porous and high surface area silicon oxycarbide-based materials-a review. *Mater Sci Eng R Rep* **2015**, *97*, 23-49.
9. Wan JL, Gasch MJ, Mukherjee AK. In situ densification behavior in the pyrolysis consolidation of amorphous Si-N-C bulk ceramics from polymer precursors. *J Am Ceram Soc* **2001**, *84*, 2165-2169.
10. Brequel H, Parmentier J, Soraru GD, Schiffini L, Enzo S. Study of the phase separation in amorphous silicon oxycarbide glasses under heat treatment. *Nanostruct Mater* **1999**, *11*, 721-731.
11. Saha A, Raj R. Crystallization maps for SiCO amorphous ceramics. *J Am Ceram Soc* **2007**, *90*, 578-583.
12. Biasetto L, Pena-Alonso R, Soraru GD, Colombo P. Etching of SiOC ceramic foams. *Adv Appl Ceram* **2008**, *107*, 106-110.
13. Blum YD, Macqueen DB, Kleebe H-J. Synthesis and characterization of carbon-enriched silicon oxycarbides. *J Eur Ceram Soc* **2005**, *25*, 143-149.

14. Turquat C, Kleebe HJ, Gregori G, Walter S, Soraru GD. Transmission electron microscopy and electron energy-loss spectroscopy study of nonstoichiometric silicon-carbon-oxygen glasses. *J Am Ceram Soc* **2001**, *84*, 2189-2196.
15. Liang T, Li Y-L, Su D, Du H-B. Silicon oxycarbide ceramics with reduced carbon by pyrolysis of polysiloxanes in water vapor. *J Eur Ceram Soc* **2010**, *30*, 2677-2682.
16. Narisawa M, Terauds K, Raj R, Kawamoto Y, Matsui T, Iwase A. Oxidation process of white Si-O-C(-H) ceramics with various hydrogen contents. *Scripta Mater* **2013**, *69*, 602-605.
17. Lu K, Li J. Fundamental understanding of water vapor effect on SiOC evolution during pyrolysis. *J Eur Ceram Soc* **2016**, *36*, 411-422.
18. Li JK, Lu K. Highly porous SiOC bulk ceramics with water vapor assisted pyrolysis. *J Am Ceram Soc* **2015**, *98*, 2357-2365.
19. Tsougeni K, Tserepi A, Gogolides E. Photosensitive poly(dimethylsiloxane) materials for microfluidic applications. *Microelectron Eng* **2007**, *84*, 1104-1108.
20. Janakiraman N, Aldinger F. Fabrication and characterization of fully dense Si-C-N ceramics from a poly (ureamethylvinyl) silazane precursor. *J Eur Ceram Soc* **2009**, *29*, 163-173.
21. Martinez-Crespiera S, Ionescu E, Kleebe HJ, Riedel R. Pressureless synthesis of fully dense and crack-free SiOC bulk ceramics via photo-crosslinking and pyrolysis of a polysiloxane. *J Eur Ceram Soc* **2011**, *31*, 913-919.
22. Sun JT, Huang YD, Cao HL, Gong GF. Effects of ambient-temperature curing agents on the thermal stability of poly(methylphenylsiloxane). *Polym Degrad Stab* **2004**, *85*, 725-731.
23. Ravikovitch PI, Neimark AV. Characterization of nanoporous materials from adsorption and desorption isotherms. *Colloids Surf, A* **2001**, *187*, 11-21.
24. Rouquerol J, Llewellyn P, Rouquerol F. Is the BET equation applicable to microporous adsorbents? *Stud Surf Sci Catal* **2006**, *160*, 49-56.
25. Peña-Alonso R, Sorarù GD, Raj R. Preparation of ultrathin-walled carbon-based nanoporous structures by etching pseudo-amorphous silicon oxycarbide ceramics. *J Am Ceram Soc* **2006**, *89*, 2473-2480.

26. Singh AK, Pantano CG. The role of Si-H functionality in oxycarbide glass synthesis. *Mater Res Soc Symp* Proc **1992**, *271*, 795-800.
27. Halim M, Hudaya C, Kim AY, Lee JK. Phenyl-rich silicone oil as a precursor for SiOC anode materials for long-cycle and high-rate lithium ion batteries. *J Mater Chem A* **2016**, *4*, 2651-2656.
28. Liu GW, Kaspar J, Reinold LM, Graczyk-Zajac M, Riedel R. Electrochemical performance of DVB-modified SiOC and SiCN polymer-derived negative electrodes for lithium-ion batteries. *Electrochim Acta* **2013**, *106*, 101-108.
29. Nyczyk-Malinowska A, Wojcik-Bania M, Gumula T, Hasik M, Cypryk M, Olejniczak Z. New precursors to SiCO ceramics derived from linear poly(vinylsiloxanes) of regular chain composition. *J Eur Ceram Soc* **2014**, *34*, 889-902.
30. Anderson DR. Infrared, Raman, and ultraviolet spectroscopy. In: Smith AL, editor. Analysis of silicones. Malabar, FL: Robert E. Krieger Publishing Company, Inc., 1983; p. 257-279.
31. Wilson AM, Zank G, Eguchi K, Xing W, Yates B, Dahn JR. Pore creation in silicon oxycarbides by rinsing in dilute hydrofluoric acid. *Chem Mater* **1997**, *9*, 2139-2144.
32. Pena-Alonso R, Mariotto G, Gervais C, Babonneau F, Soraru GD. New insights on the high-temperature nanostructure evolution of SiOC and B-doped SiBOC polymer-derived glasses. *Chem Mater* **2007**, *19*, 5694-5702.
33. Li ZQ, Lu CJ, Xia ZP, Zhou Y, Luo Z. X-ray diffraction patterns of graphite and turbostratic carbon. *Carbon* **2007**, *45*, 1686-1695.
34. Kleebe HJ, Turquat C, Soraru GD. Phase separation in an SiCO class studied by transmission electron microscopy and electron energy-loss spectroscopy. *J Am Ceram Soc* **2001**, *84*, 1073-1080.
35. Tobias G, Shao LD, Salzmann CG, Huh Y, Green MLH. Purification and opening of carbon nanotubes using steam. *J Phys Chem B* **2006**, *110*, 22318-22322.
36. Soraru GD, Pena-Alonso R, Leoni M. C-rich micro/mesoporous Si(B)OC: In situ diffraction analysis of the HF etching process. *Microporous Mesoporous Mater* **2013**, *172*, 125-130.
37. Soraru GD, Modena S, Guadagnino E, Colombo P, Egan J, Pantano C. Chemical durability of silicon oxycarbide glasses. *J Am Ceram Soc* **2002**, *85*, 1529-1536.

38. Yuan XY, Jin HL, Yan XB, Cheng LF, Hu LT, Xue QJ. Synthesis of ordered mesoporous silicon oxycarbide monoliths via preceramic polymer nanocasting. *Microporous Mesoporous Mater* **2012**, *147*, 252-258.
39. Sing KSW. Reporting physisorption data for gas solid systems - with special reference to the determination of surface-area and porosity. *Pure Appl Chem* **1982**, *54*, 2201-2218.
40. Saha A, Raj R, Williamson DL. A model for the nanodomains in polymer-derived SiCO. *J Am Ceram Soc* **2006**, *89*, 2188-2195.

3 Effect of Additive Structure and Size on SiO_2 Nucleation in Polymer Derived SiOC Ceramics

3.1 Abstract

Silicon oxycarbide (SiOC) ceramics with highly adjustable properties and microstructures are promising candidates for many applications such as batteries, catalysis, gas separation, and supercapacitors. In this study, additive structures on the nucleation and growth of SiO_2 within SiOC ceramics are investigated by adding cyclic tetramethyl-tetravinylcyclotetrasiloxane (TMTVS) or caged octavinyl-polyhedral oligomeric silsesquioxane (POSS) to a base polysiloxane (PSO) precursor. The effects of the two additives on the polymer-to-ceramic transformation and the phase formation within the SiOC at pyrolysis temperatures between 1100°C-1400°C are discussed. POSS encourages SiO_2 nucleation at as early as 1100°C and leads to more SiO_2 formation with significantly increased ceramic yield. High TMTVS content decreases both the specific surface area and pore volume of the resulting porous SiOCs. POSS additions of 10-40 wt% leads to slightly increased surface area. This study demonstrates a new approach of using Si-rich additive POSS to increase the SiOC yield while maintaining or even increasing the specific surface area.

3.2 Introduction

Polymer derived ceramics, such as SiOC, SiCN, and SiBCN, offer exciting properties because the microstructures and compositions of the ceramic materials can be controlled on the molecular level by focusing on the crosslinking and pyrolysis of the polymer precursors [1-3]. In particular, silicon oxycarbide, SiOC, in both bulk and porous forms, has great application potentials in batteries, catalysis, gas separation, and supercapacitors due to its high temperature stability, resistance to devitrification, and oxidation resistance [1, 4]. After pyrolysis of the preceramic polymer, SiOC is composed of mixed SiO_xC_{4-x} bonds ($0<x<4$). Upon further heating to temperatures above 1000°C, SiO_2 and free carbon form in the SiOC matrix; at temperatures above approximately 1300°C, the SiOC matrix further phase separates into additional SiO_2 and

carbon, as well as SiC nanocrystals [2, 5, 6]. The formation temperature and content of each of the phases can be controlled by tailoring the polymer precursors and pyrolysis conditions [6-10].

Several studies have been conducted on the effect of the polymer precursor architecture (e.g. linear, cyclic, cage) on the phase formation within the SiOC after pyrolysis. The effect of using a cyclic precursor, tetramethyl cyclotetrasiloxane (TMTS), versus a linear precursor, polyhydromethylsiloxane (PHMS), was investigated using either tetramethyl-tetravinylcyclotetrasiloxane[11] or divinylbenzene[12, 13] as crosslinking agents. The cyclic TMTS resulted in the formation of both crystalline and amorphous SiO_2 whereas the linear PHMS only led to amorphous SiO_2 after pyrolysis at 1400°C. For the effects of caged molecules on the pyrolysis of polymers, several studies added polyhedral oligomeric silsesquioxane (POSS) to polymer precursors for fabricating SiOC, but pyrolysis temperatures in these studies were limited to low temperatures <1100°C [14-17]. Additionally, the phase formation within the POSS-derived SiOC ceramics has not been well studied. Thus, further investigation on the effects of the POSS cage structure on the phase formation in SiOC ceramics is needed.

The formation of the SiO_2 phase within SiOC ceramics has been shown to be highly dependent on the size of the additive. SiO_2 powder with size between 15-20 nm was added to a polysiloxane (PSO) and pyrolyzed. The addition of the SiO_2 caused an increase in pore volume after etching with hydrofluoric acid. However, samples with the added SiO_2 powder also had a greater volume of pores (<10 nm in size), which could not be attributed to the added powder but rather to more extensive phase separation of the SiOC phase [18]. 10 wt% of either tetramethyl orthosilicate (TMOS) or tetraethyl orthosilicate (TEOS) was added to a base PSO and in situ hydrolyzed using water vapor injection during pyrolysis [19]. Both the TMOS and TEOS decreased the pore size after etching relative to the PSO sample, but the TMOS significantly decreased the specific surface area while the addition of TEOS increased the specific surface area. The differences between the behavior of the two additives was attributed to the size difference, with the TMOS not forming large enough SiO_2 nuclei but instead forming amorphous, HF-unetchable SiOC [19]. Thus, the size of the additive responsible for SiO_2 formation in SiOC must be properly controlled to influence the SiOC characteristics, such as yield, pore size, specific surface area, etc.

In this work, microporous SiOC ceramics are fabricated through the addition of either tetramethyl-tetravinylcyclotetrasiloxane (TMTVS) or polyhedral oligomeric silsesquioxane (POSS) to a polysiloxane-based precursor in order to investigate the effect of the additives on the

formation of SiO_2 nanodomains after pyrolysis. TMTVS has a cyclic structure, similar to the cyclic tetramethyl cyclotetrasiloxane which was previously shown to encourage SiO_2 crystallization within SiOC [11, 12, 13]. POSS has a well-defined caged structure, which may have a similar effect as cyclic structures in encouraging SiO_2 crystallization, especially considering the larger size of the caged structure. The precursors are pyrolyzed in a water vapor atmosphere, which encourages the formation of SiO_2 within the SiOC ceramics [8, 9, 19, 20]. After pyrolysis, SiO_2 nanoclusters are etched with a HF solution to create single nanometer pores, with the ultimate goal being to fabricate porous SiOC ceramics with high surface area. After pyrolysis, SiO_2 nanoclusters are etched with a HF solution to create single nanometer pores. The effects of the additive size, amount, and pyrolysis temperature on the resulting pyrolysis behavior, phase evolution, specific surface area, and pores of the SiOC ceramics are studied.

3.3 Experimental Procedures

A commercial polysiloxane (PSO, $[-Si(C_6H_5)_2O-]_3[-Si(CH_3)(H)O-]_2[-Si(CH_3)(CH=CH_2)O-]_2$, SPR-684, Starfire Systems, Inc., Gelest Inc., Schenectady, NY) was chosen as the base polymer and 2.1-2.4% platinum-divinyltetramethyldisiloxane complex in xylene (Pt catalyst, Gelest Inc., Morrisville, PA) was used as the catalyst. 2,4,6,8-tetramethyl-2,4,6,8-tetravinylcyclotetrasiloxane (TMTVS, 97%, Fisher Scientific, Pittsburgh, PA) and octavinyl-polyhedral oligomeric silsesquioxane (POSS, OL1170, Hybrid Plastics, Hattiesburg, MS) were used as additives in the base PSO, and acetone (HPLC grade, Fisher Scientific, Pittsburgh, PA) was used as the solvent.

For the solutions with TMTVS additions, PSO and TMTVS were mixed with either 0, 10, 20, 30, or 40 wt% TMTVS. Adequate acetone was added to reduce the viscosity of the solution, having approximate volume ratios of 0.2:0.8 acetone to PSO+TMTVS. The mixtures were sonicated for 10 minutes and then mixed in a high energy mill (SPEX 8000M Mixer/Mill, SPEX SamplePrep, Metuchen, NJ) for 10 minutes to form a homogeneous mixture. Next, the Pt catalyst (1 wt% relative to PSO) was added, the mixtures were mixed again in a high energy ball mill for 5 minutes, and then poured into aluminum foil molds. For solutions containing POSS, additional acetone was used to fully dissolve POSS before mixing with the PSO; the acetone to POSS volume

ratio was 5:1. PSO was then added to the solution to make 10, 20, 30, and 40 wt% POSS mixtures. All other preparation steps for the POSS mixtures were the same as for TMTVS.

Once transferred to the molds, the mixtures were placed into a vacuum chamber and vacuumed for 30 minutes at approximately 20 Torr to remove all the solvent and any bubbles from the solutions. After that, the molds were put in an oven to crosslink at 50°C for 12 hrs and then at 120°C for 6 hrs. Samples designated as PSO correspond to the pure PSO sample; the samples with POSS or TMTVS were labelled as XP or XT, respectively, where X is the weight percent of POSS or TMTVS.

To prepare the samples for pyrolysis, the crosslinked materials were first cut and polished into circular pieces roughly 10 mm in diameter and 2 mm in thickness. Next, the samples were placed into a zirconia crucible, covered on both sides with graphite mats in order to reduce friction during shrinkage and prevent warping [21, 22], and put into a tube furnace (1730-20 Horizontal Tube Furnace, CM Furnaces Inc., Bloomfield, NJ). With an Ar flow rate of about 500 std cm^3/min, the samples were heated up to 1100°C, 1300°C, or 1400°C at a rate of 1°C/min, held for 2 hrs, cooled to 400°C with a rate of 1°C/min, and finally cooled to 50°C with a rate of 2°C/min. During heating from 500°C-700°C, the Ar was bubbled through water at 60°C, giving a gas flow with a Ar:H_2O molar ratio of approximately 5:1.

Etching of the bulk SiOC samples after pyrolysis was done using a HF solution (20 wt% HF in water), which was magnetically stirred at room temperature until no significant mass loss was detected for the samples, taking approximately 4 days. The SiOC samples were then rinsed with deionized water and dried at 120°C. The mass loss due to etching was calculated by dividing the change in mass after etching by the original mass.

Ceramic yield was calculated by measuring the mass of the samples before and after the pyrolysis. The chemical bonding was evaluated using Fourier Transform Infrared Spectroscopy (FT-IR) (Nicolet 8700 with Pike GladiATR attachment, Thermo Scientific, Waltham, MA) between 500 and 4000 cm^{-1} wavenumber with a resolution of 4 cm^{-1} and averaged between 64 scans. The thermal decomposition of the polymers was investigated by thermogravimetric analysis (TGA) using a STA 449C Jupiter® analyzer (Netzsch-Gerätebau GmbH, Selb, Germany) with a temperature range of room temperature to 1000°C, a heating rate of 5 °C/min, and a N_2 flux of 40 ml/min. The densities of the bulk samples were measured using a pycnometer (AccuPyc II 1340, Micromeritics, Norcross, GA) with high purity helium gas. The phase compositions of the

pyrolyzed samples were analyzed in an X'Pert PRO diffractometer (PANalytical B.V., EA Almelo, the Netherlands) with Cu Kα radiation. The JCPDS reference cards used to identify the crystalline phases were 00-039-1425 for SiO_2, 00-029-1129 for SiC and 01-075-1621 for C. The specific surface area, pore size distribution, and pore volume of the pyrolyzed samples were evaluated using nitrogen adsorption at 77 K with a Quantachrome Autosorb-1 (Quantachrome Instruments, Boynton Beach, FL), and the samples were degassed before testing for 3 hrs at 300°C. The pore size distribution and pore volume were derived by applying the Non Local Density Functional Theory (NLDFT) to the adsorption branch of the data [23]. Assuming cylindrical pores, the average pore size was estimated using 4000V/A, where V is the pore volume and A is the specific surface area [24].

3.4 Results and Discussion

3.4.1 Polymer Architecture and Bonding

The PSO, TMTVS, and POSS species have distinct differences in their molecular structures; PSO is composed of linear polymer chains, TMTVS has a cyclic structure, and POSS has a cage-like structure, as shown in Fig. 3.1(a)-(c). Previous studies have shown that polymer precursors containing more cyclic structures favor the formation of larger SiO_2 nuclei during pyrolysis[12, 25], so determining the architecture of the Si-O-Si bonds within the precursor is significant. The differences in the architecture of organosilicon species can be determined by the position of the FT-IR Si-O-Si peak at 1000-1100 cm^{-1} (Fig. 3.1(d)). For long polymer chains, such as PSO, the Si-O-Si bond displays a broad peak between ~1000 cm^{-1} and 1100 cm^{-1}. For cyclic molecules with less than ~ 20 siloxane repeat units, such as TMTVS, the Si-O-Si peak position is well defined and centered at 1050 cm^{-1}. Likewise, for siloxanes with a cage structure, such as POSS, the peak is also well defined and centered at 1100 cm^{-1} [17, 25]. The integration of the additives into the PSO causes new peaks to appear at 1050 cm^{-1} or 1100 cm^{-1} due to the different architectures of the additives (Fig. 3.1(d)).

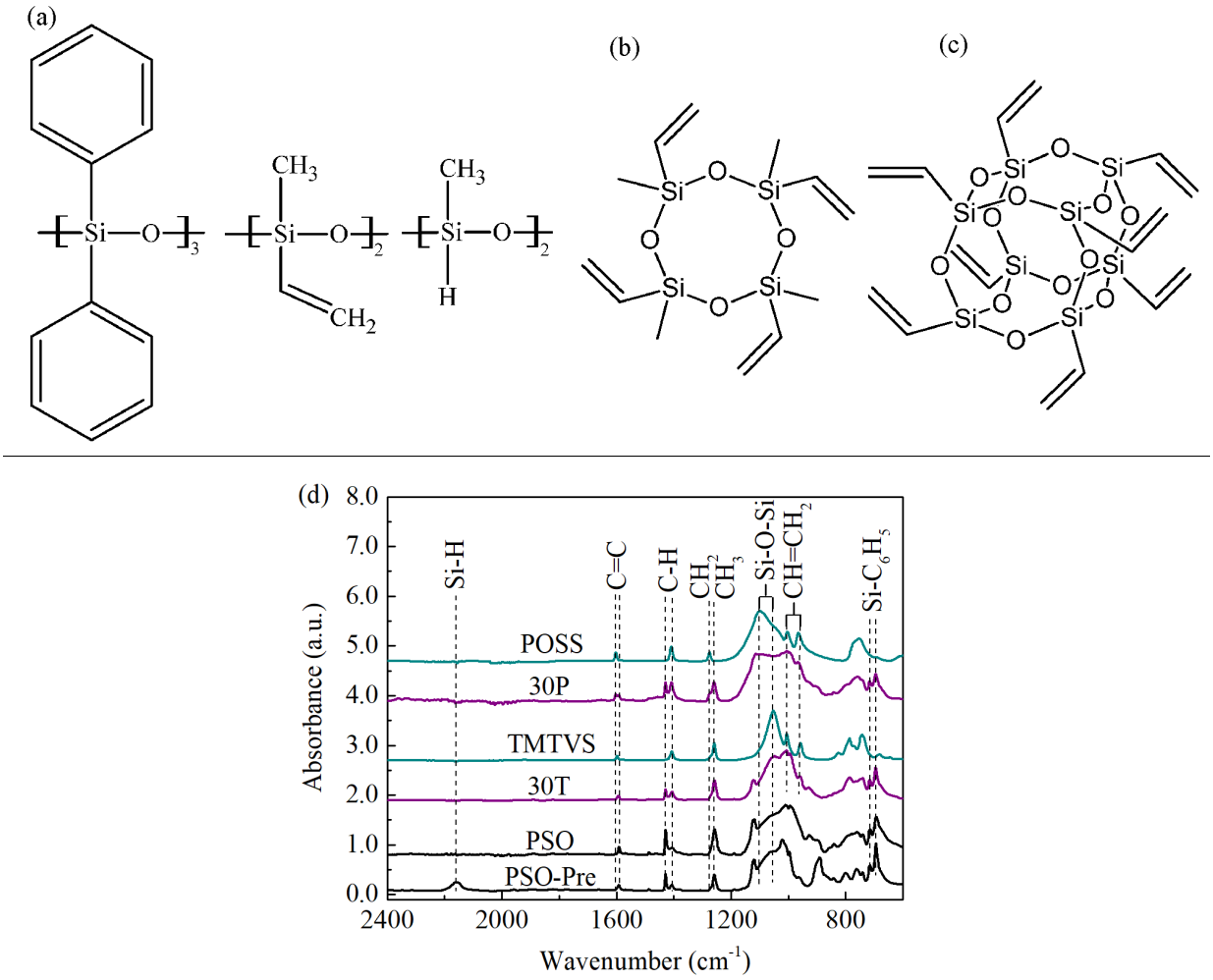

Fig. 3.1 Chemical structures of (a) PSO, (b) TMTVS, and (c) POSS, and (d) the FT-IR absorption spectra for the PSO before crosslinking (PSO-Pre) and the crosslinked PSO, 30T, and 30P polymers, as well as pure TMTVS and POSS.

Fig. 3.1(d) also shows the presence of residual vinyl bonds for the samples with TMTVS and POSS additions. For the base PSO, crosslinking occurs through hydrosilylation between the hydrogen and vinyl groups, which are present in equal molar amounts in the PSO. The consumption of the hydrogen bonds is evident in Fig. 3.1(d) comparing the spectra of the pure PSO before crosslinking (PSO-Pre) and after, which shows the disappearance of the Si-H absorption peak near 2160 cm^{-1} [26]. With the addition of either TMTVS or POSS to PSO, additional vinyl bonds are added to the polymer, leaving unreacted vinyl groups after crosslinking, as seen by the absorption peaks at 1405 cm^{-1} and 1604 cm^{-1} for the 30T and 30P samples [17]. The theoretical molar ratios of vinyl to hydrogen groups for the POSS samples are 1.6, 2.4, 3.4, and 4.7 for the

10P, 20P, 30P, and 40P samples, respectively. For the TMTVS samples, the theoretical molar ratios of vinyl to hydrogen groups is 1.6, 2.3, 3.2, and 4.4, for the 10T, 20T, 30T, and 40T samples, respectively. The residual vinyl bonds for both the TMTVS and POSS may have an effect on the bond formation during pyrolysis because the vinyl bonds can react with either other vinyl bonds or methyl bonds at elevated temperatures [27].

3.4.2 Pyrolysis Behavior

Analysis of the thermal decomposition behavior for the PSO, 30T, and 30P samples up to 1000°C was conducted using TGA as shown in Fig. 3.2. Since the TGA was conducted in inert nitrogen while the actual samples were fabricated with water vapor injection between 500°C-700°C, the focus of the TGA results will be for the initial decomposition of the precursors at temperatures below 500°C. The pure PSO sample shows two major mass loss steps at 400°C and 550°C. The mass loss at 400°C is associated with depolymerization of the siloxane chains resulting in the formation of volatile cyclic siloxane molecules, and the mass loss at 550°C is attributed to the release of various hydrocarbon compounds [28, 29]. The 30T sample, however, displays continuous degradation beginning at approximately 100°C due to the evaporation of TMTVS, which has a boiling temperature of ~110°C. The mass loss rate for the 30T sample continuously increases until reaching a maximum at 500°C. For the 30P sample, there are two well defined maxima in the mass loss rate at 400°C and 550°C, similar to the PSO, as well as a third maxima at 250°C; the peak at 250°C corresponds to the decomposition of the POSS molecules [16]. However, the mass loss after the 250°C degradation step is less than 2%; the majority of the POSS added to the polymer remains in the polymer precursor during further heating.

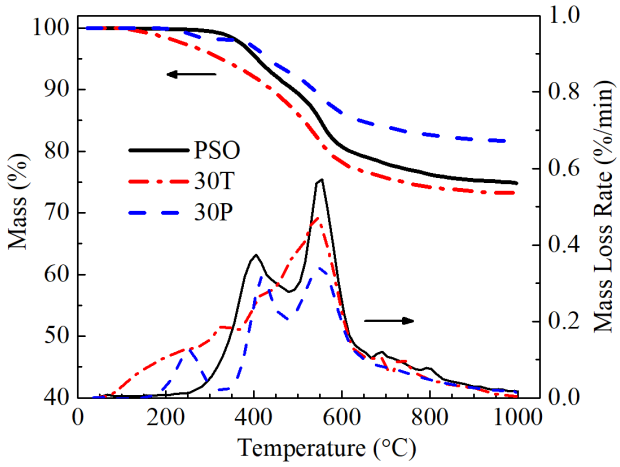

Fig. 3.2 TG and dTG for the PSO, 30T, and 30P samples in nitrogen.

The ceramic yield and linear shrinkage of the polymers after pyrolysis at 1100°C is shown in Fig. 3.3(a). The yield for the 10T and 20T samples is slightly greater than for the pure PSO sample, increasing from 72.2% for PSO to 74.1% for 20T. The increase in the ceramic yield may be due to a higher crosslinking density with the incorporation of up to 20 wt% TMTVS as well as the lower hydrocarbon content of TMTVS compared to the base PSO. With the addition of more TMTVS, however, the yield decreases to 70.9% for 30T and 66.6% for 40T, likely because the TMTVS is not fully incorporated into the PSO matrix and thus evaporates or decomposes to a greater extent during pyrolysis. For the samples with POSS, the ceramic yield continually increases as the amount of POSS increases, from 74.7% for 10P to 82.3% for 40P. The thermal stability enhancement for octavinyl-POSS has been shown in POSS-PDMS systems [16]. Similar to the TMTVS, this increase in yield may be due to an increase in the crosslinking density with more POSS. Additionally, the residual vinyl bonds in the POSS samples may react with either other vinyl groups or methyl groups during pyrolysis, creating additional linkages and further improving the thermal stability and thus yield [30]. This yield increase is significant to large scale applications.

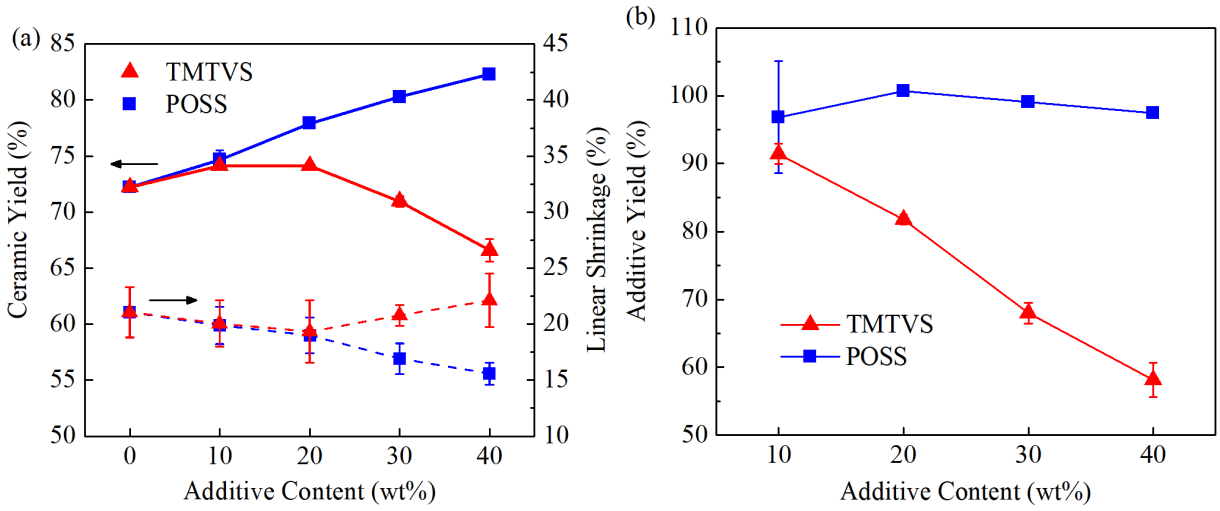

Fig. 3.3 (a) Ceramic yield and linear shrinkage of the PSO sample with the TMTVS and POSS additives after pyrolysis at 1100°C, and (b) yield of the TMTVS and POSS additives as a function of content within the PSO precursor after pyrolysis at 1100°C.

From Fig. 3.3(a), it is apparent that the additives have a significant influence on the ceramic yield of the polymer precursors. Assuming that the additive does not have a compounding effect within the polymer blends to influence the yield of the PSO, the ceramic yield of the additive, y_f, is given by:

$$y_f = \frac{Y - y_{PSO}(1 - x_f)}{x_f} \tag{3.1}$$

where Y is the measured ceramic yield of the polymer precursors in Fig. 3.3(a), y_{PSO} is the yield of the pure PSO sample, and x_f is the mass fraction of the additive in the polymer. The standard deviation for Eq. (3.1), σ_{y_f}, can be obtained using propagation of uncertainty [31]:

$$\sigma_{y_f} = \frac{\sqrt{[\sigma_Y]^2 + \left[\sigma_{y_{PSO}}(1 - x_f)\right]^2}}{x_f} \tag{3.2}$$

where σ_Y is the standard deviation of the measured ceramic yield and $\sigma_{y_{PSO}}$ is the standard deviation of the yield of the PSO sample. Applying Eqs. (3.1) and (3.2) to the measured ceramic yields for the samples pyrolyzed at 1100°C leads to Fig. 3.3(b). For TMTVS, the additive yield continuously decreases as the content within the polymer is increased, changing from 91.4% for 10T to 58.1% for 40T. The POSS additive leads to very little change between the different samples, going from 96.8% for 10P to 97.5% for 40P; the calculated yield is consistent with the TGA results

for the 30P sample, which only experienced a mass loss of about 2% near the sublimation temperature of POSS, 250°C.

The calculated additive yield for POSS is consistent with previous studies and is due to two factors: the size of the POSS molecule and the unreacted vinyl bonds. Yang et. al[16] showed that the addition of POSS with either phenyl or vinyl functional groups were physically mixed with polydimethylsiloxane and both POSS types improved the thermal stability due to lowering the mobility of the siloxane chains and the kinetics of the chain scission. The POSS with the vinyl functional group, however, had a ceramic yield twice that of the phenyl POSS due to the vinyl groups causing further reactions during pyrolysis and strengthening the polymer network.[16] This same improvement from the vinyl bonds is seen for the 10T and 20T samples, but the addition of more TMTVS causes partial evaporation of the TMTVS before temperatures high enough for the vinyl bond to react. Thus, the higher TMTVS contents lead to lower yields.

The linear shrinkage for the TMTVS-containing, as shown in Fig. 3.3(a), initially decreases from 21.1% for PSO to 19.3% for the 20T sample, but then increases with further addition of TMTVS, reaching 22.1% for the 40T sample. Overall, the linear shrinkage is not greatly affected by the amount of TMTVS within the polymer precursor, especially when considering the standard deviations of the measurements as shown in Fig. 3.3(a). The addition of the POSS causes a continual and consistent decrease in linear shrinkage, from 19.9% for the 10P sample to 15.6% for the 40P sample. Understandably, the linear shrinkage trend for the POSS samples is opposite to the ceramic yield trend.

The yields of the PSO, 30P, and 30T samples after pyrolysis at 1100°C, 1300°C, and 1400°C are shown in Fig. 3.4. The yield for the pure PSO sample decreases slightly between 1100°C and 1300°C, from 72.2% to 70.2%, likely due to the carbothermal reduction of SiO_2 to be discussed later, and is consistent with previous studies using the same PSO precursor [9, 18]. The ceramic yield for the PSO sample is then nearly the same between 1300°C and 1400°C, suggesting that there is no further carbothermal reduction. The 30T sample shows a similar trend as the PSO sample, with the major mass loss step being between 1100°C and 1300°C. For the 30P sample, the slight mass loss is delayed to higher temperatures between 1300°C and 1400°C, demonstrating the enhanced stability of the SiOC system with the POSS addition, but is of similar magnitude as those observed for the PSO and 30T samples. For the other TMTVS and POSS samples, the variation between yield and pyrolysis temperature is similar as discussed for the 30T and 30P samples.

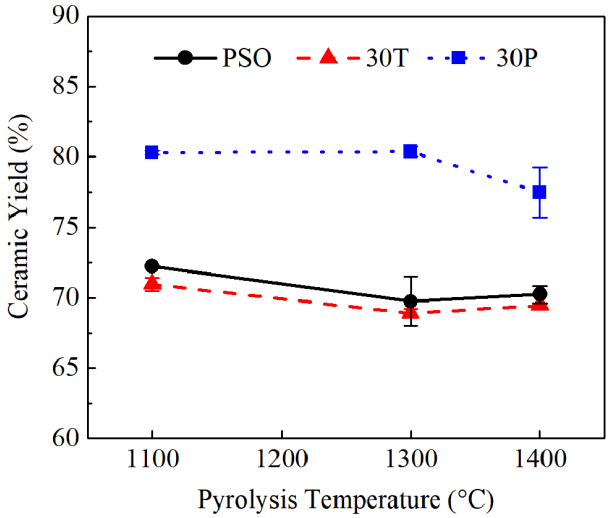

Fig. 3.4 Ceramic yield of PSO, 30T, and 30P at various pyrolysis temperatures.

The bulk density of the PSO sample after pyrolysis at 1100°C, measured using pycnometry, is 1.90 g/cm^3, lower than that of typical SiOC systems (density ~ 2.3 g/cm^3) [32-34], which is due to the significant amount of turbostratic carbon (density ~ 1.45 g/cm^3) present in the sample [22]. For the POSS samples, the densities are 1.90 g/cm^3, 1.91 g/cm^3, 1.87 g/cm^3, and 1.87 g/cm^3, for 10P, 20P, 30P, and 40P, respectively. Likewise, the densities for 10T, 20T, 30T, and 40T samples are 1.91 g/cm^3, 1.91 g/cm^3, 1.93 g/cm^3, and 1.91 g/cm^3, respectively. Thus, neither the TMTVS nor POSS additives influence the bulk density, which can be understood by considering the yield and shrinkage trends shown in Figure 3a. For both additives, the ceramic yield and linear shrinkage showed inverse trends, which resulted in similar densities for all samples after pyrolysis.

3.4.3 Phase Evolution

All of the samples after pyrolysis at 1100°C are amorphous, as shown in Fig. 3.5, with diffraction peaks only for turbostratic carbon at 43° and a broad peak centered around 23° for amorphous SiO_2. At a higher pyrolysis temperature of 1300°C, the samples still display the turbostratic carbon peaks at 43° and strong amorphous SiO_2 peaks. Additionally, small broad peaks at 35.6°, 60°, and 72° begin to appear for the PSO and 30T samples, indicating the formation of nanocrystalline β-SiC. The SiC formation is more evident for the samples with higher TMTVS additions. SiC formation is not as significant in these samples compared to similar carbon-rich

samples is due to the water vapor injection between 500°C-700°C. The water vapor encourages the formation of Si-O bonds at the expense of Si-C bonds within the samples, which results in increased SiO_2 formation and reduced SiC formation at higher pyrolysis temperatures [8, 9, 19, 20]. After pyrolysis at 1400°C, the PSO and 30T samples show more extensive SiC formation. For the 30P sample, the onset of SiC formation is delayed until 1400°C, and the SiC diffraction peaks are much smaller than for either the PSO or 30T samples. The formation of SiC within SiOC is through either the phase separation of the amorphous SiOC [5, 9, 18]:

$$2SiOC \rightarrow SiO_2(amorphous) + SiC(\beta) + C \quad (3.3)$$

or the carbothermal reduction of SiO_2:

$$SiO_2(amorphous) + 3C \rightarrow SiC(\beta) + 2CO(g) \uparrow \quad (3.4)$$

Considering that the mass loss from 1100°C to 1400°C is approximately 3 wt% for all the samples, forming only ~2.5 wt% of SiC if following Eq. (3.4), then the more dominant cause for SiC formation is through the phase separation of SiOC following Eq. (3.3). This is further supported by the increased SiC formation for PSO and 30T between 1300°C and 1400°C, even though the samples experience no major change in the ceramic yield at the same temperatures.

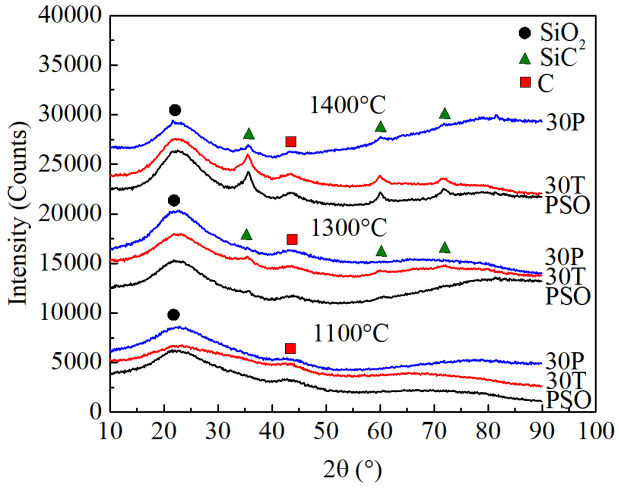

Fig. 3.5 XRD patterns for the PSO, 30T, and 30P samples pyrolyzed at 1100°C, 1300°C, and 1400°C.

To determine whether the amorphous halo in Figure 5 for the samples pyrolyzed at 1100°C is due solely to the SiOC phase or whether nucleation of SiO_2 has already begun, the samples were etched with HF. SiOC is highly resistant to leaching with HF, so only through phase separation

and formation of SiO_2 nanodomains can the material be etched to cause mass loss [35]. For the PSO sample pyrolyzed at 1100°C, the mass loss after etching is 14% as shown in Fig. 3.6. With the addition of TMTVS, the etching mass loss is slightly decreased, with most samples showing less than 10% mass loss. The incorporation of the POSS additive causes an increase in the etching mass loss for all the samples compared to the pure PSO. Thus, POSS is believed to encourage the nucleation of SiO_2 within SiOC at temperatures as low as 1100°C, attributed to its Si-containing cage molecular structure.

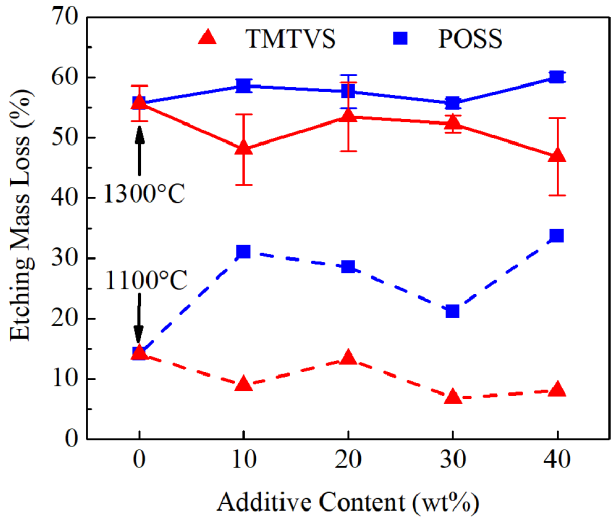

Fig. 3.6 Mass loss after HF etching of the samples pyrolyzed at 1100°C (dashed lines) and 1300°C (solid lines).

Increasing the pyrolysis temperature to 1300°C causes further etching mass loss for all the samples, due to further phase separation of SiOC as already discussed. For the TMTVS samples, the etching mass is less than that of the PSO or POSS samples and does not show any trend with the TMTVS content. This observation is consistent with the understanding that TMTVS is not conducive for SiO_2 nanocluster formation. The etching mass loss for the POSS samples is relatively constant for all samples and close to the mass loss of the PSO samples.

3.4.4 Specific Surface Area and Pore Size Distribution

Similar to Chapter 2, the samples were not powdered before testing, so all of the porosity from the HF etching is open porosity. As shown in Fig. 3.7, all the samples show a large adsorption volume at low relative pressures, followed by a relative constant adsorption volume at higher relative pressures; this adsorption behavior corresponds to the Type I isotherm, according to the IUPAC classification, which indicates that the samples are prominently microporous with only monolayer adsorption [36]. For the TMTVS samples, the adsorption volume at $P/P_o \sim 1$ steadily decreases as the TMTVS content increases, indicating a decrease in total pore volume. For the samples with POSS additions, the adsorption volumes are relatively the same to the PSO sample for the 10P, 20P, and 30P samples. With an increase of the POSS content to 40 wt%, however, the adsorption volume at relative pressures above 0.2 slightly increases compared to the other POSS samples, indicating that the mesopore volume for the 40P sample is greater than for any of the other samples with POSS.

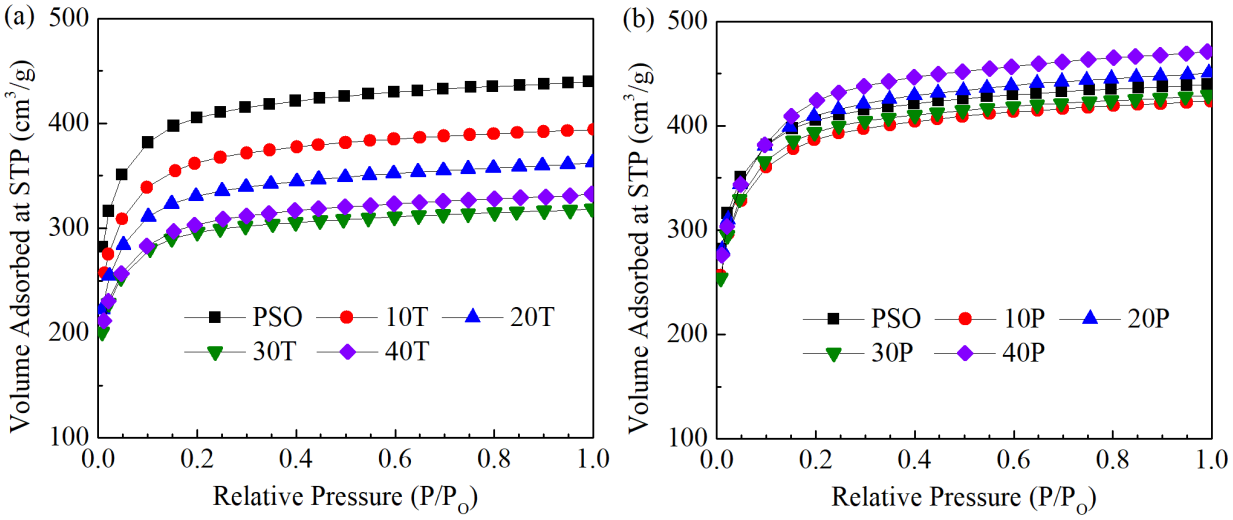

Fig. 3.7 Nitrogen adsorption isotherms for (a) TMTVS and (b) POSS samples pyrolyzed at 1300°C.

The results from nitrogen adsorption are shown in Fig. 3.8. For the TMTVS samples, the specific surface area and total pore volume also decrease with increasing TMTVS content, from 1500.9 m^2/g and 0.65 cm^3/g, respectively, for the PSO sample to 1150.7 m^2/g and 0.50 cm^3/g, respectively, for the 40T sample. The reason for the negative effects of the TMTVS additive can be understood by considering the phase formation in Fig. 3.5. At 1100°C, the samples with higher

TMTVS content produces more amorphous SiOC rather than forming SiO_2. As the temperature increases to 1300°C, the SiOC then phases separates, forming more SiC and less SiO_2 than the samples with low TMTVS additive content. Thus, after etching, the samples with higher TMTVS amounts have less SiO_2 to generate pores and thus produce lower pore volumes. For the samples with the POSS additive, both the pore volume and specific surface area are largely independent of the additive content and produce slightly higher specific surface areas and similar pore volume values compared to the PSO sample.

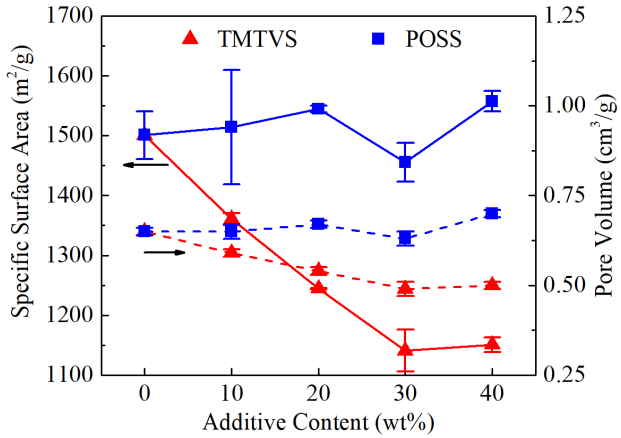

Fig. 3.8 Specific surface area (solid lines) and pore volume (dashed lines) for the samples pyrolyzed at 1300°C.

The pore size distributions for the samples pyrolyzed at 1300°C after etching are shown in Fig. 3.9. All the samples have similar pore sizes of < 2 nm and no large pores. For the pure PSO sample, the mode of the pore size distribution occurs at ~1.6 nm. The TMTVS samples show approximately the same pore size as the PSO sample, regardless of the TMTVS content, with the only significant difference in the pore concentration. Similarly, none of the POSS samples except for the 40P sample, which contains only slightly larger pores, show any significant changes to the pore size distribution compared to the PSO sample.

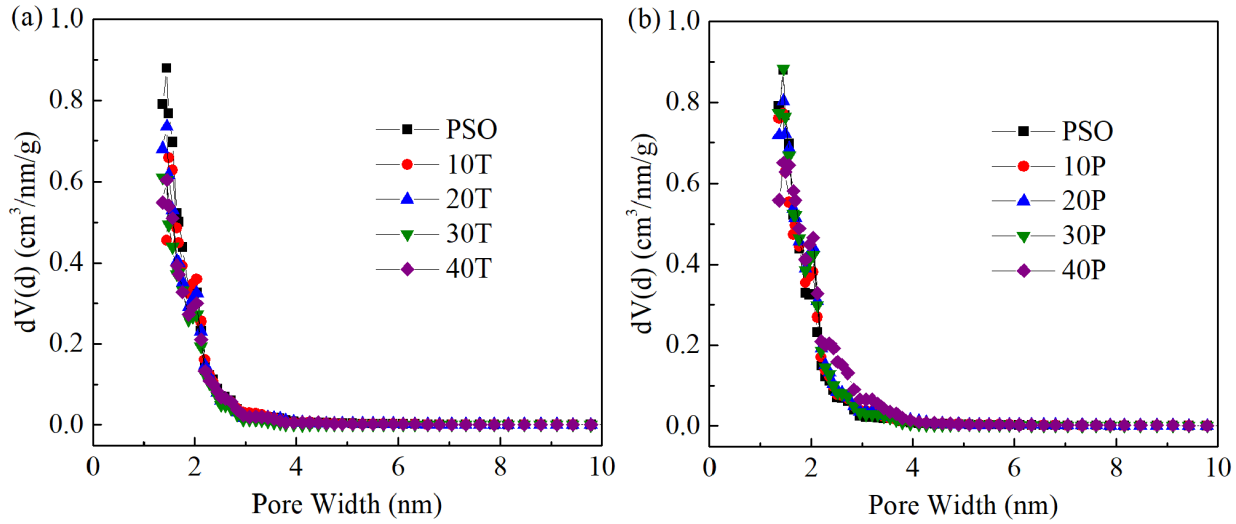

Fig. 3.9 Pore size distributions of the (a) TMTVS and (b) POSS samples pyrolyzed at 1300°C.

To understand the effect of pyrolysis temperature on the evolution of the SiO_2 nanodomains within the samples, nitrogen adsorption was conducted on the PSO, 30T, and 30P samples pyrolyzed at 1100°C and 1400°C, and the resulting pore size distributions are shown in Fig. 3.10(a) and Fig. 3.10(b), respectively. At 1100°C, the pore size distributions have only one mode at approximately 1.6 nm, similar to all of the samples pyrolyzed at 1300°C. Upon further heating to 1400°C, however, the pore size distributions begin to contain multiple modes as seen in Fig. 3.10(b). For PSO, the modes occur at ~ 1.8 nm, 3.5 nm, and 4.9 nm; similarly, the 30T sample has modes at ~1.8 nm and 4.9 nm, and the 30P sample has modes at ~1.8 nm, 3.9 nm, and 5.3 nm. Compared to the PSO, the 30T sample contains fewer pores larger than 4 nm, while the 30P sample contains a significantly larger volume of pores greater than 3 nm in diameter.

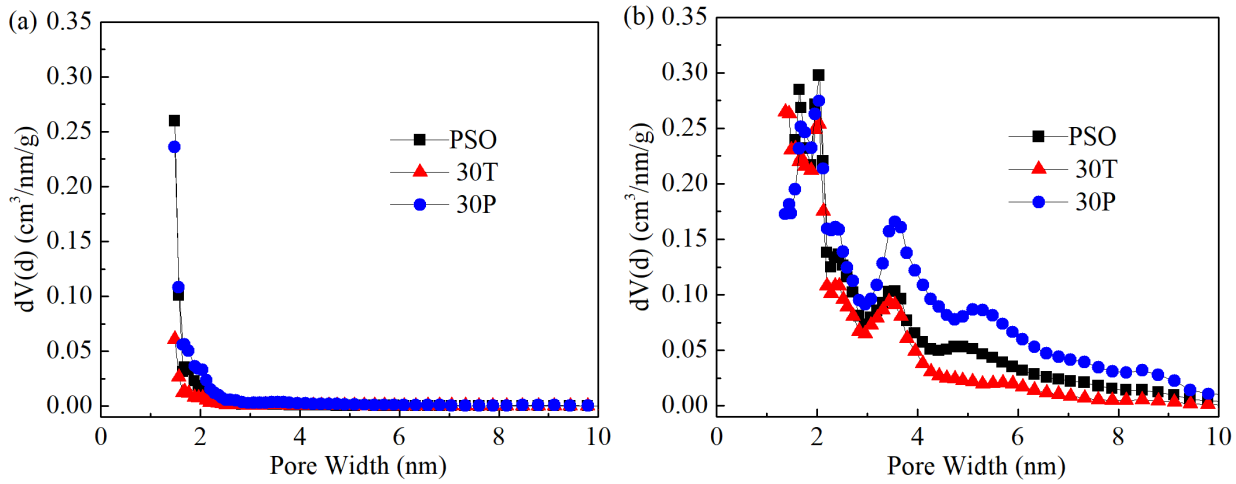

Fig. 3.10 Pore size distributions after etching for PSO, 30T, and 30P pyrolyzed at (a) 1100°C and (b) 1400°C.

3.4.5 Evolution of SiO_2 Nanodomains

At low pyrolysis temperatures between 1100°C and 1300°C, the POSS and TMTVS additives have little influence on the resulting SiO_2 size, as seen in Fig. 3.9 and Fig. 3.10(a). Thus, the nucleation of SiO_2 nanodomains from the SiOC matrix is more dominant than their growth in this temperature range. To further study the effects of the TMTVS and POSS additives on the nucleation of SiO_2, or pores after etching, within the SiOC, the pore volume and pore size for the PSO, 30T, and 30P samples at the different pyrolysis temperatures is plotted in Fig. 3.11. At 1100°C, the 30P sample has a pore volume of 0.12 cm^3/g, approximately 1.5 times the pore volume as the PSO sample (0.079 cm^3/g), while the 30T sample only has a pore volume of 0.027 cm^3/g. Thus, the POSS additive facilitates the nucleation of SiO_2 within the SiOC at lower temperatures, as also evidenced by the etching mass loss in Fig. 3.6. Increasing the pyrolysis temperature to 1300°C results in a significant increase in the pore volume for all three samples, and the PSO (0.66 cm^3/g) and 30P (0.78 cm^3/g) samples contain greater pore volumes than the 30T sample (0.47 cm^3/g). Further increasing the pyrolysis temperature to 1400°C results in almost no change in the pore volume for the PSO and 30T samples. However, the 30P sample continues to increase in pore volume upon heating from 1300°C to 1400°C.

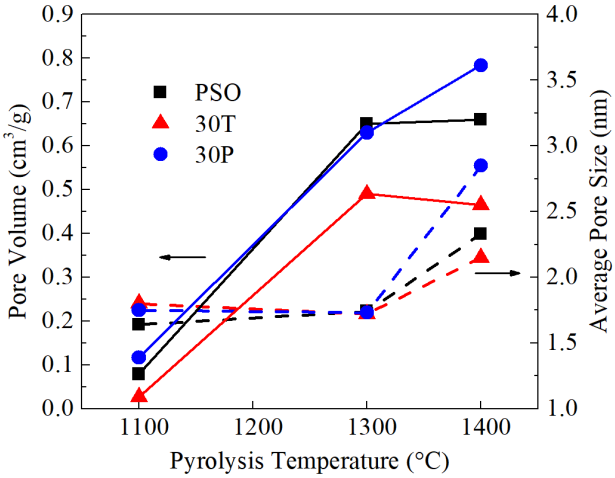

Fig. 3.11 Pore volume (solid lines) and average pore size (dashed lines) for the PSO, 30T, and 30P samples at different pyrolysis temperatures.

In addition to the pore volume, the average pore size is also shown in Fig. 3.11. At pyrolysis temperatures between 1100°C-1300°C, the average pore size for all the PSO, 30T, and 30P samples is constant at ~1.7 nm. Upon further heating to 1400°C, all samples experience significant growth of the pores. Thus, the growth of the SiO_2 domains becomes more significant at temperatures above 1300°C. At 1400°C, the PSO and 30T samples have nearly the same pore size, 2.2 nm and 2.3 nm, respectively. However, the average pore size for the 30P sample is significantly greater at 2.9 nm. A possible explanation for the increase in pore volume and more significant growth in pore size for the 30P sample after pyrolysis at 1400°C is that the more numerous SiO_2 domains in the 30P sample also have more inter-mixing with the SiOC matrix. Previous studies have found that etching SiOC ceramics with HF may unintentionally leach phases other than SiO_2. This removal is not due to the other phases reacting with HF, but rather due to the SiO_2 surrounding and encapsulating the other phases and causing their physical removal when the SiO_2 is removed.[8, 24] It is possible that the SiO_2 domains within the 30P are more dispersed within the SiOC matrix and caused co-existing, discrete SiOC, SiC, or graphitic species to be removed as well, causing a significant increase in pore volume and size.

From Fig. 3.11, it is clear that the TMTVS additive more significantly affects the nucleation of SiO_2 within the SiOC and not the growth. For the homogeneous nucleation of SiO_2 in SiOC, there is a critical nuclei size that is required to overcome the interfacial energy of the surrounding matrix [37, 38]. Given the small size of the TMTVS molecule, it is possible that the majority of the

SiO_2 nanodomains derived from the TMTVS may have not been large enough to form stable nuclei and instead remained as SiOC. This would explain the deleterious effects of the TMTVS additive on the pore volume at all pyrolysis temperatures and lower etching mass loss; if the TMTVS ultimately contributes to more SiOC formation, there would be more SiC derived from the SiOC phase separation at higher temperatures following Eq. 3.3, as evidenced in Fig. 3.5.

3.5 Conclusions

TMTVS and POSS additives are successfully incorporated into the PSO matrix. Neither the TMTVS nor POSS caused significant SiO_2 crystallization as initially thought, but both additives did have an impact on the formation of etchable SiO_2 nanodomains. During pyrolysis, TMTVS has inconsistent impact on the ceramic yield due to partial evaporation of uncrosslinked TMTVS. The POSS additive consistently increases the ceramic yield and decreases the linear shrinkage after pyrolysis, allowing for more intact samples. The POSS samples also have significantly more SiO_2 nanodomains and maintains or slightly increases the specific surface area, up to 1557 m^2/g with a larger pore size of ~1.8 nm. Thus, POSS is an excellent candidate as an additive in polymer derived porous SiOC due to its enhancement of thermal stability during the polymer-to-ceramic conversion, lowering of the SiO_2 nucleation temperature, and positive contribution to specific surface area and pore volume.

References

1. Colombo P, Mera G, Riedel R, Soraru GD. Polymer-derived ceramics: 40 years of research and innovation in advanced ceramics. *J Am Ceram Soc* **2010**, *93*, 1805-1837.
2. Lu K. Porous and high surface area silicon oxycarbide-based materials-a review. *Mater Sci Eng R Rep* **2015**, *97*, 23-49.
3. Greil P. Polymer derived engineering ceramics. *Adv Eng Mater* **2000**, *2*, 339-348.
4. Colombo P. Engineering porosity in polymer-derived ceramics. *J Eur Ceram Soc* **2008**, *28*, 1389-1395.
5. Saha A, Raj R. Crystallization maps for SiCO amorphous ceramics. *J Am Ceram Soc* **2007**, *90*, 578-583.

6. Saha A, Raj R, Williamson DL. A model for the nanodomains in polymer-derived SiCO. *J Am Ceram Soc* **2006**, *89*, 2188-2195.
7. Lu K, Erb D, Liu M. Thermal stability and electrical conductivity of carbon-enriched silicon oxycarbide. *J Mater Chem C* **2016**, *4*, 1829-1837.
8. Lu K, Li J. Fundamental understanding of water vapor effect on SiOC evolution during pyrolysis. *J Eur Ceram Soc* **2016**, *36*, 411-422.
9. Li JK, Lu K. Highly porous SiOC bulk ceramics with water vapor assisted pyrolysis. *J Am Ceram Soc* **2015**, *98*, 2357-2365.
10. Narisawa M, Funabiki F, Iwase A, Wakai F, Hosono H. Effects of atmospheric composition on the molecular structure of synthesized silicon oxycarbides. *J Am Ceram Soc* **2015**, *98*, 3373-3380.
11. Sousa BF, Yoshida IVP, Ferrari JL, Schiavon MA. Silicon oxycarbide glasses derived from polymeric networks with different molecular architecture prepared by hydrosilylation reaction. *J Mater Sci* **2013**, *48*, 1911-1919.
12. Dibandjo P, Dire S, Babonneau F, Soraru GD. Influence of the polymer architecture on the high temperature behavior of SiCO glasses: A comparison between linear- and cyclic-derived precursors. *J Non-Cryst Solids* **2010**, *356*, 132-140.
13. Dibandjo P, Dire S, Babonneau F, Soraru GD. New insights into the nanostructure of high-C SiOC glasses obtained via polymer pyrolysis. *Glass Technol: Eur J Glass Sci Technol, Part A* **2008**, *49*, 175-178.
14. Hasik M, Wojcik-Bania M, Nyczyk A, Gumula T. Polysiloxane-POSS systems as precursors to SiCO ceramics. *React Funct Polym* **2013**, *73*, 779-788.
15. Kolel-Veetil MK, Fears KP, Qadri SB, Klug CA, Keller TM. Formation of a crosslinked POSS network by an unusual hydrosilylation: Thermo-oxidative stabilization of the α-cristobalite phase in its amorphous regions. *J Polym Sci, Part A: Polym Chem* **2012**, *50*, 3158-3170.
16. Yang D, Zhang W, Yao RL, Jiang BZ. Thermal stability enhancement mechanism of poly(dimethylsiloxane) composite by incorporating octavinyl polyhedral oligomeric silsesquioxanes. *Polym Degrad Stab* **2013**, *98*, 109-114.

17. Wang X, Hu YA, Song L, Xing WY, Lu HD. Thermal degradation behaviors of epoxy resin/POSS hybrids and phosphorus-silicon synergism of flame retardancy. *J Polym Sci, Part B: Polym Phys* **2010**, *48*, 693-705.
18. Li JK, Lu K, Lin TS, Shen FY. Preparation of micro-/mesoporous SiOC bulk ceramics. *J Am Ceram Soc* **2015**, *98*, 1753-1761.
19. Erb D, Lu K. Additive and pyrolysis atmosphere effects on polysiloxane-derived porous SiOC ceramics. *J Eur Ceram Soc* **2017**, *37*, 4547-4557.
20. Liang T, Li Y-L, Su D, Du H-B. Silicon oxycarbide ceramics with reduced carbon by pyrolysis of polysiloxanes in water vapor. *J Eur Ceram Soc* **2010**, *30*, 2677-2682.
21. Janakiraman N, Aldinger F. Fabrication and characterization of fully dense Si-C-N ceramics from a poly (ureamethylvinyl) silazane precursor. *J Eur Ceram Soc* **2009**, *29*, 163-173.
22. Martinez-Crespiera S, Ionescu E, Kleebe HJ, Riedel R. Pressureless synthesis of fully dense and crack-free SiOC bulk ceramics via photo-crosslinking and pyrolysis of a polysiloxane. *J Eur Ceram Soc* **2011**, *31*, 913-919.
23. Ravikovitch PI, Neimark AV. Characterization of nanoporous materials from adsorption and desorption isotherms. *Colloids Surf, A* **2001**, *187*, 11-21.
24. Peña-Alonso R, Sorarù GD, Raj R. Preparation of ultrathin-walled carbon-based nanoporous structures by etching pseudo-amorphous silicon oxycarbide ceramics. *J Am Ceram Soc* **2006**, *89*, 2473-2480.
25. Anderson DR. Infrared, Raman, and ultraviolet spectroscopy. In: Smith AL, editor. Analysis of silicones. Malabar, FL: Robert E. Krieger Publishing Company, Inc., 1983; p. 257-279.
26. Liu GW, Kaspar J, Reinold LM, Graczyk-Zajac M, Riedel R. Electrochemical performance of DVB-modified SiOC and SiCN polymer-derived negative electrodes for lithium-ion batteries. *Electrochim Acta* **2013**, *106*, 101-108.
27. Nyczyk-Malinowska A, Wojcik-Bania M, Gumula T, Hasik M, Cypryk M, Olejniczak Z. New precursors to SiCO ceramics derived from linear poly(vinylsiloxanes) of regular chain composition. *J Eur Ceram Soc* **2014**, *34*, 889-902.
28. Hourlier D, Venkatachalam S, Ammar MR, Blum Y. Pyrolytic conversion of organopolysiloxanes. *J Anal Appl Pyrolysis* **2017**, *123*, 296-306.

29. Camino G, Lomakin SM, Lageard M. Thermal polydimethylsiloxane degradation. Part 2. The degradation mechanisms. *Polymer* **2002**, *43*, 2011-2015.
30. Gibbons GJ, Holland D, Howes AP. Structure development in simple cross-linked organopolysiloxanes. *J Sol-Gel Sci Technol* **1998**, *13*, 379-383.
31. Ku HH. Notes on use of propagation of error formulas. *J Res Natl Bur Stand Sec C* **1966**, *70C*, 263-273.
32. Brequel H, Enzo S, Walter S, Sorarù GD, Badheka R, Babonneau F. Structure/property relationship in silicon oxycarbide glasses and ceramics obtained via the sol-gel method. *J Metastable Nanocryst Mater* **2002**, *13*, 359-364.
33. Walter S, Soraru GD, Brequel H, Enzo S. Microstructural and mechanical characterization of sol gel-derived Si-O-C glasses. *J Eur Ceram Soc* **2002**, *22*, 2389-2400.
34. Soraru GD, Dallapiccola E, Dandrea G. Mechanical characterization of sol-gel-derived silicon oxycarbide glasses. *J Am Ceram Soc* **1996**, *79*, 2074-2080.
35. Soraru GD, Modena S, Guadagnino E, Colombo P, Egan J, Pantano C. Chemical durability of silicon oxycarbide glasses. *J Am Ceram Soc* **2002**, *85*, 1529-1536.
36. Sing KSW. Reporting physisorption data for gas solid systems - with special reference to the determination of surface-area and porosity. *Pure Appl Chem* **1982**, *54*, 2201-2218.
37. Yu L, Raj R. On the thermodynamically stable amorphous phase of polymer-derived silicon oxycarbide. *Sci Rep* **2015**, *5*, 14550.
38. Varga T, Navrotsky A, Moats JL, Morcos RM, Poli F, Müller K, Saha A, Raj R. Thermodynamically stable $Si_xO_yC_z$ polymer-like amorphous ceramics. *J Am Ceram Soc* **2007**, *90*, 3213-3219.

4 Influence of Vinyl Bonds from PDMS on the Pore Structure of Polymer Derived Ceramics

4.1 Abstract

The influence of vinyl bonds on the phase separation and decomposition of polydimethylsiloxane (PDMS) was investigated for a saturated PDMS (s-PDMS) and an unsaturated poly(dimethylsiloxane-co-vinylmethylsiloxane) (v-PDMS) with the same molecular weight, and the resulting pore sizes were investigated for two base polymer systems, one with an excess of hydrogen bonds (PHMS, polyhydromethylsiloxane) and one with stoichiometric hydrogen to vinyl bonds (PSO, polysiloxane). For PHMS, the samples with s-PDMS have lower ceramic yield and higher total porosity, while the samples with v-PDMS contain nearly no porosity after pyrolysis to 1300°C due to extensive hydrosilylation between the hydrogen and vinyl groups. For the PSO, both s-PDMS and v-PDMS produce micron-sized pores, but the v-PDMS produces smaller pores with a narrower size distribution than the s-PDMS. The fundamental differences in the polymer phase separation and decomposition arising from the addition of vinyl bonds to the PDMS chains and the effect of the base polymer hydrogen content are discussed.

4.2 Introduction

Porous ceramic components containing macro-, meso-, and/or micro-pores are important for applications such as catalyst supports, thermal insulation, and gas separation membranes [1]. The use of polymer derived ceramics offers distinct advantages over traditional powder based processing techniques due to lower processing temperatures and a wide range of available compositions [2, 3]. In particular, porous silicon oxycarbide (SiOC) is an excellent candidate due to its resistance to chemical and oxidation degradation, high temperature stability, and excellent mechanical properties [1, 2, 4-6].

There are several routes to fabricate porous polymer derived ceramics, including sacrificial fillers [7-9], foaming [10-14], freeze casting [15, 16], selective etching of a ceramic phase [17-22], and polymer phase decomposition [23-25]. The pore size, shape, and distribution within polymer derived ceramics

can be tailored to fit a specific application: pores created by selective etching or polymer decomposition are often spherical and uniformly distributed and are well suited for thermal insulation or adsorption of gas, ions, and dyes [22-25]; pores created using foaming or freeze casting can be directionally aligned and useful in applications requiring high permeability such as catalysis and filtration [10, 15, 16]. One particular processing strategy, polymer phase separation followed by selective decomposition of one of the polymers, such as polydimethylsiloxane (PDMS), during pyrolysis has gained attention in recent years as a convenient processing route to create porous SiOC and SiC ceramics with different pore sizes [3, 23-25]. The pore sizes resulting from the decomposition of the PDMS phase can range from meso- to macro-scale depending on the processing conditions. The effects of various processing variables on the pore size and porosity have been researched, including the viscosity of the PDMS [26], the content of PDMS in the polymer blend [23-26], the base polymer system [3, 23], and the pyrolysis temperature [24]. However, the studies thus far have been largely empirical, with the given results being specific to the polymer system used.

Recently, Blum et al. [24] reported the fabrication of mesoporous SiOC through the hydrosilylation reaction of vinyl terminated PDMS and a hydrogen containing base polymer. By simply changing the molecular weight of the PDMS additive from 9400 g/mol to 155000 g/mol, the resulting pore size from the PDMS decomposition can vary between 5 nm to 32 nm [24]. This processing technique has achieved pore sizes corresponding to the molecular size of the PDMS molecule within the SiOC ceramics. However, there are fundamental differences between the vinyl terminated PDMS used by Blum et al. [24] and a fully saturated PDMS polymer typically used to fabricate porous SiOC [3, 25, 26]. Thus, additional research into the use of vinyl-containing PDMS is needed in order to understand the effects of the vinyl bonds during the decomposition of the PDMS molecules.

In this study, two PDMS molecules are compared with the only difference being the presence of vinyl bonds along the backbone of one of the PDMS polymers (s-PDMS vs. v-PDMS). Further, two different base polymers are used, one with an excess of hydrogen bonds (PHMS) and the other with an equimolar amount of hydrogen and vinyl bonds (PSO), to illustrate the effect of the vinyl bonds during pyrolysis when either bonded during crosslinking through hydrosilylation or when left unsaturated.

4.3 Experimental Procedures

Polyhydromethylsiloxane (PHMS, M_W ~ 1600 g/mol, $(CH_3)_3SiO[-Si(H)CH_3O-]_nSi(CH_3)_3$, Gelest Inc., Morrisville, PA) was chosen as the precursor for one of the base polymer systems used, and divinylbenzene (DVB, M_W = 130.2 g/mol, Sigma-Aldrich, St. Louis, MO) was used as the crosslinking agent. The other base polymer system used was a commercial polysiloxane (PSO, $[-Si(C_6H_5)_2O-]_3[-Si(CH_3)(H)O-]_2[-Si(CH_3)(CH=CH_2)O-]_2$, SPR-684, viscosity: 10 Pa s, Starfire Systems, Inc., Schenectady, NY). For both polymers, 2.1-2.4% platinum-divinyltetramethyldisiloxane complex in xylene (Pt catalyst, Gelest Inc., Morrisville, PA) was used as the catalyst. A fully saturated PDMS (M_W = 28000 g/mol, $(CH_3)_3SiO[-Si(CH_3)_2O-]_nSi(CH_3)_3$, viscosity: 1 Pa s, Fisher Scientific, Pittsburgh, PA) and a PDMS copolymer containing 7-8% vinylmethylsiloxane (VDT-781, M_W = 28000 g/mol, $(CH_3)_3SiO[-Si(CH_3)_2O-]_n[Si(CH_3)(CH=CH_2)O-]_m(Si(CH_3)_3$, viscosity: 0.8-1.2 Pa s, Gelest Inc., Morrisville, PA) were selected as the additives and pore forming species.

First, a mixture of PHMS and DVB with a 1:0.6 weight ratio was prepared, which was simply labelled as PHMS in this study for brevity; the PHMS mixture had a viscosity of 0.01 Pa·s. Then PHMS-PDMS or PSO-PDMS mixtures containing 0, 10, 20, or 30 wt% of both types of PDMS were mixed. Toluene (Fisher Scientific, Pittsburgh, PA) was added to the PSO solutions as needed to provide a suitable viscosity for mixing. The solution was mixed for 15 minutes using a high energy mill (SPEX 8000M Mixer/Mill, SPEX SamplePrep, Metuchen, NJ). Next, the Pt catalyst (5 ppm relative to PHMS, 225 ppm relative to PSO) was added, the mixture was milled again for 5 minutes and then poured into aluminum foil molds. The mixture was placed into a vacuum chamber and vacuumed to approximately 20 Torr for 30 minutes to remove any solvent or trapped bubbles. After that, the mixture was crosslinked in an oven at 50°C for 12 hrs, 80°C for 10 hrs, and then at 120°C for 6 hrs. Samples are denoted as either PHMS-Xs or PSO-Xs for the samples containing saturated PDMS and PHMS-Xv or PSO-Xv for samples with the vinyl containing PDMS; X is the weight percent of PDMS in the polymer blend.

To prepare the samples for pyrolysis, the crosslinked polymers were first cut and polished into pieces roughly 10 mm in length and 2 mm in thickness. Next, the samples were placed into a zirconia crucible, covered on both sides with graphite mats in order to reduce friction during shrinkage and prevent warping [27, 28], and put into a tube furnace (1730-20 Horizontal Tube

Furnace, CM Furnaces Inc., Bloomfield, NJ). The samples were heated up to 1300°C at a rate of 1 K/min, held for 2 hrs, cooled to 400°C with a rate of 1 K/min, and finally cooled to 50°C with a rate of 2 K/min, all with an Ar flow (500 std cm^3/min). When the furnace was between 500-700°C during heating, the Ar was bubbled through water at 60°C, giving a gas flow with a Ar:H_2O molar ratio of approximately 5:1. The 500°C-700°C water vapor injection was used to facilitate SiO_2 formation, and the temperature range was chosen because it corresponded to the temperature range at which most mass loss occurs for the base polymers.

Etching of the bulk SiOC samples after pyrolysis was done using a solution of HF (20 wt% HF in water). The HF solution was magnetically stirred at room temperature until the SiOC samples had no significant mass loss, taking approximately 3 days. The SiOC samples were then rinsed with deionized water and dried at 120°C. The mass loss due to etching was calculated by dividing the change in mass after etching by the original mass.

The chemical bonding was evaluated using Fourier Transform Infrared Spectroscopy (FT-IR) (Nicolet 8700 with Pike GladiATR attachment, Thermo Scientific, Waltham, MA), which recorded between 500 and 4000 cm^{-1} wavenumber with a resolution of 4 cm^{-1} and averaged between 64 scans. The thermal decomposition of the polymers was investigated by thermogravimetric analysis (TGA) using a STA 449C Jupiter® analyzer (Netzsch-Gerätebau GmbH, Selb, Germany) with a temperature range of room temperature to 1000°C, a heating rate of 5 °C/min, and a N_2 flux of 40 ml/min. Linear shrinkage and ceramic yield were calculated by measuring the dimensions and mass, respectively, of the samples before and after the pyrolysis; bulk density and apparent density were calculated using the Archimedes method with water as the medium. An environmental SEM (Quanta 600 FEG, FEI, Hillsboro, OR) was used to observe the microstructures of the pyrolyzed samples. Pore size distributions were obtained from high contrast SEM images, with three images per sample, using the image analysis software ImageJ [29]. The specific surface area and pore volume of micro-/meso-pores within the samples after the HF etching was measured using nitrogen adsorption at 77 K (NOVA 2200e, Quantachrome Instruments, Boynton Beach, FL). The viscosity of the polymers was measured at room temperature with a rheometer (AR 2000, TA Instruments, New Castle DE) and a cone-plate geometry.

4.4 Results and Discussion

4.4.1 Polymer Chemical Structure

The PHMS-PDMS solutions after mixing but before crosslinking were transparent for both the v-PDMS and s-PDMS samples. After crosslinking, however, the s-PDMS samples became opaque while the v-PDMS samples remained transparent, as shown in Fig. 4.2(a). The opaque appearance of the s-PDMS samples is due to phase separation of the PDMS molecules from the PHMS because the two polymers have little to no crosslinks (Fig. 4.2(c)), and significant scattering of light occurs as the phase boundary grows to several hundred nanometers or greater, the same scale as the wavelength of visible light. The opaque nature of the PHMS-PDMS crosslinked system has also been observed in other studies using PDMS [25]. For the v-PDMS samples, however, the samples remain transparent, similar to the pure PHMS sample, up to 30 wt% v-PDMS. The hydrosilylation (Fig. 4.1) reaction between the hydrogen bonds in the PHMS and the vinyl bonds in the v-PDMS [24, 30, 31] may have prevented such large scale phase separation, leaving the sample transparent, as shown in Fig. 4.2(c). On the contrary, the PSO-PDMS solutions become opaque during mixing due to the incompatibility between PDMS and phenyl groups [32, 33], and the polymer blends remain opaque after crosslinking for both the s-PDMS and v-PDMS polymers as shown in Fig. 4.2(b).

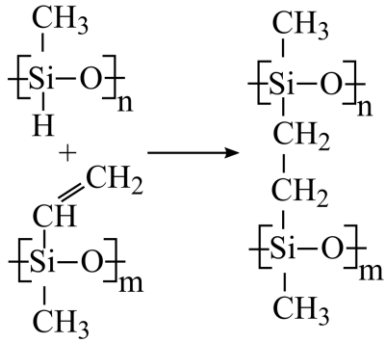

Fig. 4.1 Hydrosilylation reaction between hydrogen and vinyl bonds to induce crosslinks.

In addition to becoming opaque after crosslinking, the PHMS/s-PDMS samples also show different microstructures depending on the PDMS content. The PHMS-10s and PHMS-20s

samples are composed of the PHMS matrix with the s-PDMS phase dispersed throughout with a close-to-spherical shape; the size of the s-PDMS phase increases as the weight percent of PDMS is increased from 10 wt% to 20 wt%. For the PHMS-30s sample, phase inversion has occurred, with the s-PDMS phase now comprising the matrix and the PHMS in a droplet form (Fig. 4.2(c)). This phase inversion behavior for blends of PHMS and s-PDMS was also observed by Yan et al. [25], which used tetramethyltetravinylcyclotetrasiloxane as the crosslinking agent as opposed to DVB in this study. Due to the initial compatibility between the PHMS and PDMS molecules, the change in microstructure can be attributed to the crosslinking of the PHMS and DVB, which effectively increases the molecular weight of the PHMS until the PHMS and PDMS can no longer form a single phase and thus phase separate. This behavior is typical for systems that experience polymerization induced phase separation [34, 35].

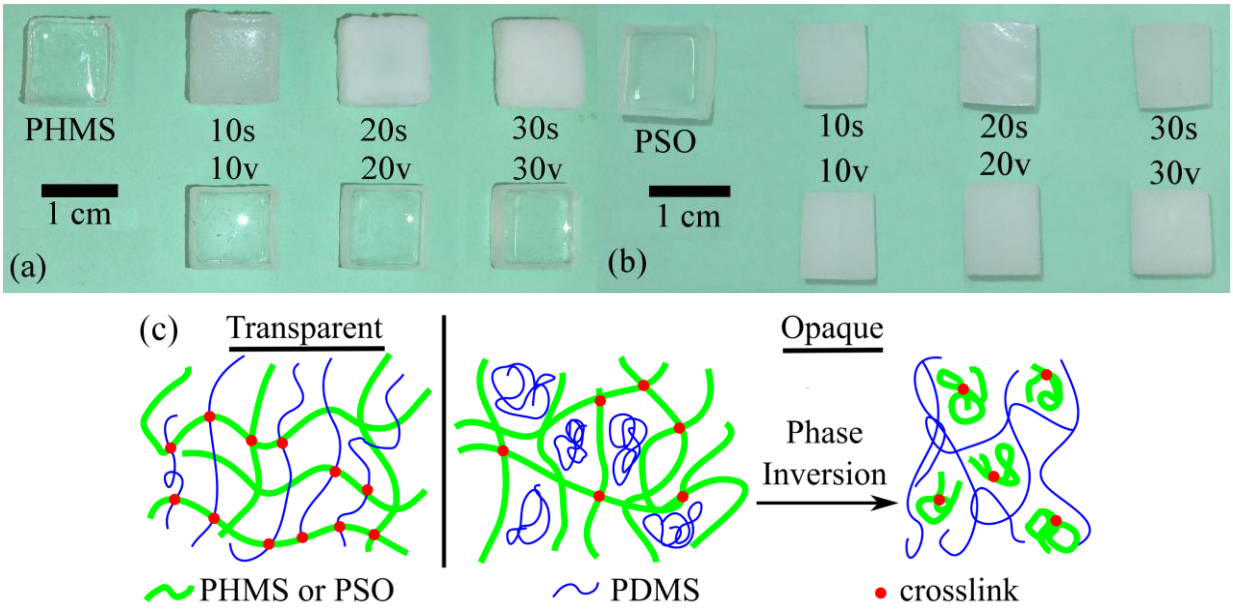

Fig. 4.2 Crosslinked samples for (a) PHMS base polymer and (b) PSO base polymer; (c) crosslinking difference between transparent and opaque samples.

The FT-IR spectra for the crosslinked PHMS-PDMS polymers as well as the pure s-PDMS and v-PDMS polymers are shown in Fig. 4.3; each of the spectra is normalized to the Si-O-Si peak at ~1000 cm^{-1} in order to show differences between the samples. In the pure PHMS sample, the major absorption peaks are attributed to Si-O-Si (1000-1100 cm^{-1}), Si-CH_3 (1256 cm^{-1}), Si-H (2157

cm^{-1}), and CH_x (2868-2960 cm^{-1}). With the addition of s-PDMS, no new peaks are formed because the s-PDMS has no new chemical bonds compared to the PHMS. Between 20 wt% and 30 wt% s-PDMS, the absorbance peak due to Si-H disappears, which is attributed to the phase inversion behavior of the 30 wt% s-PDMS sample as already discussed. Since the PDMS phase surrounds the PHMS phase, the signal from the attenuated total reflectance (ATR) cannot penetrate through the PDMS phase, and the signal from the PHMS is not observable. Similar to the s-PDMS samples, the addition of v-PDMS causes no new peaks to form. However, the samples do not show the disappearance of the Si-H peak due to the more homogenous distribution of the polymers.

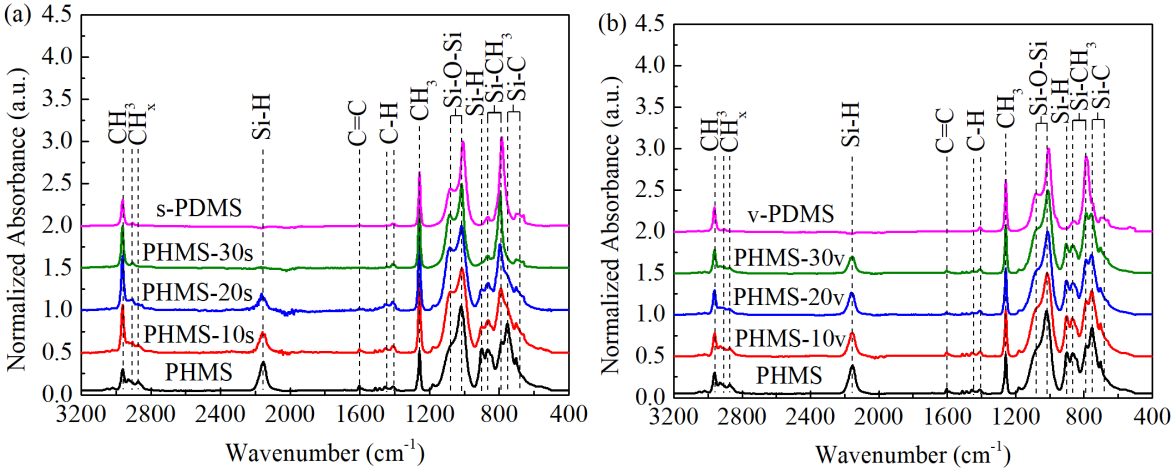

Fig. 4.3 FT-IR spectra for pure PHMS, 10-30 wt% PDMS, and pure PDMS: (a) s-PDMS, and (b) v-PDMS.

The FT-IR plots for the PSO-PDMS blends (Fig. 4.4) show no major differences in the spectra of the polymers after crosslinking. The spectra for both the s-PDMS in Fig. 4.4(a) and v-PDMS in Fig. 4.4(b) show similar peaks, which is to be expected since the vinyl content in the v-PDMS polymer is only 7-8 mol%. The PSO polymer has equal molar amounts of hydrogen and vinyl bonds, so the concentration of hydrogen bonds after crosslinking is minimal. Thus, the PSO polymer does not have an excess of Si-H bonds like the PHMS polymer. Due to this deficiency in Si-H bonds compared to vinyl bonds with the addition of v-PDMS, the probability of v-PDMS molecules attaching to the PSO through hydrosilylation is much less likely than for the PHMS base. The consumption of the hydrogen bonds in the PSO does not necessarily mean that the hydrogen bonds have all reacted with the vinyl bonds in the PSO rather than the v-PDMS polymer.

However, given that the PSO and PDMS molecules readily phase separate due to the phenyl group in the PSO [33], the interaction between the PSO and PDMS molecules is likely much lower than the PSO molecules within the PSO phase.

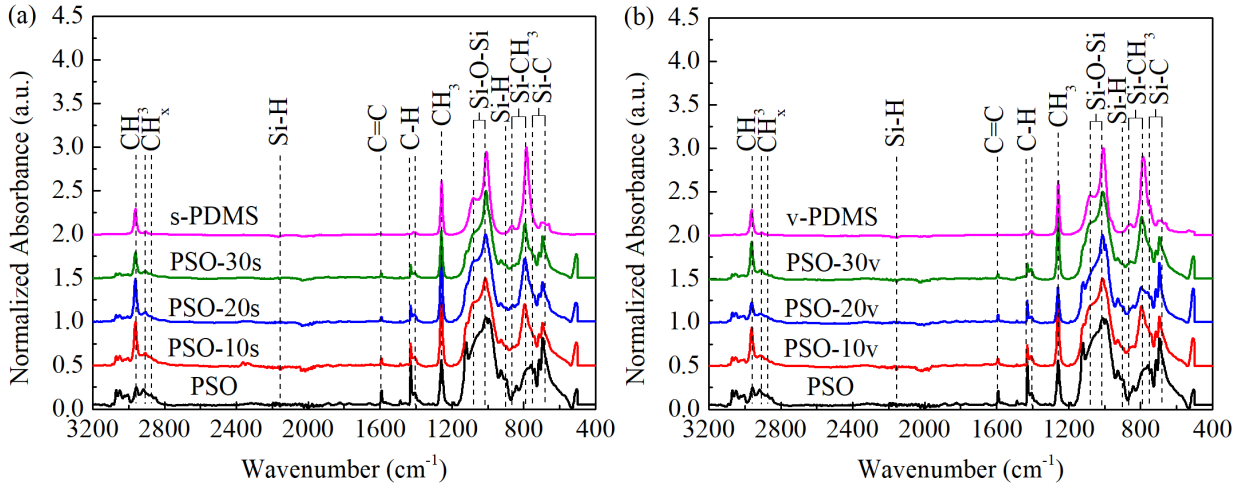

Fig. 4.4 FT-IR spectra for pure PSO, 10-30 wt% PDMS, and pure PDMS: (a) s-PDMS, and (b) v-PDMS.

4.4.2 Pyrolysis Behavior

The decomposition behaviors of the base polymers, and the base polymers with 20 wt% addition of s-PDMS and v-PDMS are investigated using TGA, and the resulting TG and dTG curves are shown in Fig. 4.5. For the PHMS base polymers, the onset of decomposition for the PHMS-20s sample is at ~350°C, while the PHMS and PHMS-20v samples begin decomposition at a slightly higher temperature of 400°C. Initial degradation of trimethylsilylated PDMS is caused by the depolymerization of linear chains with the formation of cyclic siloxane products [36]. This depolymerization can be inhibited through increasing the crosslink density of the polymer, enhancing its thermal stability [36, 37]. Thus, the higher onset degradation temperature for the PHMS and PHMS-20v samples can be attributed to a higher crosslinking density compared to that of the PHMS-20s sample. Both the PHMS and PHMS-20v samples have a maximum mass loss rate around 575°C on the dTG curve and a second smaller maximum at 700°C. After the completion of pyrolysis at 1000°C, the PHMS and PHMS-20v samples have ceramic yields close to 80%, while the ceramic yield of the PHMS-20s sample is much lower at 64%. These differences in the

decomposition behavior between the s-PDMS and v-PDMS samples can be attributed to the vinyl groups in the v-PDMS which promote the formation of Si-CH_2-Si or Si-CH_2-CH_2-Si bonds during pyrolysis and delay the decomposition of the PDMS molecules until much higher temperatures.

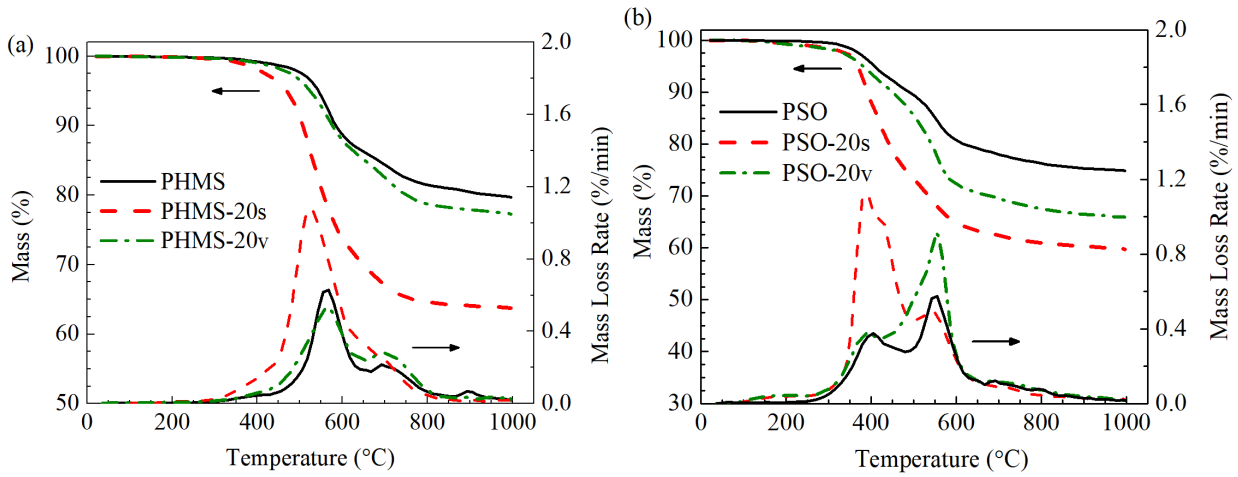

Fig. 4.5 TG and dTG of the (a) PHMS, PHMS-20s, PHMS-20v, and (b) PSO, PSO-20s, PSO-20v samples.

The decomposition behaviors of the PSO, PSO-20s, and PSO-20v samples are shown in Fig. 4.5(b). All three of the samples show two maxima on the dTG curves: one maximum at around 400°C and the other around 550°C. The PSO-20s sample shows a higher decomposition rate at 400°C and has about the same decomposition rate as the PSO at 550°C. Most likely, the mass loss centered at 400°C is due to the decomposition of the PDMS molecules. The PSO-20v polymer has a similar decomposition rate as PSO at 400°C, but then a much higher mass loss rate at 550°C. The difference between the two types of PDMS molecules can again be attributed to the vinyl bonds in the v-PDMS sample. Even without forming Si-CH_2-CH_2-Si bonds through hydrosilylation, the vinyl groups can form additional bonds during pyrolysis, leading to strengthening of the polymer network [38]. Due to these additional bonds, the PSO-20v polymer has a slightly higher yield and a slower decomposition rate compared to the PSO-20s polymer; however, both polymers show much lower yields than the base PSO.

The ceramic yield and the linear shrinkage of the samples after pyrolysis at 1300°C are given in Fig. 4.6. Compared to PHMS, the s-PDMS samples all have lower ceramic yields, as expected due to the decomposition of the PDMS molecules. With further addition of s-PDMS, the

ceramic yield continues to decrease. For the v-PDMS samples, the ceramic yield for the 10 wt% v-PDMS sample is similar to that of the 10 wt% s-PDMS sample. However, for higher v-PDMS contents, the yield decreases only slightly, due to the vinyl bonds in the v-PDMS creating additional crosslinks and preventing the decomposition of all the PDMS molecules.

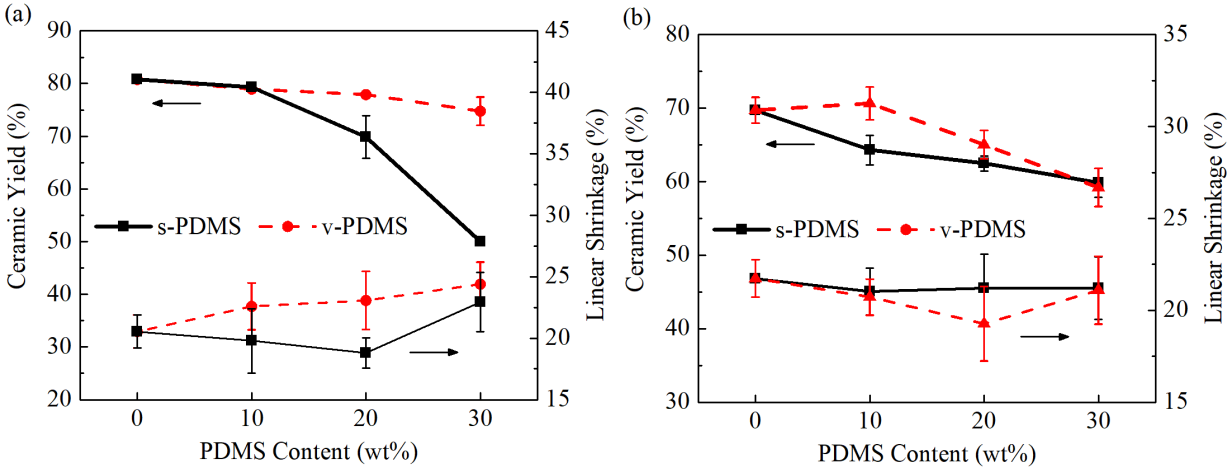

Fig. 4.6 Ceramic yield and linear shrinkage of the (a) PHMS and (b) PSO samples after pyrolysis at 1300°C.

For the PSO base, the addition of s-PDMS decreases the ceramic yield for all the PDMS contents tested, confirming the decomposition of the PDMS molecules. With only 10 wt% v-PDMS, the ceramic yield of the PSO-PDMS polymer is increased. As the v-PDMS content is increased, however, the ceramic yield quickly decreases to a similar value to that of the s-PDMS samples. The change in the ceramic yield with the v-PDMS content can be attributed to the interaction between the PSO and v-PDMS polymers. With higher v-PDMS concentrations in the polymer mixture, the interactions between the PSO and v-PDMS molecules decrease, reducing the probability of interaction between the vinyl bonds in the v-PDMS and the hydrogen bonds in the PSO so that the phase separation of the two polymers occurs more readily. This would cause the v-PDMS sample to respond more similarly to the s-PDMS, which has no interaction with the PSO polymer, as clearly shown by the ceramic yield values in Fig. 4.6(b).

The linear shrinkage of the 10 wt% and 20 wt% s-PDMS samples decreases only slightly compared to that of the PHMS sample; with the addition of 30 wt% s-PDMS, the shrinkage increases much more, most likely due to the different microstructure of the 30 s-PDMS sample

(Fig. 4.6(a)). For the v-PDMS samples, the linear shrinkage continually increases with the PDMS concentration. This behavior can be attributed to the sintering of the pores created from the v-PDMS, due to their much smaller size as to be discussed. The PSO samples show much less difference between the s-PDMS and v-PDMS samples, since there is little to no hydrosilylation occurring between the PSO and v-PDMS polymers (Fig. 4.6(b)). Further, the linear shrinkage also shows no dependence on the content of PDMS within the polymer, with all PSO/PDMS samples showing linear shrinkage values close to that of the pure PSO sample.

4.4.3 Porosity and Pore Size

The bulk and apparent densities for the PHMS/PDMS and PSO/PDMS samples are shown in Table 4.1. The bulk density takes into account the volume of the SiOC matrix and the open and closed pores; the apparent density considers the volume of the SiOC matrix and closed pores only. For the PHMS base, the samples with s-PDMS show a continual decrease in the bulk density while maintaining similar apparent densities. This result indicates that the open porosity of the PHMS/s-PDMS samples increases with increasing s-PDMS content while the closed porosity stays relatively constant. For the PHMS samples with v-PDMS, the bulk density shows no such dependence on the v-PDMS concentration, and all v-PDMS samples have similar bulk and apparent densities to the pure PHMS sample. This means that v-PDMS has no significant effect on the open porosity of the PHMS samples.

Table 4.1 Bulk and apparent densities of the PHMS and PSO samples after pyrolysis.

Base Polymer	PDMS Content (wt%)	Bulk Density, ρ_b (g/cm^3)		Apparent Density, ρ_a (g/cm^3)	
		s-PDMS	v-PDMS	s-PDMS	v-PDMS
PHMS	0	1.90 ± 0.05		2.01 ± 0.05	
PHMS	10	1.73 ± 0.02	1.90 ± 0.02	1.90 ± 0.02	2.01 ± 0.02
PHMS	20	1.65 ± 0.01	1.98 ± 0.05	1.84 ± 0.01	2.05 ± 0.05
PHMS	30	1.20 ± 0.02	1.90 ± 0.03	1.96 ± 0.01	2.05 ± 0.03
PSO	0	1.76 ± 0.01		1.88 ± 0.01	

PSO	10	1.59 ± 0.01	1.72 ± 0.01	1.77 ± 0.01	1.79 ± 0.01
PSO	20	1.51 ± 0.01	1.57 ± 0.01	1.83 ± 0.01	1.66 ± 0.01
PSO	30	1.44 ± 0.01	1.34 ± 0.01	1.79 ± 0.01	1.45 ± 0.01

For the PSO/s-PDMS samples, the bulk densities decrease with increasing s-PDMS concentration while the apparent density remains relatively the same, again indicating that the open porosity is much more affected than the closed porosity by the s-PDMS samples. With the addition of v-PDMS to the PSO, both the bulk and apparent densities decrease, indicating that both the open and closed pore volumes increase with increasing v-PDMS content.

The density values listed in Table 4.1 can be used to compute the open porosity V_{op}, closed porosity V_{cp}, and total porosity V_{tp}, of the samples using the following equations:

$$V_{op} = 100(1-\rho_b/\rho_a) \quad (4.1)$$

$$V_{tp} = 100(1-\rho_b/\rho_t) \quad (4.2)$$

$$V_{cp} = V_{tp} - V_{op} \quad (4.3)$$

The true density for the base PHMS and PSO samples can be assumed to be equal to their measured apparent densities given that neither sample contains significant closed porosity [5, 19, 28]. Furthermore, the true densities of the samples with PDMS can be assumed to be equal to the true densities of their PHMS or PSO base samples since the majority of the PDMS should decompose and thus not affect the true density of the remaining ceramic; therefore, the true density is estimated to be 2.01 g/cm^3 for all of the PHMS samples and 1.88 g/cm^3 for all of the PSO samples. Fig. 4.7 shows the results after applying Eqs. (4.1)-(4.3) to the density values in Table 4.1. For the pyrolyzed PSO and PHMS samples, the calculated total porosity is ~5%, which is most likely due to the cracks on the sample surface. With the addition of s-PDMS to PHMS (Fig. 4.7(a)), the porosity increases to 18% for the 20s-PDMS sample. The total porosity then increases greatly to 40% for the 30s-PDMS sample due to the phase inversion as previously discussed. Comparatively, the PHMS/v-PDMS samples show no significant change in porosity for the 10-30 wt% v-PDMS samples. This result indicates that all the pores created by the v-PDMS decomposition have closed during pyrolysis. It should be noted that both the open porosity and total porosity for the PHMS samples with v-PDMS overlap in Fig. 4.7(a) due to the absence of closed porosity within the samples.

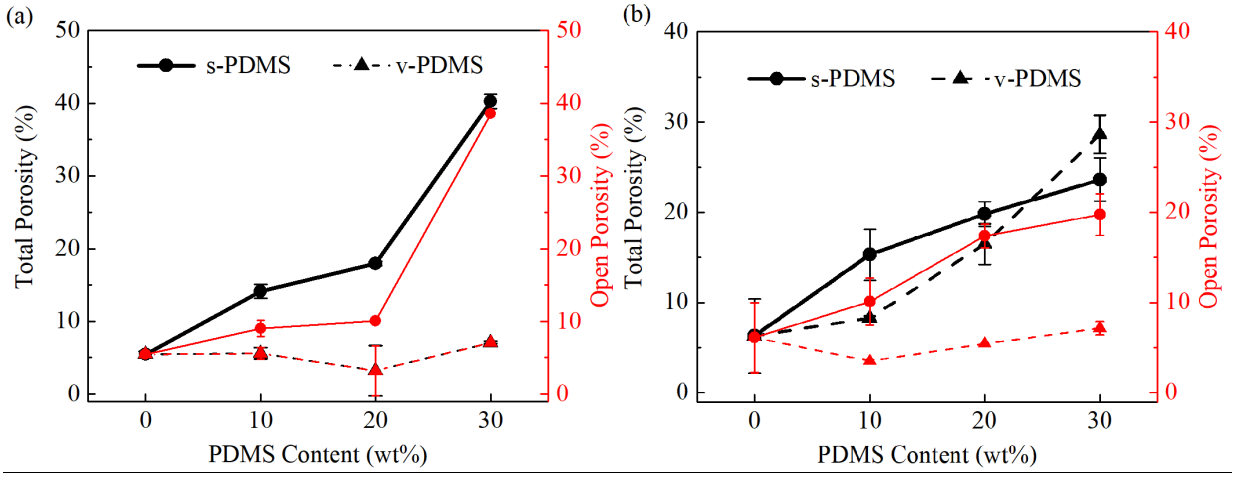

Fig. 4.7 Open and total porosities for (a) PHMS, and (b) PSO base polymers.

For the PSO samples, the s-PDMS and v-PDMS polymers show distinct differences in open and total porosity trends (Fig. 4.7(b)). Addition of s-PDMS to the PSO matrix causes a continual increase in open porosity and total porosity, with the PSO-30s sample containing 24% total porosity. The difference between the total porosity and open porosity is similar for the three s-PDMS samples, indicating that s-PDMS strongly affects open porosity while maintaining similar closed porosity, and there is minimal interaction between PSO and s-PDMS and most s-PDMS escapes and leads to open pores during the pyrolysis. For the v-PDMS samples, the total porosity for the 10 wt% v-PSO sample is similar to that of the pure PSO sample. Increasing the v-PDMS content to 20 or 30 wt% causes a sharp increase in the total porosity, likely due to the lower interaction between the vinyl bonds in the v-PDMS and the hydrogen bonds in the PSO as already discussed in Section 4.4.2. Interestingly, the v-PDMS polymer affects the closed porosity much more strongly than the open porosity, showing an opposite trend to the s-PDMS polymer.

Fig. 4.8 shows the cross sections of the PHMS-s-PDMS and PHMS-v-PDMS samples after pyrolysis. With 10 wt% s-PDMS addition, the sample shows uniform, featureless microstructures. With 20 wt% s-PDMS addition, the sample has much larger pores, with the size ranging from 5 – 30 μm and a few pores reaching ~50 μm. As already discussed, the 30 wt% s-PDMS sample shows an inversion of the microstructure, with the pyrolyzed PHMS phase being made of loosely bonded spheres; the spheres have a bimodal size with the smaller spheres reaching approximately 10 μm and the larger spheres having diameters of several hundred microns.

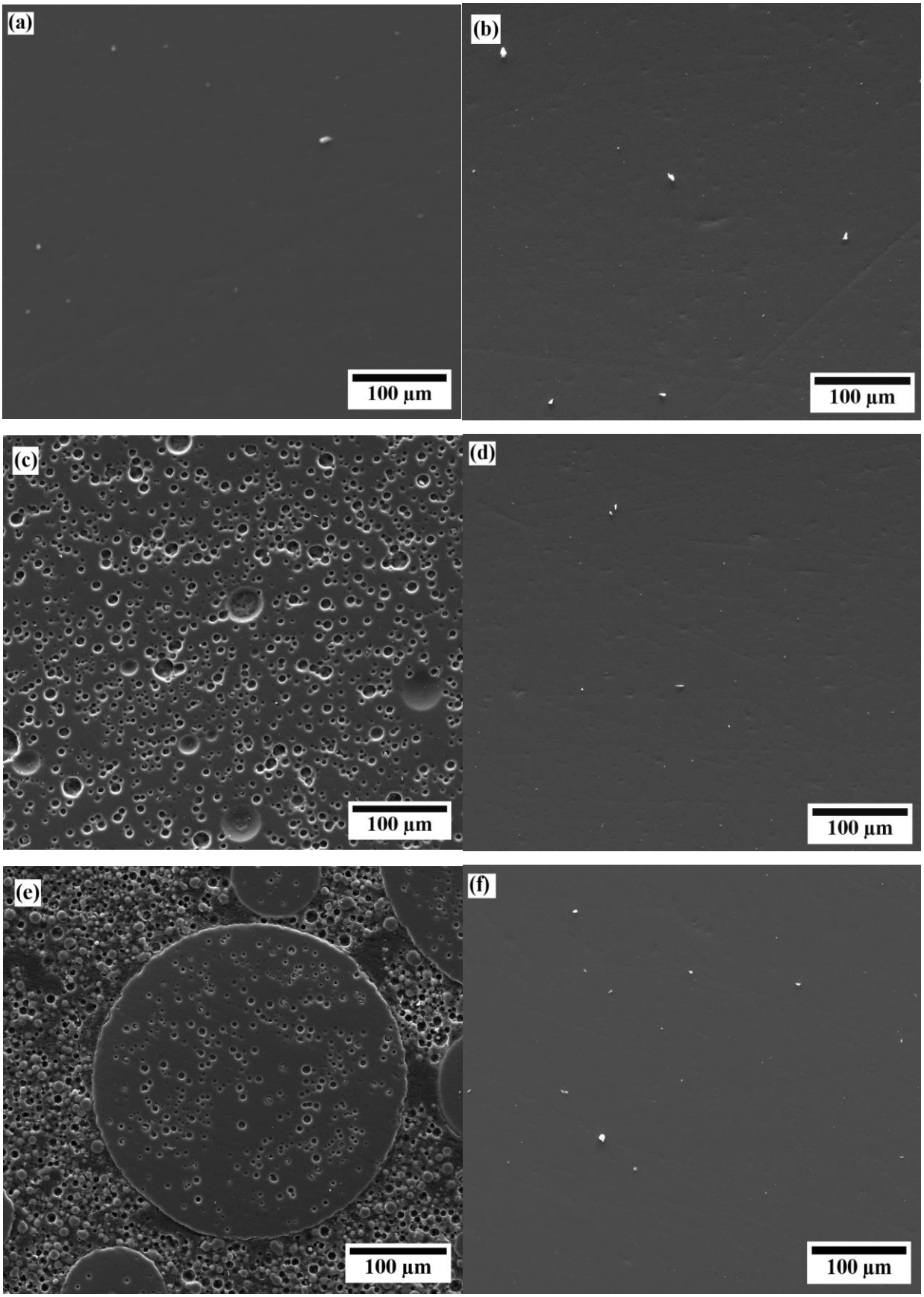
(a)
100 µm
(b)
100 µm
(c)
100 µm
(d)
100 µm
(e)
100 µm
(f)
100 µm

Fig. 4.8 SEM micrographs of pyrolyzed samples (a) PHMS-10s, (b) PHMS-10v, (c) PHMS-20s, (d) PHMS-20v, (e) PHMS-30s, and (f) PHMS-30v.

After pyrolysis, for the PHMS samples with v-PDMS, the pore size with 10 wt% addition shows a similar featureless microstructure as for the PHMS with 10 wt% s-PDMS sample. However, the addition of higher amounts of v-PDMS does not show any significant changes to the microstructure (different from the corresponding s-PDMS samples), confirming the lack of porosity as measured with the Archimedes method. The reason for this observation with the v-PDMS samples can be understood by considering that the vinyl bonds within the v-PDMS sample react with the hydrogen bonds in the PHMS during crosslinking. Since the total molecular weight of the v-PDMS polymer is 28000 g/mol with 7-8 mol% vinylmethylsiloxane, then the average molecular weight of the PDMS chains between vinylmethylsiloxane molecules (or crosslinks) is approximately 900 g/mol, assuming that the vinylmethylsiloxane units are evenly distributed along the PDMS chains. For the PDMS polymers within the PHMS matrix, the conformation of the PDMS molecules can be assumed to be ideal; and the dependence of R_g for the PDMS molecules on the polymer molecular weight was determined by neutron scattering studies to be [39]:

$$R_g = 0.025M^{0.5} \text{ (nm)} \quad (4.5)$$

The pore diameter left from the decomposition of PDMS molecules would simply be twice the value obtained from Eq. (4.5). Thus, if the average molecular weight between crosslinks for the v-PDMS molecules within the PHMS matrix is 900 g/mol, then the pore size would be approximately 1.5 nm following Eq. (4.5). Such small pores have been shown to easily close at higher temperatures, resulting in minimal porosity [24]. This hypothesis is further confirmed by considering the higher linear shrinkage of the v-PDMS samples in Fig. 4.6(a) versus the PHMS or PHMS-s-PDMS samples.

To further examine whether microporosity may have arisen from the decomposition of the PDMS molecules, nitrogen adsorption was conducted on the pure PHMS and PSO samples as well as the samples with 20 wt% s-PDMS or v-PDMS, all after pyrolysis; the samples were first etched with a HF solution to remove SiO_2 from the samples and open the structure to allow for any closed pores from the PDMS decomposition to be available to the N_2 gas. The resulting pore size distributions for the samples (Fig. 4.9) show that no significant porosity can be observed other than that arising from the etching of the SiO_2 at ~ 1.6 nm and 3.5 nm. Thus, there is no significant

residual microporosity from the decomposition of the s-PDMS and v-PDMS in either the PHMS or PSO.

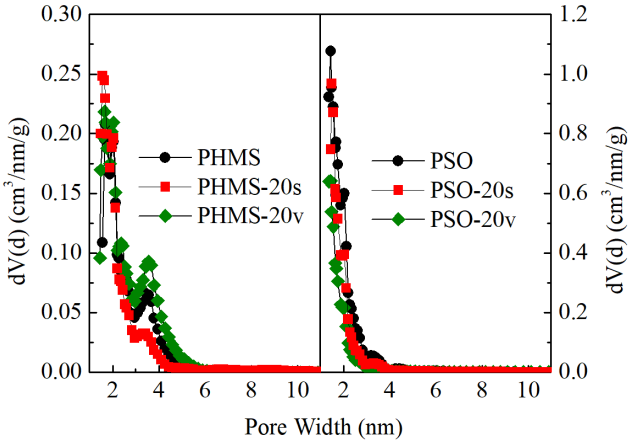

Fig. 4.9 Pore size distributions for the pure PHMS and PSO polymers after pyrolysis as well as the samples with 20 wt% PDMS additions.

The microstructures for the PSO-s-PDMS and PSO-v-PDMS mixtures after pyrolysis are shown in Fig. 4.10. The PSO-10s sample has a pore size range between 3 – 20 µm. The PSO-20s sample has a similar pore size range, with the only difference being the concentration of pores within the sample. An increase of the s-PDMS content to 30 wt% causes a much more drastic increase in the pore size to 20 – 50 µm, with a small concentration of pores still being 5 – 10 µm in diameter. Similar to the PSO-10s sample, the pore size for the PSO-10v sample is in the range of 3 – 20 µm. With an increase of the v-PDMS content, both the pore size and pore size distribution increase, with the pore size ranging from 5 – 30 µm for both the PSO-20v and PSO-30v samples. This means that at higher concentrations of the v-PDMS, the pore formation more closely resembles that from the s-PDMS.

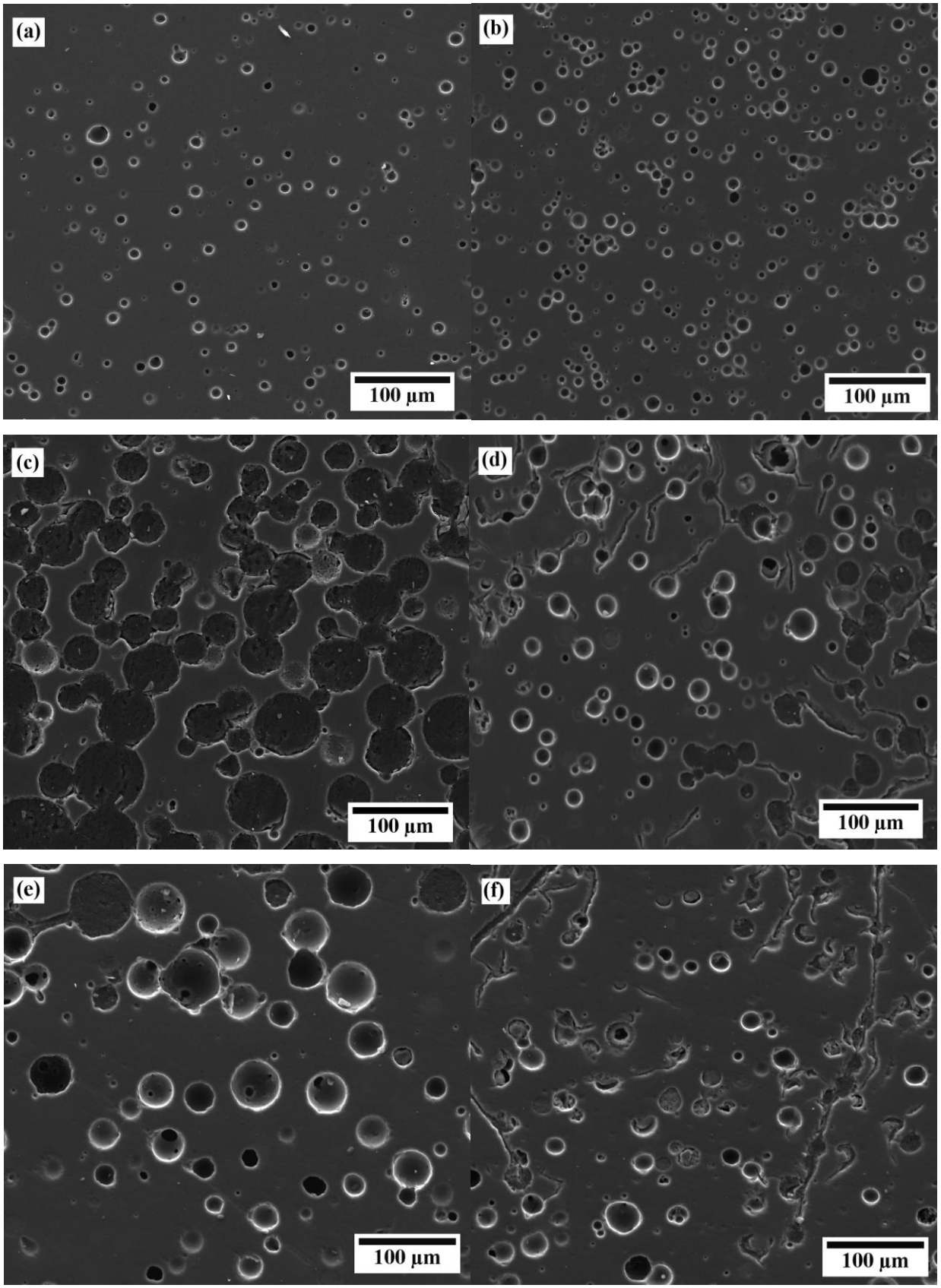
(a)
100 µm
(b)
100 µm
(c)
100 µm
(d)
100 µm
(e)
100 µm
(f)
100 µm

Fig. 4.10 SEM micrographs of pyrolyzed samples: (a) PSO-10s, (b) PSO-10v, (c) PSO-20s, (d) PSO-20v, (e) PSO-30s, and (f) PSO-30v.

To further investigate the difference between the pore sizes for the PSO samples with s-PDMS and v-PDMS additions, the pore size distributions for the samples were obtained through image analysis of the SEM microstructures such as those shown in Fig. 4.10. The pore size measurements were not carried out for the PHMS samples due to the fact that only the PHMS-20s sample contains measureable porosity; the PHMS-10s and all of the PHMS-v samples contain negligible porosity, and the phase inversion for the PHMS-30s sample prevents any measurement of the PDMS phase. Figs. 4.11(a) and (b) show the area probability density, or the derivative of the cumulative pore area, for the PSO-PDMS samples. For the PSO-10s sample, the pore size distribution is wide and spans from 5 - 50 μm with a mode size of ~30 μm. Increasing the s-PDMS content to 20 wt% causes the pore size distribution to further widen, with the modes occurring at 35 μm and 65 μm. For the PSO-30s sample, the modes are at 20 μm, 50 μm, 75 μm, and 85 μm.

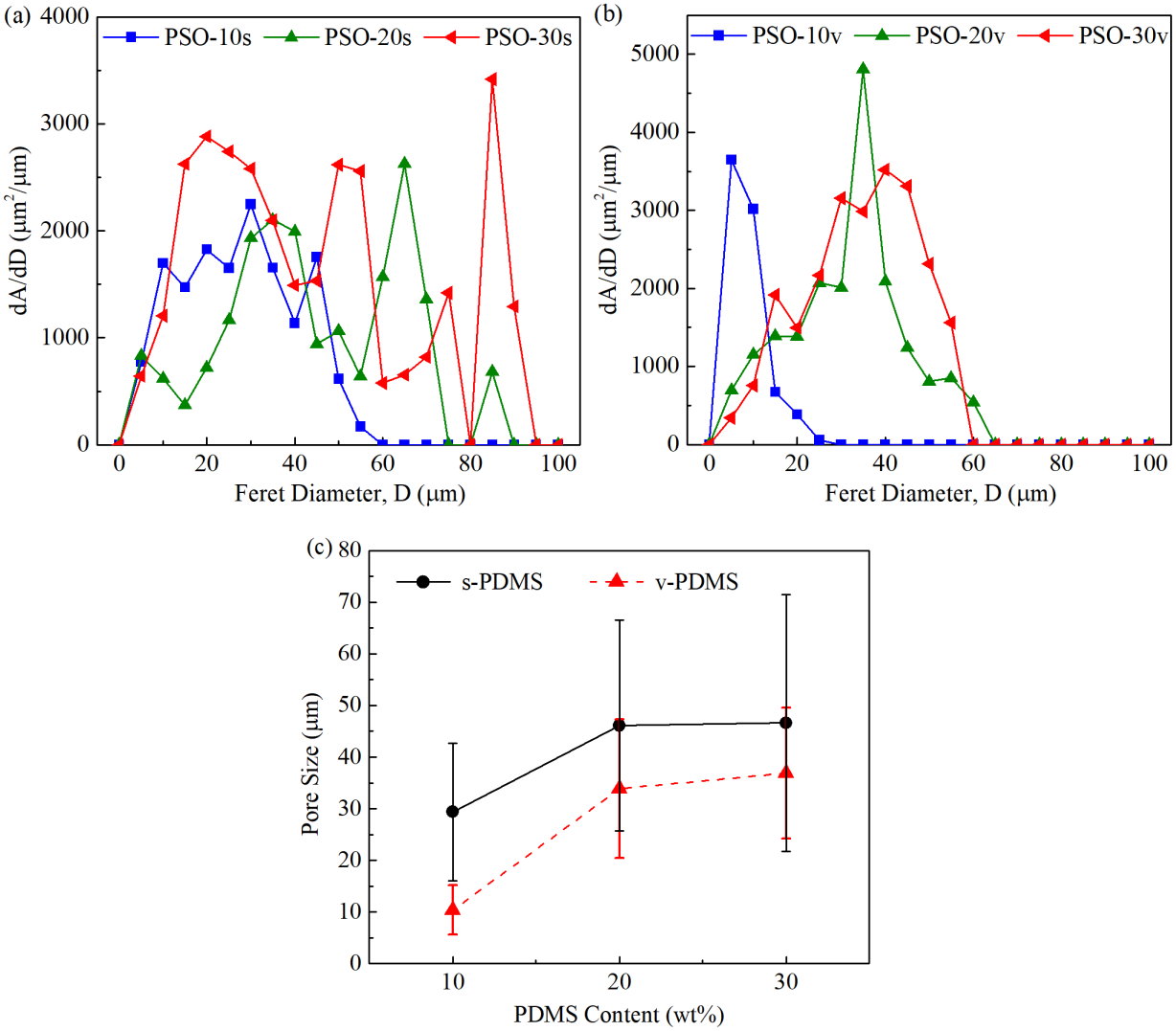

Fig. 4.11 Pore size distributions obtained from the SEM image analysis for PSO with: (a) s-PDMS, and (b) v-PDMS. (c) Average pore size for the PSO-s and PSO-v samples.

The pore size distributions for the PSO with v-PDMS in Fig. 4.11(b) all display narrower pore size distributions and smaller pore sizes than those for the s-PDMS samples. For the PSO-10v sample, the mode pore size is only 5 μm, and the sample contains no pores larger than 30 μm. Increasing the v-PDMS content to 20 wt% again causes the pore size distribution to broaden and increases the mode pore size to 35 μm. The PSO-30v sample has a similar pore size distribution to the PSO-20v sample, with the mode pore size only increasing to 40 μm.

The average pore size and standard deviation for each of the PSO-PDMS samples are shown in Fig. 4.11(c). For the s-PDMS, the average pore size increases from 29.4 μm for the PSO-

10s to 46.1 μm for the PSO-20s and then to 46.6 μm for the PSO-30s. The v-PDMS similarly increases with the PDMS content from 10.4 μm for the PSO-10v to 33.9 μm and 36.9 for the PSO-20v and PSO-30v, respectively. However, the standard deviations for the v-PDMS samples are much smaller than for the s-PDMS samples for each of the PDMS contents. The smaller pore sizes and narrower pore size distributions for the v-PDMS samples compared to the s-PDMS samples can only be attributed to the vinyl bonds within the v-PDMS, since both the molecular weight and the viscosity of the two types of PDMS are identical. As already seen from the TGA data in Fig. 4.5, the v-PDMS sample shows a different decomposition behavior than the s-PDMS sample due to the reactions from the vinyl group. Accordingly, these reactions may slightly prevent such extensive phase separation between the PSO and v-PDMS molecules. The reactions from the vinyl bonds along the v-PDMS chain may also effectively reduce the molecular weight of the PDMS molecules; the added connection points shorten the length of the free PDMS chains, reducing the PDMS molecular weight as already discussed for the PHMS/v-PDMS system. Both reducing the extent of phase separation and reducing the PDMS molecular weight would lead to smaller pore sizes and a narrower size distribution.

If the phase separation between the base polymer and the PDMS molecules is significant, as it is for the PSO base, then the size of the PDMS domains will be much larger than that of single polymer chains as discussed previously, given by [33]:

$$d = \frac{4\sigma_{int}(p+1)}{\dot{\gamma}\eta_m\left(\frac{19p}{4}+4\right)} \tag{4.6}$$

where p is the viscosity ratio of the dispersed phase to the matrix phase, σ_{int} is the interfacial tension of the two polymers, η_m is the viscosity of the matrix polymer, and $\dot{\gamma}$ is the shear rate exerted on the system during mixing. If the polymer phases coalesce after mixing, then the polymer domains will increase in size according to the empirical relationship [33, 40]:

$$d = \frac{4\sigma_{int}}{\dot{\gamma}\eta_m}(p)^{-0.84} \tag{4.7}$$

The measured viscosities of the PSO, s-PDMS, and v-PDMS are 10.7 ± 0.1 Pa s, 1.0 ± 0.1 Pa s, and 1.0 ± 0.1 Pa s, respectively. The interfacial tension is estimated to be ~0.00058 N/m, which is the value between PDMS and a poly(dimethylsiloxane-ran-methylphenylsiloxane), similar to the PSO used in this study [33]. Fig. 4.12 shows the result based on Eqs. (4.6) and (4.7) vs. the shear rate during mixing as well as the average pore sizes. Considering that the shear rate

during the vibratory milling of the polymers is much greater than 1 1/s, then Eq. (4.7) more closely estimates the experimental pore sizes at a shear rate of approximately 40 1/s. Eq. (4.6) is based off the initial size of the polymer domains directly after mixing, while Eq. (4.7) takes into account coalescence of the domains after mixing, matching with the experimental results, since the PSO-PDMS mixtures were allowed to sit in the oven before reaching gelation.

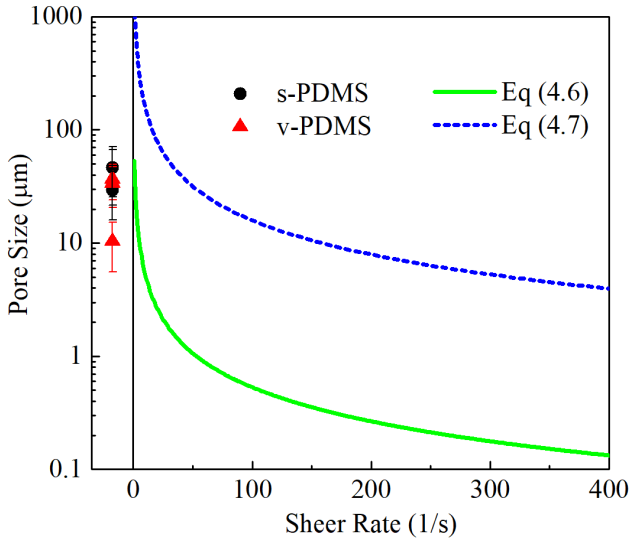

Fig. 4.12 Calculated pore size versus shear rate during mixing from Eqs. (4.6) and (4.7), and the experimental pore sizes from Fig. 4.9(c).

4.5 Conclusions

Pores and porosity arising from the decomposition of PDMS have been studied for a fully saturated PDMS (s-PDMS) and a PDMS copolymer containing vinyl bonds (v-PDMS). The s-PDMS produces lower yields than the v-PDMS and higher porosity when added to PSO and PHMS base polymers, regardless of the content of hydrogen bonds in the base polymer. When crosslinked with the PHMS base, the v-PDMS does not show large scale phase separation, is more thermally stable than the s-PDMS, and produces no significant porosity. For low contents of v-PDMS crosslinked with the PSO base, the yield is higher and the porosity is lower compared to the corresponding s-PDMS samples, but the differences between the two PDMS types decreases as the PDMS content increases. For the PSO base containing no excess hydrogen bonds, the pores resulting from the PDMS decomposition are micron sized for both the s-PDMS and v-PDMS

polymers. However, the PSO with v-PDMS produces smaller pores with a narrower pore size distribution than the s-PDMS, which is attributed to the vinyl bonds within the v-PDMS producing reactions and effectively reducing the polymer molecular weight. The fundamental differences between the interaction of the PDMS molecules and the base polymers based on the vinyl content are discussed to provide a practical guide for polymer selection.

References

1. Colombo P. Engineering porosity in polymer-derived ceramics. *J Eur Ceram Soc* **2008**, *28*, 1389-1395.
2. Colombo P, Mera G, Riedel R, Soraru GD. Polymer-derived ceramics: 40 years of research and innovation in advanced ceramics. *J Am Ceram Soc* **2010**, *93*, 1805-1837.
3. Yu ZJ, Feng Y, Li S, Pei YX. Influence of the polymer-polymer miscibility on the formation of mesoporous SiC(O) ceramics for highly efficient adsorption of organic dyes. *J Eur Ceram Soc* **2016**, *36*, 3627-3635.
4. Soraru GD, Modena S, Guadagnino E, Colombo P, Egan J, Pantano C. Chemical durability of silicon oxycarbide glasses. *J Am Ceram Soc* **2002**, *85*, 1529-1536.
5. Lu K, Erb D, Liu MY. Thermal stability and electrical conductivity of carbon-enriched silicon oxycarbide. *J Mater Chem C* **2016**, *4*, 1829-1837.
6. Lu K, Erb D, Liu MY. Phase transformation, oxidation stability, and electrical conductivity of TiO_2-polysiloxane derived ceramics. *J Mater Sci* **2016**, *51*, 10166-10177.
7. Vakifahmetoglu C, Zeydanli D, Colombo P. Porous polymer derived ceramics. *Mater Sci Eng R Rep* **2016**, *106*, 1-30.
8. Pan JM, Yan XH, Cheng XN, Lu QB, Wang MS, Zhang CH. Preparation of SiC nanowires-filled cellular SiCO ceramics from polymeric precursor. *Ceram Int* **2012**, *38*, 6823-6829.
9. Ceron-Nicolat B, Fey T, Greil P. Processing of ceramic foams with hierarchical cell structure. *Adv Eng Mater* **2010**, *12*, 884-892.
10. Vakifahmetoglu C, Zeydanli D, Innocentini MDD, Ribeiro FD, Lasso PRO, Soraru GD. Gradient-hierarchic-aligned porosity SiOC ceramics. *Sci Rep* **2017**, *7*.

11. Zeschky J, Hofner T, Arnold C, Weissmann R, Bahloul-Hourlier D, Scheffler M, Greil P. Polysilsesquioxane derived ceramic foams with gradient porosity. *Acta Mater* **2005**, *53*, 927-937.
12. Bhattacharjee S, Das PR, Ohl C, Wilker V, Kappa M, Scheffler F, Scheffler M. Novel-type inorganic foams from preceramic polymers with embedded titania nanoparticles for photo-catalytic applications. *Adv Eng Mater* **2011**, *13*, 996-1001.
13. Ohl C, Kappa M, Wilker V, Bhattacharjee S, Scheffler F, Scheffler M. Novel open-cellular glass foams for optical applications. *J Am Ceram Soc* **2011**, *94*, 436-441.
14. Wen GW, Bai HW, Huang XX, Han ZX. Lotus-type porous SiOCN ceramic fabricated by undirectional solidification and pyrolysis. *J Am Ceram Soc* **2011**, *94*, 1309-1313.
15. Zhang HX, Fidelis CL, Wilhelm M, Xie ZP, Rezwan K. Macro/mesoporous SiOC ceramics of anisotropic structure for cryogenic engineering. *Mater Design* **2017**, *134*, 207-217.
16. Zhang HX, Fidelis CL, Serva ALT, Wilhelm M, Rezwan K. Water-based freeze casting: Adjusting hydrophobic polymethylsiloxane for obtaining hierarchically ordered porous SiOC. *J Am Ceram Soc* **2017**, *100*, 1907-1918.
17. Biasetto L, Pena-Alonso R, Soraru GD, Colombo P. Etching of SiOC ceramic foams. *Adv Appl Ceram* **2008**, *107*, 106-110.
18. Peña-Alonso R, Sorarù GD, Raj R. Preparation of ultrathin-walled carbon-based nanoporous structures by etching pseudo-amorphous silicon oxycarbide ceramics. *J Am Ceram Soc* **2006**, *89*, 2473-2480.
19. Li JK, Lu K, Lin TS, Shen FY. Preparation of micro-/mesoporous SiOC bulk ceramics. *J Am Ceram Soc* **2015**, *98*, 1753-1761.
20. Li JK, Lu K. Highly porous SiOC bulk ceramics with water vapor assisted pyrolysis. *J Am Ceram Soc* **2015**, *98*, 2357-2365.
21. Erb D, Lu K. Additive and pyrolysis atmosphere effects on polysiloxane-derived porous SiOC ceramics. *J Eur Ceram Soc* **2017**, *37*, 4547-4557.
22. Yang J, Wu HL, Zhu M, Ren WJ, Lin Y, Chen HB, Pan F. Optimized mesopores enabling enhanced rate performance in novel ultrahigh surface area meso-/microporous carbon for supercapacitors. *Nano Energy* **2017**, *33*, 453-461.
23. Vakifahmetoglu C, Colombo P. A direct method for the fabrication of macro-porous SiOC ceramics from preceramic polymers. *Adv Eng Mater* **2008**, *10*, 256-259.

24. Blum Y, Soraru GD, Ramaswamy AP, Hui D, Carturan SM. Controlled mesoporosity in SiOC via chemically bonded polymeric "spacers". *J Am Ceram Soc* **2013**, *96*, 2785-2792.
25. Yan X, Su D, Han SS. Phase separation induced macroporous SiOC ceramics derived from polysiloxane. *J Eur Ceram Soc* **2015**, *35*, 443-450.
26. Wu JQ, Li YM, Chen LM, Zhang ZB, Wang D, Xu CH. Simple fabrication of micro/nano-porous SiOC foam from polysiloxane. *J Mater Chem* **2012**, *22*, 6542-6545.
27. Janakiraman N, Aldinger F. Fabrication and characterization of fully dense Si-C-N ceramics from a poly (ureamethylvinyl) silazane precursor. *J Eur Ceram Soc* **2009**, *29*, 163-173.
28. Martinez-Crespiera S, Ionescu E, Kleebe HJ, Riedel R. Pressureless synthesis of fully dense and crack-free SiOC bulk ceramics via photo-crosslinking and pyrolysis of a polysiloxane. *J Eur Ceram Soc* **2011**, *31*, 913-919.
29. Schneider CA, Rasband WS, Eliceiri KW. NIH image to ImageJ: 25 years of image analysis. *Nat Methods* **2012**, *9*, 671-675.
30. Hourlier D, Venkatachalam S, Ammar MR, Blum Y. Pyrolytic conversion of organopolysiloxanes. *J Anal Appl Pyrolysis* **2017**, *123*, 296-306.
31. Sakaki S, Mizoe N, Sugimoto M. Theoretical study of platinum(0)-catalyzed hydrosilylation of ethylene. Chalk-harrod mechanism or modified chalk-harrod mechanism. *Organometallics* **1998**, *17*, 2510-2523.
32. Stammer A, Wolf BA. Effect of random copolymer additives on the interfacial tension between incompatible polymers. *Macromol Rapid Commun* **1998**, *19*, 123-126.
33. Ziegler V, Wolf BA. Viscosity and morphology of the two-phase system PDMS/P(DMS-ran-MPS). *J Rheol* **1999**, *43*, 1033-1045.
34. Boots HMJ, Kloosterboer JG, Serbutoviez C, Touwslager FJ. Polymerization-induced phase separation. 1. Conversion-phase diagrams. *Macromolecules* **1996**, *29*, 7683-7689.
35. Serbutoviez C, Kloosterboer JG, Boots HMJ, Touwslager FJ. Polymerization-induced phase separation. 2. Morphology of polymer-dispersed liquid crystal thin films. *Macromolecules* **1996**, *29*, 7690-7698.
36. Camino G, Lomakin SM, Lageard M. Thermal polydimethylsiloxane degradation. Part 2. The degradation mechanisms. *Polymer* **2002**, *43*, 2011-2015.

37. Camino G, Lomakin SM, Lazzari M. Polydimethylsiloxane thermal degradation - part 1. Kinetic aspects. *Polymer* **2001**, *42*, 2395-2402.
38. Nyczyk-Malinowska A, Wojcik-Bania M, Gumula T, Hasik M, Cypryk M, Olejniczak Z. New precursors to SiCO ceramics derived from linear poly(vinylsiloxanes) of regular chain composition. *J Eur Ceram Soc* **2014**, *34*, 889-902.
39. Gilra N, Cohen C, Briber RM, Bauer BJ, Hedden RC, Panagiotopoulos AZ. A SANS study of the conformational behavior of linear chains in compressed and uncompressed end-linked elastomers. *Macromolecules* **2001**, *34*, 7773-7782.
40. Wu SH. Formation of dispersed phase in incompatible polymer blends - interfacial and rheological effects. *Polym Eng Sci* **1987**, *27*, 335-343.

5 Conclusions and Future Work

5.1 Conclusions

In this thesis, porous SiOC ceramics were fabricated based on phase separation, either through phase separation of the ceramic matrix during pyrolysis or phase separation of the polymer precursors during crosslinking.

Porous silicon oxycarbide (SiOC) ceramics were fabricated from a base polysiloxane (PSO) system by using different additives (polymethylphenylsiloxane, polydimethylsiloxane, polyhydromethylsiloxane, tetramethyl orthosilicate, and tetraethyl orthosilicate) and pyrolysis atmospheres (Ar and Ar+H_2O) followed by hydrofluoric acid (HF) etching, which produced open porosity. The additives modified the Si:O:C ratios within the polymers and thus influenced the microstructural evolution within the SiOC. Additives that were lower in carbon content, such as polyhydromethylsiloxane, had larger pores after etching, indicating larger SiO_2 nanodomains. The SiOC ceramics contained significantly less SiC and more SiO_2 after pyrolysis in an Ar+H_2O atmosphere compared to an Ar atmosphere. Water vapor injection during pyrolysis also caused a drastic increase in specific surface areas and pore volumes after etching. Further, the tetraethyl orthosilicate additive was successfully in-situ converted to SiO_2 with the Ar+H_2O atmosphere, causing a significant increase in the specific surface area.

The effects of additive structures on the nucleation and growth of SiO_2 within SiOC ceramics were investigated by adding 0 - 40 wt% of cyclic tetramethyl-tetravinylcyclotetrasiloxane (TMTVS) or caged octavinyl-polyhedral oligomeric silsesquioxane (POSS) to a linear PSO and crosslinked. The effects of the two additives on the polymer-to-ceramic transformation and the phase formation within the SiOC at pyrolysis temperatures between 1100°C-1400°C were discussed. The caged POSS structure improved the ceramic yield and increased the onset of thermal decomposition, while the cyclic TMTVS negatively affected both. POSS also encourages SiO_2 nucleation at temperatures as low as 1100°C, resulting in higher mass loss from the HF etching than those of the PSO or TMTVS samples. For the samples pyrolyzed at 1300°C, both TMTVS and POSS had little effect on the pore size after etching, with the average pore size remaining < 2 nm. At 1400°C, the POSS samples had increased growth of the SiO_2 phase compared to the TMTVS or PSO.

The influence of vinyl bonds on the phase separation and decomposition of polydimethylsiloxane (PDMS) was investigated for a fully saturated PDMS (s-PDMS) and an unsaturated poly(dimethylsiloxane-co-vinylmethylsiloxane) (v-PDMS) with the same molecular weight, and the resulting pore sizes were investigated for two base polymer systems, one with an excess of hydrogen bonds, polyhydromethylsiloxane (PHMS), and one with stoichiometric hydrogen to vinyl bonds, PSO. For the PHMS base, the samples with s-PDMS had lower ceramic yield and higher total porosity, while the samples with v-PDMS contained nearly no porosity after pyrolysis to 1300°C due to a more extensive hydrosilylation reaction between the hydrogen and vinyl groups in the preceramic polymer. For the PSO base, both s-PDMS and v-PDMS produced micron-sized pores, but the v-PDMS produced smaller pores with a narrower size distribution than the s-PDMS, which was attributed to the vinyl bonds within the v-PDMS producing reactions during either crosslinking or pyrolysis and effectively reducing the polymer molecular weight.

5.2 Future Work

In studying the effects of water vapor injection during pyrolysis, pure siloxane polymers containing a majority of hydrogen, methyl, vinyl, phenyl, etc. bonds can be fabricated rather than mixing a small amount of each type of polymer with a base polymer. These pure polymers can be synthesized by simply using polymers with vinyl end groups, which are commercially readily available, and mixing with a small fraction of a hydrogen containing polymer such as polyhydromethylsiloxane. Using these purer polymers would more easily allow for the determination of the effects of water vapor on each of the separate side group types.

Further study of the change in structure within the SiOC ceramics as a function of additive materials, pyrolysis temperatures, and pyrolysis atmospheres can be studied using ^{29}Si NMR, which would give information on the relative quantities of SiO_xC_{4-x} tetrahedral bonds within the ceramics.

Since the fabrication techniques and various polymer precursors and their effects on the structure of the resulting SiOC ceramics have been extensively studied, further testing into the properties of the materials can be conducted to further understand the processing-structure-properties relationships and pursue applications. For example, the electrochemical behavior of the microporous and mesoporous SiOC ceramics in Chapters 2 and 3 can be studied for use in lithium

ion batteries, and the thermal properties, such as thermal conductivity and heat capacity, of the macroporous SiOC ceramics in Chapter 4 can be studied for application as a thermal barrier.

Publications

1. Lu K, **Erb D**, Liu M. Thermal stability and electrical conductivity of carbon-enriched silicon oxycarbide. *J Mater Chem C* **2016**, *4*, 1829-1837. DOI: https://doi.org/10.1039/C6TC00069J.
2. Lu K, **Erb D**, Liu MY. Phase transformation, oxidation stability, and electrical conductivity of TiO_2-polysiloxane derived ceramics. *J Mater Sci* **2016**, *51*, 10166-10177. DOI: https://doi.org/10.1007/s10853-016-0244-6.
3. **Erb D**, Lu K. Additive and pyrolysis atmosphere effects on polysiloxane-derived porous SiOC ceramics. *J Eur Ceram Soc* **2017**, *37*, 4547-4557. DOI: https://doi.org/10.1016/j.jeurceramsoc.2017.06.036.
4. Lu K, **Erb D**. Polymer derived silicon oxycarbide-based coatings. *Int Mater Rev* **2018**, *63*, 139-161. DOI: https://doi.org/10.1080/09506608.2017.1322247.
5. **Erb D**, Lu K. Influence of vinyl bonds from PDMS on the pore structure of polymer derived ceramics. *Mater Chem Phys* **2018**, *209*, 217-226. DOI: https://doi.org/10.1016/j.matchemphys.2018.01.078.
6. **Erb D**, Lu K. Effects of SiO_2-forming additive on polysiloxane derived SiOC ceramics. *Microporous Mesoporous Mater* **2018**, *266*, 75-82. DOI: https://doi.org/10.1016/j.micromeso.2018.02.034.
7. **Erb D**, Lu K. Effect of additive structure and size on SiO_2 formation in polymer derived SiOC ceramics. *J Am Ceram Soc* **2018**, Accepted. DOI: https://doi.org/10.1111/jace.15876.
8. Ma RX, **Erb D**, Lu K. Flash pyrolysis of polymer-derived SiOC ceramics. *J Eur Ceram Soc* **2018**, Accepted. DOI: https://doi.org/10.1016/j.jeurceramsoc.2018.07.010.
9. Ma RX, Lu K, **Erb D**. Effect of solvent in preparation of SiOC bulk ceramics. *Mater Chem Phys* **2018**, *218*, 140-146. DOI: https://doi.org/10.1016/j.matchemphys.2018.07.043.
10. **Erb D**, Lu K. Synthesis of SiOC using solvent-modified polymer precursors. *Mater Chem Phys* **2018**, Submitted.

Appendix A: Effects of SiO_2-forming Additive on Polysiloxane Derived SiOC Ceramics

A.1 Abstract

Novel ultrahigh surface area materials are highly desired for demanding applications such as high temperature catalysts, electrodes, and harsh environment sensors. In-situ conversion of tetraethyl orthosilicate (TEOS) into SiO_2 and its incorporation into silicon oxycarbide (SiOC) ceramics during polysiloxane ceramization are investigated by crosslinking TEOS within a polysiloxane matrix and introducing water vapor during pyrolysis. The effects of the TEOS-derived SiO_2 on the pyrolysis behavior, phase development, and the resulting porous SiOC are investigated. The SiOC with 10 wt% TEOS within the crosslinked polymer creates the highest specific surface area of ~2100 m^2/g with an average pore size of ~2 nm. The specific surface area and pore size distribution are correlated with the theoretical results from Voronoi diagram simulation and idealized model calculation.

A.2 Introduction

Silicon oxycarbide (SiOC) is a polymer derived ceramic through which polysiloxane polymer precursors undergo thermal decomposition and bond rearrangement, resulting in amorphous or nanocrystalline ceramics (or a mixture of both) with a wide range of tailorable properties, such as high temperature stability, oxidation resistance, and electrical conductivity, depending on the pyrolysis temperature and specific composition [1-3].

In general, porous SiOC can be fabricated with a wide range of pore sizes using several different processing routes before, during, or after pyrolysis, such as by using sacrificial fillers, sacrificial templating, direct foaming, polymer precursor phase separation, and selective removal of phases after pyrolysis [4-7]. However, to create ultrahigh surface areas, only controlled phase separation during pyrolysis and selective phase removal after pyrolysis at the nanocluster level are feasible means, which can create pores with less than 10 nm sizes and very narrow distributions.

Phase separation in an evolving SiOC system can be introduced using two different methods. The first is through phase separation of the polymer precursors during crosslinking.

When two or more immiscible polymers co-exist as liquid precursors, they will separate and form two distinct phases after crosslinking. One of the phases can then evaporate after cross-linking or decompose during pyrolysis, leaving behind pores. The SiOC ceramics created with this method have high specific surface areas at temperatures around 600°C. However, the specific surface area may decrease as the temperature increases due to the sintering of transient pores [4, 8]. The second method is by controlling phase evolution within SiOC during pyrolysis. At temperatures above 1100°C, the amorphous SiOC phase separates into free carbon and amorphous SiO_2 nanodomains along with SiOC units of different stoichiometry. Pyrolysis to even higher temperatures, e.g., greater than 1250°C, leads to further phase separation and thus more carbon and SiO_2, as well as nanocrystalline SiC [9, 10]. From this point forward, the pyrolysis temperature can significantly influence the phase separation and the separated domain sizes. After pyrolysis, certain ceramic phases can be etched away, such as using hydrofluoric acid (HF) to remove SiO_2 nanodomains or chlorine gas to remove SiC nanocrystals, leaving behind single nanometer pores [1, 11]. Therefore, nucleation and growth, concentration, and size of different ceramic phases within SiOC are critical factors influencing the final porous SiOC materials.

SiO_2 nanodomain sizes in SiOC are related to both system chemistry and processing conditions. From ~1000°C to ~1250°C, SiO_2 nanoclusters are the main separated phase along with turbostratic carbon. In this temperature range, the SiO_2 nanodomains largely remain amorphous but the corresponding sizes increase with pyrolysis temperature. Saha et al.[12] reported that the size of the SiO_2 nanodomains is also dependent on the Si:O elemental ratio of the SiOC, with larger Si:O ratios producing smaller domain sizes. The effect of polymer precursor molecular structure on the resulting SiO_2 domain size is shown by comparing a linear polymer, polyhydridomethylsiloxane (PHMS), and a cyclic polymer, 1,3,5,7-tetramethyl-1,3,5,7-tetracyclotetrasiloxane (TMTS), having the same chemical composition. After pyrolysis at 1400°C, the PHMS sample has only amorphous SiO_2, while the TMTS sample contains both amorphous and crystalline SiO_2 [13, 14]. After etching both samples with HF, the PHMS sample has a higher micropore volume compared to the TMTS sample due to the presence of smaller SiO_2 domains[13].

SiO_2 formation in SiOC can also be influenced by pyrolysis atmosphere, such as by introducing reactive species into the pyrolysis gas, e.g., H_2 or H_2O [15-18]. Our previous work demonstrated that injecting water vapor during the temperature range at which precursor bond

(chain) breaking occurs results in a dramatic decrease in carbon precipitation and an increase in Si-O-Si bond formation [7, 17, 18]. The resulting SiOC sample pyrolyzed at 1300°C after HF etching has a specific surface area of 2391.6 m^2/g, much greater than the specific surface area of the sample pyrolyzed in Ar at the same temperature, 630.41 m^2/g [18]. Liang et al.[15] investigated water vapor injection effects on the chemistry and atomic bonding of SiOC from 500°C to 1000°C. The samples pyrolyzed in the water vapor atmosphere have only about half the carbon content compared to the samples pyrolyzed in Ar, resulting in a reduction of SiC_4 and SiC_2O_2 structural units and an increase in SiO_4 units.

Additives can be introduced into the polymer precursor to further react with the pyrolysis atmosphere. By adding 10 wt% tetraethylorthosilicate (TEOS), a water reactive molecule, to a commercial polysiloxane and then pyrolyzing in an $Ar+H_2O$ atmosphere, the specific surface area of the SiOC after HF etching increases from 1108.5 m^2/g for the base polysiloxane to 1953.9 m^2/g for the sample with TEOS. Additionally, the average pore size of the 10 wt% TEOS sample is 1.66 nm, less than the 3.03 nm pore size of the polysiloxane sample [19]. However, the evolution of the TEOS during the polymer to ceramic transformation or its effect on the phase separation within SiOC is yet unknown; it is unclear whether the TEOS would interact with the SiOC system to form SiO_2 or experience SiO_2 nucleation and growth independently.

Understanding and creating highly porous SiOC is of high interest for fundamental understanding, such as addressing the questions related to SiO_2 nucleation and growth as well as molecular interactions of different precursors. Porous SiOC also has many exciting applications, e.g., electrodes in lithium ion batteries, catalyst supports, thermal barriers, gas separation membranes, and lightweight components [20-22]. In this work, micro- and meso-porous SiOC ceramics are fabricated through the addition of TEOS to a polysiloxane precursor and then pyrolysis in a water vapor-containing atmosphere. After pyrolysis, SiO_2 nanoclusters are etched with a HF solution to create single nanometer pores. The effects of the additive amount and pyrolysis temperature on the resulting pyrolysis behavior, phase evolution, specific surface area, and pores of the SiOC ceramic are studied.

A.3 Experimental procedures

A commercial polysiloxane (PSO, $[-Si(C_6H_5)_2O-]_3[-Si(CH_3)(H)O-]_2[-Si(CH_3)(CH=CH_2)O-]_2$, SPR-684, Starfire Systems, Inc., Gelest Inc., Schenectady, NY) was chosen as the base precursor, tetraethyl orthosilicate (TEOS, $Si(OC_2H_5)_4$, Sigma-Aldrich, St. Louis, MO) was used as the additive, and 2.1-2.4% platinum-divinyltetramethyldisiloxane complex in xylene (Pt catalyst, Gelest Inc., Morrisville, PA) was used as the catalyst.

First, solutions with PSO and either 0, 10, 20, 30, or 40 wt% TEOS were sonicated for 10 minutes and then mixed in a high energy mill (SPEX 8000M Mixer/Mill, SPEX SamplePrep, Metuchen, NJ) for 10 minutes to form a homogeneous mixture. Next, the Pt catalyst (1 wt% relative to PSO) was added, the mixtures were mixed again in the high energy ball mill for 5 minutes, and then poured into aluminum foil molds. The mixtures were placed into a vacuum chamber and vacuumed for 10 minutes at 200 Torr to remove any bubbles in the solutions. After that, the molds were put in an oven to crosslink at 50°C for 12 hrs and then at 120°C for 6 hrs. All solutions initially had slightly greater than the listed weight of TEOS added in order to account for the evaporation of the additive during processing: the actual content of TEOS added was 11, 22, 32, and 43 wt% for the 10, 20, 30, and 40 wt% samples, respectively. The samples were also sealed during the curing process to prevent additional loss of TEOS. The samples designated as 100PSO corresponded to the pure PSO sample; the samples with the additive were labelled as XTEOS, where X was from 10 wt% to 40 wt%, depending on the TEOS amount.

For pyrolysis, the crosslinked materials were first cut and polished into circular pieces roughly 10 mm in diameter and 2 mm in thickness. Next, the samples were placed into a zirconia crucible, covered on both sides with graphite mats in order to reduce friction during shrinkage and prevent warping,[23, 24] and put into a tube furnace (1730-20 Horizontal Tube Furnace, CM Furnaces Inc., Bloomfield, NJ). With an Ar flow rate of approximately 500 std cm^3/min, the samples were heated up to 1100°C, 1300°C, or 1400°C at a rate of 1°C/min, held for 2 hrs, cooled to 400°C with a rate of 1°C/min, and finally cooled to 50°C with a rate of 2°C/min. During heating from 500°C-700°C, the Ar gas was bubbled through water at 60°C, giving a gas flow with a Ar:H_2O molar ratio of approximately 5:1.

Etching of the bulk SiOC samples after pyrolysis was done using a HF solution (20 wt% HF in water). The HF solution was magnetically stirred at room temperature until there was no significant mass loss, taking approximately 4 days. The SiOC samples were then rinsed with deionized water and dried at 120°C. Bulk density of the samples after etching was determined

geometrically by dividing the mass after etching by the volume of the samples measured using the image analysis software ImageJ [25].

Ceramic yield was calculated by measuring the mass of the samples before and after the pyrolysis. The apparent density after pyrolysis was measured using the Archimedes method with water as the medium [26]. The phase compositions of the pyrolyzed samples were analyzed in an X'Pert PRO diffractometer (PANalytical B.V., EA Almelo, the Netherlands) with Cu Kα radiation. The JCPDS reference cards used to identify the crystalline phases were 00-039-1425 for SiO_2, 00-029-1129 for SiC, and 01-075-1621 for C. The chemical bonding was evaluated using Fourier Transform Infrared Spectroscopy (FT-IR) (Nicolet 8700 with Pike GladiATR attachment, Thermo Scientific, Waltham, MA) between 500 and 4000 cm^{-1} wavenumber with a resolution of 4 cm^{-1} and averaged between 64 scans. The specific surface area, pore size distribution, and specific pore volume of the pyrolyzed samples were evaluated using nitrogen adsorption at 77 K with a Quantachrome Autosorb-1 (Quantachrome Instrumenets, Boynton Beach, FL), and the samples were degassed before testing for 3 hrs at 300°C. The relative pressure range used to calculate the specific surface area using the BET method was determined using the procedure proposed by Rouquerol et al.[27]; the calculated specific surface area should be considered as the "BET-equivalent specific surface area" due to the complications of applying the BET theory to microporous materials. The pore size distribution and specific pore volume were derived by applying the Non Local Density Functional Theory (NLDFT) model for N_2 adsorption on carbon with cylindrical pores to the adsorption branch of the data [28]. Assuming cylindrical pores, the average pore size was estimated using $4000V_p/SSA$, where V_p is the specific pore volume, and SSA is the specific surface area [29].

Modelling of the SiOC microstructure after etching was computed using Voronoi software (Rhinoceros 5.0, Robert McNeel and Associates, Seattle, WA). First, a three dimensional Voronoi tessellation model was created, and spheres were then placed within the center of each Voronoi cell to represent pores (or SiO_2 nanodomains before etching) within the SiOC matrix. The pore size distributions used in the model were generated by first fitting the experimental pore size distributions from nitrogen adsorption with log-normal distributions. Random pore diameters corresponding to the fitted distributions were then generated using Mathematica software (Mathematica 11.0, Wolfram, Champaign, IL). After the generation of the cubes containing the Voronoi cells and corresponding pores, images along the length of the cube were taken in order to

produce 3D reconstructions of the samples (Amira 5.4.1, FEI, Hillsboro, OR), giving the specific surface area and pore volume of the simulated SiOC microstructures after the HF etching.

A.4 Results and Discussion

A.4.1 Pyrolysis Behavior

The ceramic yields of the SiOC samples are shown in Fig. A.1 as a function of the TEOS content at different pyrolysis temperatures. After pyrolysis at 1100°C, the ceramic yield decreases from 71.1% to 47.6% with the TEOS content increase from 0 to 40 wt%. The samples pyrolyzed at 1400°C also change similarly, even though in general the ceramic yield is lower, from 68.7% - 46.2% at 0 - 40 wt% TEOS addition. The yield results at 1300°C pyrolysis temperatures are in-between those at the other two pyrolysis temperatures with no significant difference. For all the samples, pyrolysis temperature causes only a slight decrease in the ceramic yield from 1100°C to 1300°C. From 1300°C to 1400°C, there is no significant yield change. Increasing the TEOS content causes a continuous decrease in the ceramic yield at all pyrolysis temperatures. This decrease can be attributed to the evaporation of TEOS from the sample at low pyrolysis temperatures, the hydrolysis and condensation of the TEOS molecules during the water vapor injection between 500°C - 700°C, and the evaporative species loss through Eqs. (A.1)-(A.9). At pyrolysis temperatures 1300°C and above, mass loss can also occur based on Eqs. (A.10)-(A.11) (Section A.4.2).

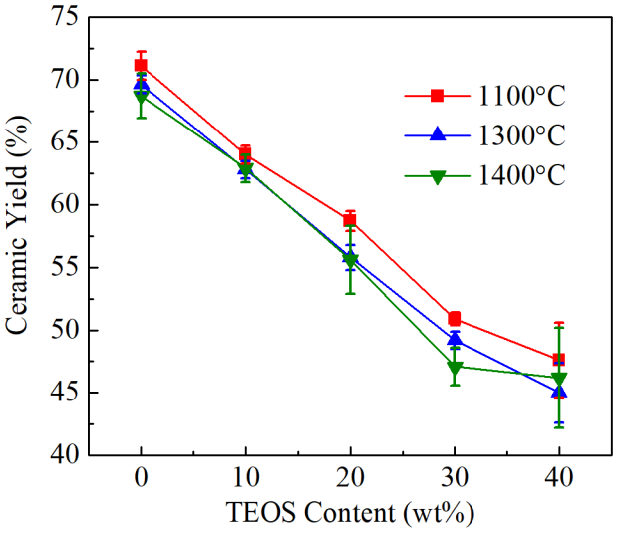

Fig. A.1 Ceramic yield of the SiOC samples after pyrolysis at different temperatures.

As understood from our earlier work [6, 18], at >1100°C pyrolysis temperature, there is continuous phase separation of SiO_2 and crystallization of SiC. Based on Eqs. (A.10) and (A.11) to be discussed later, the phase separation process may or may not induce mass loss due to the formation of CO gas. If the phase evolution follows Eq. (A.10), the mass of the SiOC sample should remain unchanged during the phase separation. If the phase evolution follows Eq. (A.11), the mass of the SiOC sample should decrease. However, for the system in this work, the mass loss is minimal, suggesting that the formation of SiC is very limited, as to be discussed later (Section A.4.2).

The apparent densities of the samples after pyrolysis between 1100°C and 1400°C vary from 1.62 ± 0.02 g/cm^3 to 1.87 ± 0.03 g/cm^3. There is no consistent trend or significant change with the pyrolysis temperature. For PSO, 10TEOS, and 20TEOS, the density ranges from 1.76 ± 0.06 g/cm^3 to 1.88 ± 0.01 g/cm^3. The 30TEOS and 40TEOS samples have slightly lower densities ranging between 1.62 ± 0.02 g/cm^3 to 1.83 ± 0.02 g/cm^3. The lower densities for the 30TEOS and 40TEOS samples is likely due to the more extensive evaporation of the TEOS molecules during the early stages of pyrolysis leaving behind macropores in the samples rather than a fundamental difference in the polymer to ceramic conversion, considering that lowering the PSO content in the polymer would cause a decrease in the carbon content in the ceramic, which should increase the density of the SiOC in this work [24]. The measured density values for the samples in this study are

in good agreement with those obtained from previous studies with the same PSO precursor (1.6 g/cm^3- 1.8 g/cm^3) [18, 19, 24].

A.4.2 Phase evolution

To understand the effect of the TEOS addition on the chemical bonding of the system, the FT-IR spectra of the crosslinked polymers are shown in Fig. A.2. In Fig. A.2(a), all the crosslinked samples show sharp peaks, corresponding to the phenyl (695, 715, 740, 1430, 3000-3070 cm^{-1}) and methyl (1260 cm^{-1}) side groups in the PSO polymer. The broad peak between 1000 and 1100 cm^{-1} wavenumbers can be assigned to Si-O-Si [30]. With the addition of TEOS, the peaks at 785, 1170, 1298, 1390, 1440, 2890, 2929, and 2975 cm^{-1} increase, indicative of increasing amounts of TEOS [31]. Fig. A.2(b) compares the C-H vibration at 2955 cm^{-1}, found only in PSO, and 2975 cm^{-1}, found only in TEOS, as the TEOS content in the polymer is increased. The continuous decrease of the 2955 cm^{-1} peak and increase of the 2975 cm^{-1} peak indicate that the concentration of TEOS within the crosslinked polymers increases from 10TEOS to 40TEOS, consistent with the designed composition changes.

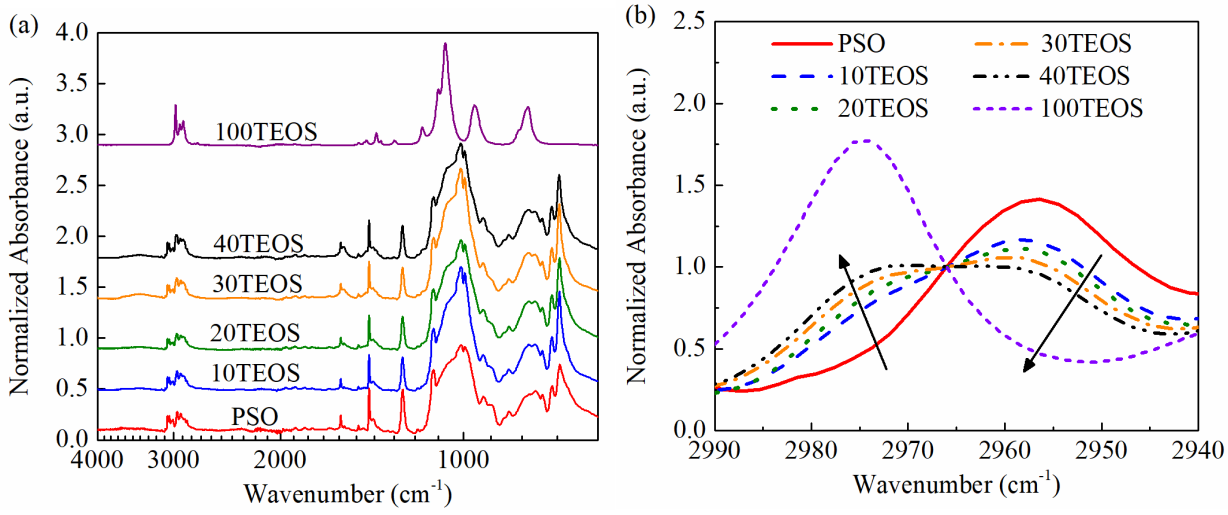

Fig. A.2 (a) Normalized FT-IR spectra for the PSO-TEOS precursors after crosslinking along with pure PSO and pure TEOS. (b) The spectra from (a) normalized to 2966 cm^{-1} to illustrate the effect of increasing TEOS content.

Before the pyrolysis temperature reaches 1100°C, the fundamental phase evolution process in the studied system can be understood by examining the mass loss. With the presence of water vapor between 500°C and 700°C, the polymer to ceramic transformation occurs with the following reactions:[15, 17]

$$Si\text{-}H + H_2O \rightarrow Si\text{-}OH + H_2\uparrow \quad (A.1)$$

$$Si\text{-}CH_3 + H_2O \rightarrow Si\text{-}OH + CH_4\uparrow \quad (A.2)$$

$$Si\text{-}CH_2\text{-}Si + H_2O \rightarrow Si\text{-}OH + Si\text{-}CH_3 \quad (A.3)$$

$$Si\text{-}CH_2\text{-}CH_2\text{-}Si + 2H_2O \rightarrow 2Si\text{-}OH + C_2H_6\uparrow \quad (A.4)$$

$$Si\text{-}CH{=}CH_2 + H_2O \rightarrow Si\text{-}OH + C_2H_4\uparrow \quad (A.5)$$

$$Si\text{-}C_6H_5 + H_2O \rightarrow Si\text{-}OH + C_6H_6\uparrow \quad (A.6)$$

Further, TEOS hydrolyzes following Eq. (A.7):

$$Si\text{-}O\text{-}C_2H_5 + H_2O \rightarrow Si\text{-}OH + C_2H_5OH \quad (A.7)$$

The Si-OH bonds can then condense to form Si-O-Si bonds:

$$Si\text{-}OH + Si\text{-}OH \rightarrow Si\text{-}O\text{-}Si + H_2O\uparrow \quad (A.8)$$

In addition, free carbon that precipitates between 500°C and 700°C may also oxidize following the reaction:[15, 18, 32]

$$C_{free} + H_2O \rightarrow H_2\uparrow + CO\uparrow \quad (A.9)$$

According to Eqs. (A.1)-(A.9), water vapor facilitates Si-O bond formation while reducing Si-C bonds and consuming free carbon. Fig. A.3(b) clearly reflects this when compared to samples pyrolyzed without water vapor injection [18]. The prominent formation of SiO_2 compared to SiC for all of the samples is due to the decrease of Si-C bonds in the water vapor environment [15].

Fig. A.3(a) shows the XRD patterns of the SiOC samples pyrolyzed in the Ar+H_2O atmosphere at 1100°C. All the samples show an amorphous SiO_2 halo centered around ~23° [29]. In addition, all the samples exhibit a peak at ~44°, which corresponds to the (100) plane of turbostratic carbon [29, 33-35]. The lack of any crystalline peaks for SiO_2 shows that the TEOS-derived SiO_2 remains amorphous rather than crystallizing. Due to the broad amorphous peak characteristic of SiOC ceramics pyrolyzed at temperatures below ~1200°C, the onset of major phase separation, the amorphous SiO_2 within the samples cannot be distinguished from the SiOC matrix and the samples show no differences in Fig. A.3(a) [6, 18, 36].

Increasing the pyrolysis temperature to 1400°C (Fig. A.3(b)) results in the samples showing more obvious SiO_2 (22°) and C peaks (44°), as well as weak SiC peaks at 35.6°, 60°, and

72°. The presence of the SiO_2, SiC, and carbon diffraction peaks for the samples pyrolyzed at 1400°C occurs due to the phase separation of SiOC, as well as the carbothermal reduction of SiO_2 into SiC. The main reactions that produce SiO_2, SiC, and C within the ceramics are given by the following reactions:[10, 37]

$$2SiOC \rightarrow SiO_2(amorphous) + SiC(\beta) + C \quad (A.10)$$

$$SiO_2(amorphous) + 3C \rightarrow SiC(\beta) + 2CO\uparrow \quad (A.11)$$

Higher TEOS contents lead to slightly more obvious phase peaks (C peak at 44° as well as weak SiC peaks at 35.6°, 60°, and 72°). Overall, there is no major peak difference.

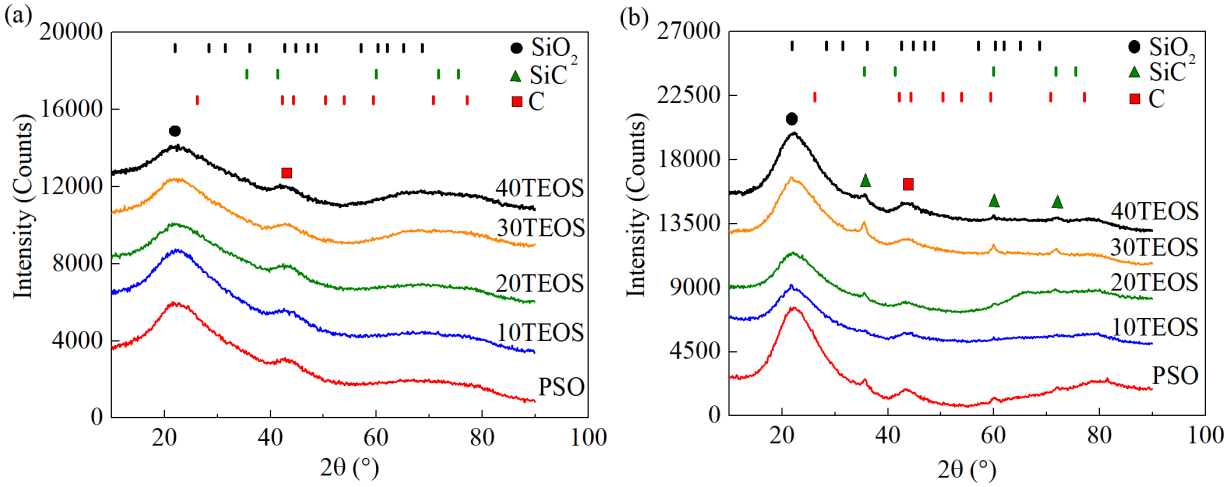

Fig. A.3 XRD patterns for different polymer precursors after pyrolysis at (a) 1100°C and (b) 1400°C.

The XRD patterns for the SiOC samples pyrolyzed at 1100°C and 1400°C after the HF etching are shown in Figs. A.4(a) and A.4(b), respectively. Dotted lines show the original positions of the amorphous hump before etching. For the 1100°C pyrolyzed samples (Fig. A.4(a)), the XRD patterns show a slightly lower halo with a right peak shift, indicating the removal of the amorphous SiO_2 phase. However, the difference between Figs. A.3(a) and A.4(a) is fairly small, again confirming that the SiO_2 phase separation is insignificant at 1100°C. In Fig. A.4(b), however, the samples no longer show the amorphous SiO_2 hump around 23°; rather, the center of the diffused peak shifts to approximately 24.5°, due to the contributions of the SiOC, residual SiO_2, and turbostratic carbon, which has a peak at approximately 26° from the (002) plane [34, 35, 38]. The SiC peaks and the C peaks all become much more visible. This means a rather large amount of

amorphous SiO_2 phase has been etched away. The etching of the SiO_2 nanodomains by the HF solution is well understood as:[18]

$$SiO_2 + 6HF \rightarrow H_2SiF_6 + 2H_2O \quad (A.12)$$

In addition, a new diffraction peak emerges after etching the 1400°C samples, at approximately 78°, which corresponds to the (110) plane of carbon [35]. The peak at 78° was too weak to accurately distinguish before etching, but becomes more visible after etching due to the removal of SiO_2, which effectively increases the relative concentration of both the remaining SiC and carbon phases and thus increases their diffraction peak intensities.

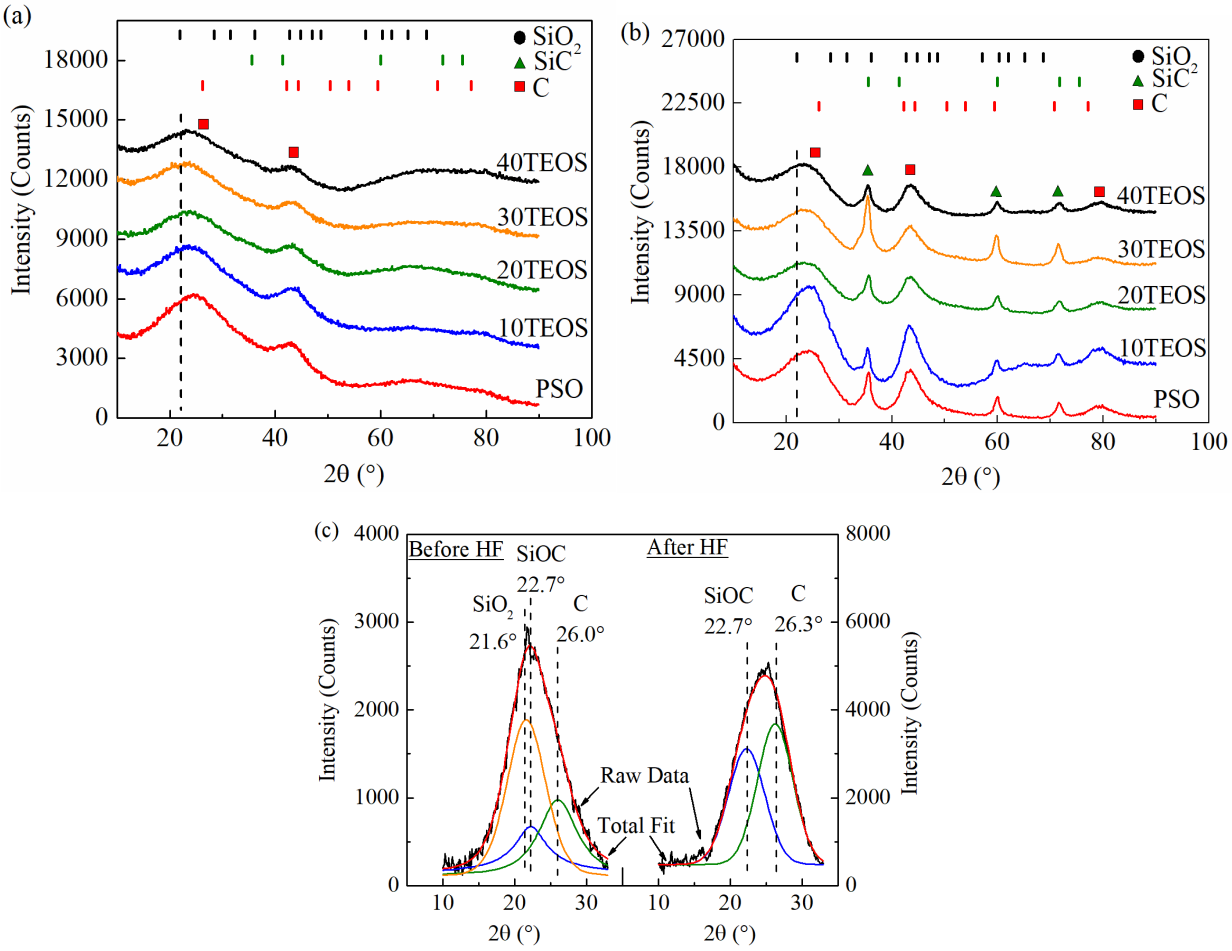

Fig. A.4 XRD patterns after HF etching of the SiOC samples pyrolyzed at (a) 1100°C and (b) 1400°C, and (c) a comparison of peak fitting before and after etching.

Fig. A.4(c) directly compares the peak splitting results from Fig. A.3(b) and Fig. A.4(b) at ~22-25°C. Before the HF etching (Fig. A.3(a)), there are three deconvoluted halos/peaks

corresponding to SiO_2 (21.6°), SiOC (22.7°), and C (26.0°). The dominance of the SiO_2 halo is obvious with the highest intensity. After the HF etching, only the SiOC halo (22.7°) and the C peak are present with the peak splitting. This comparison directly shows the removal of SiO_2 due to the HF etching.

A.4.3 Specific surface areas and pores

Nitrogen adsorption study was not conducted on the samples pyrolyzed at 1100°C due to the low mass loss from etching and thus the insignificant amount of pores from the SiO_2 removal. All the samples pyrolyzed at 1400°C have similar specific surface areas, specific pore volumes, and pore sizes (see supplement in Erb et. at[39]), meaning that the SiO_2 nanodomains have grown to similar sizes due to more extensive phase separation, which agrees with the high specific pore volume and larger pore sizes. Thus, Fig. A.4 only shows the nitrogen adsorption curves for the samples pyrolyzed at 1300°C after the HF etching. All the samples show a large adsorption volume at low relative pressures, followed by a relative constant adsorption volume at higher relative pressures; this adsorption behavior corresponds to the Type I isotherm, according to the IUPAC classification, which indicates that the samples are prominently microporous with only monolayer adsorption [40]. In detail, the PSO sample has an adsorbed gas volume of 519 cm^3/g at a relative pressure ≈ 1. The 10TEOS sample, however, has the highest adsorbed gas volume of 644 cm^3/g. When the TEOS content increases to 20, 30, and 40 wt%, the adsorbed gas volume decreases from 586 cm^3/g and then stabilizes at approximately 553 cm^3/g. This means that the phase separated SiO_2 in the SiOC has a maximum at 10 wt% TEOS; higher TEOS content is not conducive for the desired SiO_2 formation.

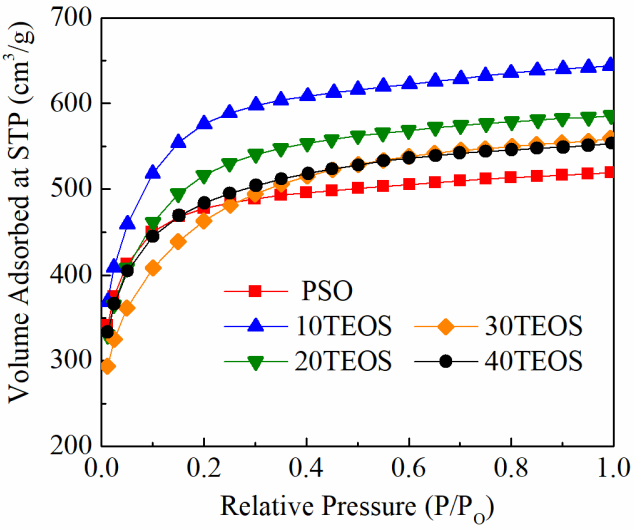

Fig. A.5 Nitrogen adsorption curves for the samples pyrolyzed at 1300°C after etching.

The specific surface area, specific pore volume, and average pore size after etching for all of the samples pyrolyzed at 1300°C are summarized in Table A.1. The addition of 10 wt% TEOS creates more surface area, with the specific surface area increasing from 1812.1 m^2/g to 2107.2 m^2/g from the pure PSO to the 10TEOS. This means that water vapor pyrolysis can facilitate the hydrolysis and condensation of TEOS into SiO_2 during the pyrolysis following Eqs. (A.7)-(A.8) and thus increase the SiO_2 content in the SiOC. With additional TEOS content, however, the specific surface area decreases to 1876.1 m^2/g for 20TEOS, 1666.9 m^2/g for 30TEOS, and 1794.9 m^2/g for 40TEOS. This means that the amount and distribution of SiO_2 nanoclusters in the SiOC also plays an important role in the specific surface area value, as to be discussed in Section A.4.4.

Table A.1 Nitrogen adsorption results for the SiOC ceramics pyrolyzed at 1300°C after the HF etching.

sample	BET-equivalent apparent specific surface area (m^2/g)	NLDFT specific surface area (m^2/g)	specific pore volume (cm^3/g)
PSO	1812.1	2091.1	0.76
10TEOS	2107.2	2200.6	0.99
20TEOS	1876.1	1962.6	0.89
30TEOS	1666.9	1745.4	0.86

40TEOS	1794.9	2024.1	0.85

The specific pore volume follows the same general trend as the specific surface area, with the specific pore volume initially increasing from 0.764 m^3/g for PSO to 0.99 cm^3/g for 10TEOS. Further increase in the TEOS content from 20-40 wt% has little effect on the specific pore volume, instead it decreases from 0.89 cm^3/g for 20TEOS to 0.85 cm^3/g for 40TEOS.

The pore size distributions obtained from the NLDFT fitting for the samples pyrolyzed at 1300°C are shown in Fig. A.5. For the PSO sample, the pore size distribution shows a peak at ~1.6 nm and then some broad distribution at larger pore sizes. With the addition of 10 wt% TEOS, the pore size distribution has a wider and higher peak at 1.6-1.8 nm. In addition, a small peak at 3.5 nm emerges, and the pore size distribution becomes wider with a higher volume of pores between 2-4 nm. With an increase to 20TEOS, the peaks at 1.6 nm and 1.8 nm shrink and the peak at 3.5 nm slightly grows. Increasing the TEOS content for the 30TEOS sample causes further decrease in the volume of small pores and pronounced increase in pores around 3.5 nm. Interestingly, the 40TEOS sample shows a similar pore size distribution as PSO, with only one peak at 1.6 nm and a much smaller peak at 3.5 nm. It should also be noticed that the 10TEOS sample has the highest peak height at 1.6-1.8 nm pore sizes. The other composition samples all have lower peak height, especially for higher TEOS samples. This means that the higher TEOS samples may contain fewer pores. Overall, for the 10TEOS sample, the specific pore volume is highest, and the pore size is rather small. Correspondingly, the specific surface area is highest.

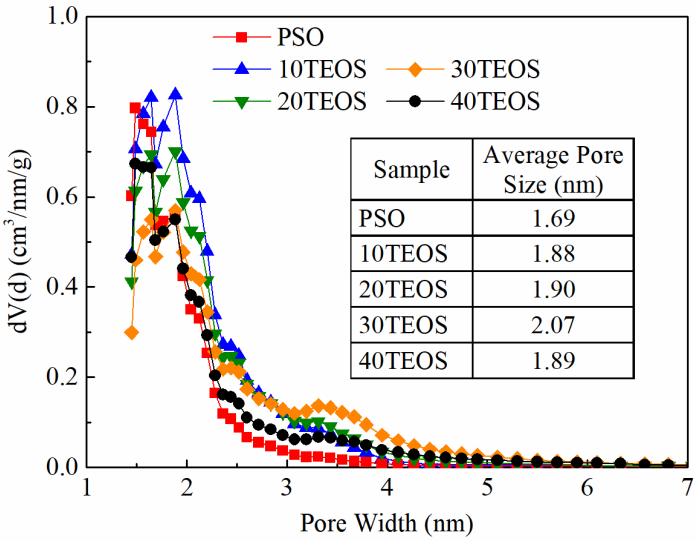

Sample	Average Pore Size (nm)
PSO	1.69
10TEOS	1.88
20TEOS	1.90
30TEOS	2.07
40TEOS	1.89

Fig. A.6 Pore size distributions for the samples pyrolyzed at 1300°C.

A.4.4 SiOC microstructure understanding

Considering the ceramic yields, XRD patterns, and nitrogen adsorption results, the effect of TEOS-derived SiO_2 on the formation of SiO_2 within SiOC can be understood as follows. During the pyrolysis, for the pure PSO, polymer decomposition and SiOC phase separation lead to SiO_2 nanocluster formation, as shown in Fig. A.7(a). For the TEOS-containing PSO, the SiO_2 domains in the SiOC matrix during pyrolysis come from two sources: the SiOC matrix and the TEOS hydrolysis. Initially, when TEOS is added into PSO, it disperses. At low TEOS content (Fig. A.7(b)), even though some TEOS clusters might be present, they are rather small due to the similar nature of hydrophobicity. When the SiO_2 nanoclusters derived from the aggregated TEOS clusters are small enough to be comparable with the PSO phase separation induced SiO_2 nanoclusters, these SiO_2 domains co-exist with limited merging, and thus generate very larger surface areas. Such a sample would contain more small and independent pores (Fig. A.7(b)), consistent with Fig. A.6. This is the case for the 10 wt% TEOS sample, the TEOS-derived SiO_2 is relatively independent of the SiO_2 which initially forms from the phase separation of SiOC. The system has a specific pore volume of 0.99 cm^3/g, much greater than that of the PSO (0.76 cm^3/g). However, as the TEOS content increases (Fig. A.7(c)), TEOS molecule aggregation increases. When the TEOS content is high, the resultant SiO_2 clusters are either large to start with due to the TEOS aggregation, or small SiO_2 nanodomains are so close that they merge and grow into larger sizes, either among themselves

or with the PSO derived SiO_2 clusters. As a result, the pore sizes increase and the specific surface area decreases. In this work, at >10 wt% content of TEOS, the results in Figs. A.5 and A.6 show that the TEOS-derived SiO_2 nanodomains can no longer remain sufficiently separate; instead, they merge with other SiO_2 domains derived from either the TEOS or the SiOC matrix, creating more pores between 3 - 4 nm without forming more pores at ~1.6 nm. The merging of the SiO_2 domains can be considered analogous to phase separation of the SiOC matrix; the ceramic yield and the etching results confirm this hypothesis. The higher TEOS content samples contain increasing content of SiC (Fig. A.3(b) and Fig. A.4(b)), which must have occurred through phase separation of the SiOC matrix (Eq. (A.10)) because the carbothermal reduction of SiO_2 into SiC (Eq. (A.11)) would have caused a significant decrease in the ceramic yield between 1100°C and 1400°C, a lower etching mass loss, and smaller specific pore volume, none of which were observed. Thus, it can be concluded that the initial SiO_2 nuclei size is roughly 1.6 nm, and the SiO_2 size after phase separation and further growth is approximately 3.5 nm. This growth of the SiO_2 phase after phase separation is supported by the nitrogen adsorption results for all of the samples pyrolyzed at 1400°C, in which all samples show a decrease in the amount of pores of < 2 nm in favor of a larger amount of pores at ~3.5 nm in size. In addition, due to the drop in carbon within the SiOC, the SiO_2 clusters are more prone to evaporation into SiO gas, further decreasing the utility of the TEOS-derived SiO_2. A qualitative illustration of the TEOS effect on the SiO_2 nanocluster formation in SiOC is shown in Fig. A.7.

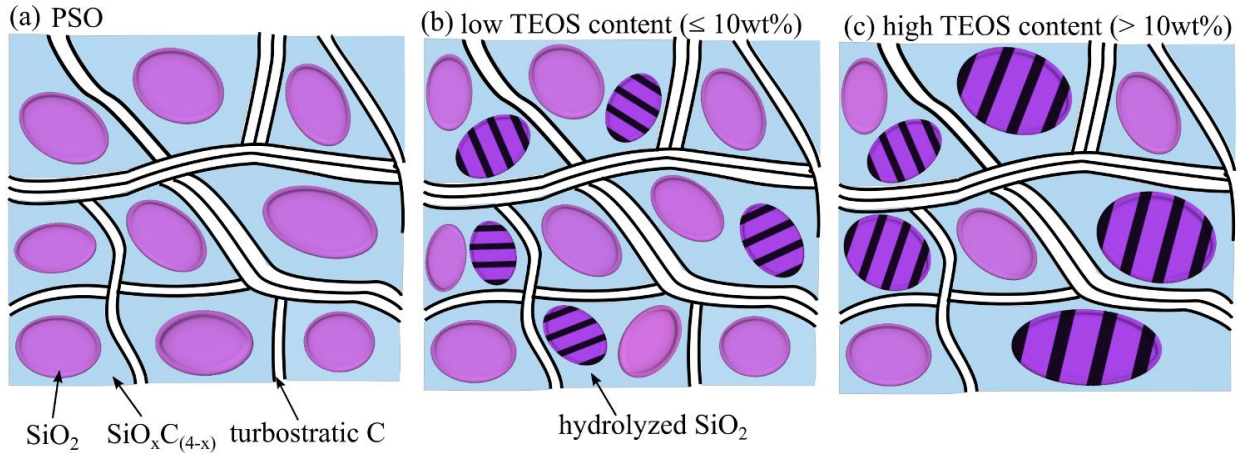

Fig. A.7 Illustration of the TEOS effect on the SiO_2 nanocluster formation in SiOC.

A more thorough three dimensional understanding of the SiOC microstructure after the HF etching was computed according to a Voronoi model, with the SiO_2 nanodomains (or pores after etching) as spheres within the center of each Voronoi cell. The size distribution of the spheres within the Voronoi cells was based on the nitrogen adsorption experimental results, and a comparison between the generated values for the pore diameters and the experimental data is shown for each of the samples in the supplement of Erb et. al [39].

In this work, 50 Voronoi cells with the superimposed pores are created within a cube with a side length l, defined in order to match with the specific pore volume of the samples:

$$l = \left(\frac{50\pi\, d^3}{6\, V_p\, \rho_b} \right)^{1/3} \tag{A.13}$$

where d is the average pore diameter in nm, as listed in Fig. A.6, V_p is the specific pore volume, in cm^3/g, as listed in Table A.1, and ρ_b is the measured bulk density of the samples after etching in g/cm^3. They are 0.61, 0.58, 0.58, 0.57, and 0.60 g/cm^3 from the pure PSO sample to the 40TEOS sample.

The 3D images of the etched PSO, 10TEOS, and 30TEOS samples obtained from the Voronoi model are shown in Fig. A.8. The PSO samples have more connected pores, the 10TEOS sample has a large number of independent pores, and the 30TEOS sample has a higher number of connected pores, matching the earlier hypotheses based on the experimental results. Suitable amount of TEOS addition creates more small and separated SiO_2 nanoclusters of similar size to that of the PSO phase separated SiO_2 nanoclusters.

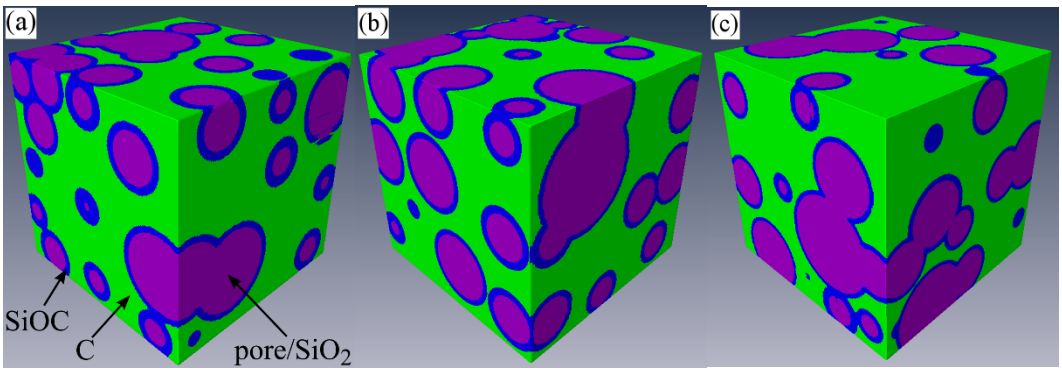

Fig. A.8 Simulated SiOC after the HF etching for the (a) PSO, (b) 10TEOS, and (c) 30TEOS samples pyrolyzed at 1300°C. The purple color represents pores (the original SiO_2 nanoclusters), the blue color represents SiOC, and the green color represents C.

From the 3D structures in Fig. A.8, the surface area S_{sim} with units of nm^2 is converted to specific surface area SSA_{sim} with a unit of m^2/g, using:

$$SSA_{sim} = \frac{1000\ S_{sim}}{\rho_b V_{sim}} \tag{A.14}$$

where V_{sim} is the total volume of the 3D structure of the sample in nm^3. Likewise, the porosity from the 3D reconstruction P_{sim} is used to calculate the specific pore volume $V_{p,sim}$ with a unit of cm^3/g according to:

$$V_{p,sim} = \frac{P_{sim}}{\rho_b} \tag{A.15}$$

The results for the specific surface area and specific pore volume of the simulated samples are compared to the experimental results in Figs. A.9(a) and (b), respectively. For the specific surface area, the simulated models for all of the samples give slightly higher values than those obtained experimentally, although all of the samples except for the PSO show only a minor shift from the expected values, demonstrating that the model is consistent for all of the samples. The poorer correlation for the PSO samples is likely due to the less than desired left branch of the pore size distribution curve, which causes deviation during the curve fitting and discretization of different sizes of pores. Likewise, the specific pore volumes from the model are consistently yet only slightly higher than their experimental values. The higher values from the simulation than those from the experiments are believed to be due to the inaccessibility of the small as well as closed pores during the BET measurements, which effectively lowers the measured specific surface area and pore volume values. The results in Figs. A.9(a) and (b) demonstrate that

representation of the SiOC matrix using a Voronoi spatial distribution gives reasonable results, allowing the visualization of the distribution of SiO_2 domains within the SiOC matrix.

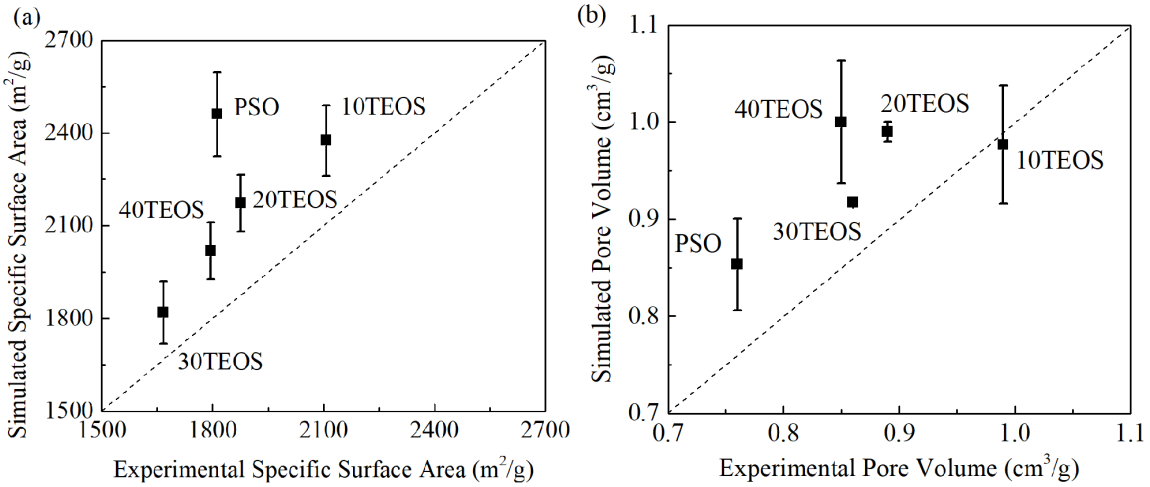

Fig. A.9 Comparison between the experimental and simulated (a) specific surface areas and (b) specific pore volumes. The dashed line indicates what a perfect agreement should be between the simulations and experiments (with a slope of 1).

To estimate the theoretical specific surface area of the SiOC matrix after etching, a simple spherical core-shell hexagonal packing model can be created as shown in the insert of Fig. A.10, in which one spherical SiO_2 domain is surrounded by different numbers of layers of turbostratic carbon. As seen, the number of graphene sheets wrapping around the pores has a tremendous effect on the specific surface area. When there is one turbostratic carbon layer separating the SiO_2 domains, the specific surface area ranges from 1780 to 2332 m^2/g for SiO_2 sizes from 1 nm to 5 nm, respectively. However, when the number of separating turbostratic carbon layers is increased to two, the specific surface area changes from 770 to 819 m^2/g, a substantial decrease. Likewise, when the turbostratic carbon layers are increased to three, four, and five, the specific surface areas are ~450, 280, and 200 m^2/g, respectively, showing continuous and significant decreases. It should also be noticed that the diameter of the pores, from 1 nm to 5 nm, also has an observable effect on the specific surface area when there is one carbon layer, with larger size pores causing a continuous increase of the specific surface area. When the number of the carbon layers is two or higher, the pore size effect on the specific surface area is negligible. It should be clarified that this observation only applies to single size pores, not to be confused with the pores with different size distributions

shown in Fig. A.6. Overall, a thin carbon layer around the pores is essential to achieving high specific surface areas.

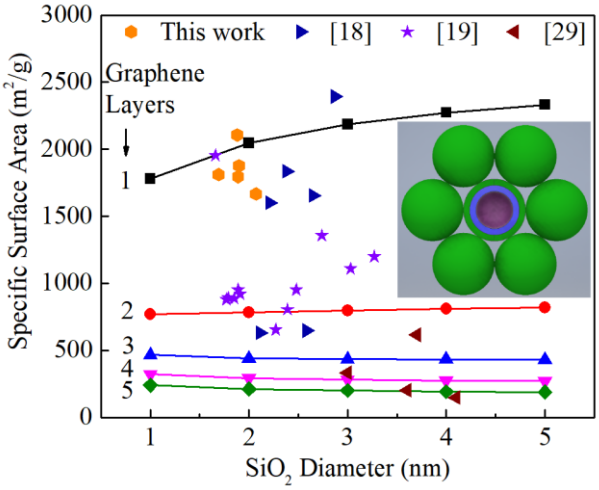

Fig. A.10 Specific surface area calculation assuming one pore is surrounded by different layers of turbostratic carbon and the hollow shell units pack regularly. The experimental data from this work and other studies are also indicated by different markers.

For our studied system, the specific surface area ranges from 1667 to 2107.2 m^2/g, very close to and understandably slightly lower than these theorized values, as shown in Fig. A.10. The specific surface areas obtained from our earlier work and other groups are also indicated on Fig. A.10 by different symbols. It proves that very thin layers of turbostratic carbon and SiO_2 nanoclusters are intimately intergrown during the pyrolysis.

For the pore volumes, using the spherical packing model with 2 layers of graphitic carbon and 1.88 nm pore size (for the 10TEOS sample), the projected specific pore volume is still much higher at 2.24 cm^3/g. Other samples have similar specific pore volumes because of the similar pore sizes in. A.6. The difference between the idealized model and the actual samples can be related to many factors such as pore shape, accessibility of the pores, the composition and thus the density of the matrix, etc.

Nonetheless, based on this theoretical idealization, the challenge in creating high specific surface area materials is creating small size and uniform pores with a thin shell and keeping them from merging, which would require great processing condition control.

A.5 Conclusions

The in-situ conversion of TEOS into SiO_2 and its incorporation within SiOC ceramics is investigated by crosslinking TEOS within a polysiloxane matrix and introducing water vapor during pyrolysis. The effect of the TEOS-derived SiO_2 on the phase development within the SiOC is studied. With the optimal TEOS addition (10 wt%) within the crosslinked polymer, SiO_2 forms from the hydrolysis and condensation of the TEOS with the water vapor atmosphere, independently of the SiO_2 formed from the phase separation of the SiOC matrix. These independent SiO_2 nuclei can be etched away, creating a higher number of ~2 nm size pores, an increase in the specific surface area (up to ~2100 m^2/g), and higher specific pore volume (~1 cm^3/g). The fundamental microstructural evolution is further studied using Voronoi cell modeling and theoretical calculation. Consistent results with the experiments are demonstrated.

References

1. Colombo P, Mera G, Riedel R, Soraru GD. Polymer-derived ceramics: 40 years of research and innovation in advanced ceramics. *J Am Ceram Soc* **2010**, *93*, 1805-1837.
2. Lu K, Erb D, Liu M. Thermal stability and electrical conductivity of carbon-enriched silicon oxycarbide. *J Mater Chem C* **2016**, *4*, 1829-1837.
3. Lu K, Erb D, Liu MY. Phase transformation, oxidation stability, and electrical conductivity of TiO_2-polysiloxane derived ceramics. *J Mater Sci* **2016**, *51*, 10166-10177.
4. Blum Y, Soraru GD, Ramaswamy AP, Hui D, Carturan SM. Controlled mesoporosity in SiOC via chemically bonded polymeric "spacers". *J Am Ceram Soc* **2013**, *96*, 2785-2792.
5. Colombo P. Engineering porosity in polymer-derived ceramics. *J Eur Ceram Soc* **2008**, *28*, 1389-1395.
6. Li JK, Lu K, Lin TS, Shen FY. Preparation of micro-/mesoporous SiOC bulk ceramics. *J Am Ceram Soc* **2015**, *98*, 1753-1761.
7. Lu K. Porous and high surface area silicon oxycarbide-based materials-a review. *Mater Sci Eng, R* **2015**, *97*, 23-49.

8. Wan JL, Gasch MJ, Mukherjee AK. In situ densification behavior in the pyrolysis consolidation of amorphous Si-N-C bulk ceramics from polymer precursors. *J Am Ceram Soc* **2001**, *84*, 2165-2169.
9. Brequel H, Parmentier J, Soraru GD, Schiffini L, Enzo S. Study of the phase separation in amorphous silicon oxycarbide glasses under heat treatment. *Nanostruct Mater* **1999**, *11*, 721-731.
10. Saha A, Raj R. Crystallization maps for SiCO amorphous ceramics. *J Am Ceram Soc* **2007**, *90*, 578-583.
11. Biasetto L, Pena-Alonso R, Soraru GD, Colombo P. Etching of SiOC ceramic foams. *Adv Appl Ceram* **2008**, *107*, 106-110.
12. Saha A, Raj R, Williamson DL. A model for the nanodomains in polymer-derived SiCO. *J Am Ceram Soc* **2006**, *89*, 2188-2195.
13. Dibandjo P, Dire S, Babonneau F, Soraru GD. New insights into the nanostructure of high-C SiOC glasses obtained via polymer pyrolysis. *Glass Technol: Eur J Glass Sci Technol, Part A* **2008**, *49*, 175-178.
14. Dibandjo P, Dire S, Babonneau F, Soraru GD. Influence of the polymer architecture on the high temperature behavior of SiCO glasses: A comparison between linear- and cyclic-derived precursors. *J Non-Cryst Solids* **2010**, *356*, 132-140.
15. Liang T, Li Y-L, Su D, Du H-B. Silicon oxycarbide ceramics with reduced carbon by pyrolysis of polysiloxanes in water vapor. *J Eur Ceram Soc* **2010**, *30*, 2677-2682.
16. Narisawa M, Terauds K, Raj R, Kawamoto Y, Matsui T, Iwase A. Oxidation process of white Si-O-C(-H) ceramics with various hydrogen contents. *Scripta Mater* **2013**, *69*, 602-605.
17. Lu K, Li J. Fundamental understanding of water vapor effect on SiOC evolution during pyrolysis. *J Eur Ceram Soc* **2016**, *36*, 411-422.
18. Li JK, Lu K. Highly porous SiOC bulk ceramics with water vapor assisted pyrolysis. *J Am Ceram Soc* **2015**, *98*, 2357-2365.
19. Erb D, Lu K. Additive and pyrolysis atmosphere effects on polysiloxane-derived porous SiOC ceramics. *J Eur Ceram Soc* **2017**, *37*, 4547-4557.
20. Juttke Y, Richter H, Voigt I, Prasad RM, Bazarjani MS, Gurlo A, Riedel R. Polymer derived ceramic membranes for gas separation. *Chem Eng Trans* **2013**, *32*, 1891-1896.

21. Dibandjo P, Graczyk-Zajac M, Riedel R, Pradeep VS, Soraru GD. Lithium insertion into dense and porous carbon-rich polymer-derived SiOC ceramics. *J Eur Ceram Soc* **2012**, *32*, 2495-2503.
22. Pradeep VS, Ayana DG, Graczyk-Zajac M, Soraru GD, Riedel R. High rate capability of SiOC ceramic aerogels with tailored porosity as anode materials for Li-ion batteries. *Electrochim Acta* **2015**, *157*, 41-45.
23. Janakiraman N, Aldinger F. Fabrication and characterization of fully dense Si-C-N ceramics from a poly (ureamethylvinyl) silazane precursor. *J Eur Ceram Soc* **2009**, *29*, 163-173.
24. Martinez-Crespiera S, Ionescu E, Kleebe HJ, Riedel R. Pressureless synthesis of fully dense and crack-free SiOC bulk ceramics via photo-crosslinking and pyrolysis of a polysiloxane. *J Eur Ceram Soc* **2011**, *31*, 913-919.
25. Schneider CA, Rasband WS, Eliceiri KW. NIH image to ImageJ: 25 years of image analysis. *Nat Methods* **2012**, *9*, 671-675.
26. ASTM C20-00, Standard test methods for apparent porosity, water absorption, apparent specific gravity, and bulk density of burned refractory brick and shapes by boiling water, ASTM International, West Conshohocken, PA, 2015.
27. Rouquerol J, Llewellyn P, Rouquerol F. Is the BET equation applicable to microporous adsorbents? *Stud Surf Sci Catal* **2006**, *160*, 49-56.
28. Ravikovitch PI, Neimark AV. Characterization of nanoporous materials from adsorption and desorption isotherms. *Colloids Surf, A* **2001**, *187*, 11-21.
29. Peña-Alonso R, Sorarù GD, Raj R. Preparation of ultrathin-walled carbon-based nanoporous structures by etching pseudo-amorphous silicon oxycarbide ceramics. *J Am Ceram Soc* **2006**, *89*, 2473-2480.
30. Halim M, Hudaya C, Kim AY, Lee JK. Phenyl-rich silicone oil as a precursor for SiOC anode materials for long-cycle and high-rate lithium ion batteries. *J Mater Chem A* **2016**, *4*, 2651-2656.
31. Tejedor-Tejedor MI, Paredes L, Anderson MA. Evaluation of ATR-FTIR spectroscopy as an "in situ" tool for following the hydrolysis and condensation of alkoxysilanes under rich H_2O conditions. *Chem Mater* **1998**, *10*, 3410-3421.

32. Tobias G, Shao LD, Salzmann CG, Huh Y, Green MLH. Purification and opening of carbon nanotubes using steam. *J Phys Chem B* **2006**, *110*, 22318-22322.
33. Wilson AM, Zank G, Eguchi K, Xing W, Yates B, Dahn JR. Pore creation in silicon oxycarbides by rinsing in dilute hydrofluoric acid. *Chem Mater* **1997**, *9*, 2139-2144.
34. Pena-Alonso R, Mariotto G, Gervais C, Babonneau F, Soraru GD. New insights on the high-temperature nanostructure evolution of SiOC and B-doped SiBOC polymer-derived glasses. *Chem Mater* **2007**, *19*, 5694-5702.
35. Li ZQ, Lu CJ, Xia ZP, Zhou Y, Luo Z. X-ray diffraction patterns of graphite and turbostratic carbon. *Carbon* **2007**, *45*, 1686-1695.
36. Rouxel T, Massouras G, Soraru GD. High temperature behavior of a gel-derived SiOC glass: Elasticity and viscosity. *J Sol-Gel Sci Technol* **1999**, *14*, 87-94.
37. Kleebe HJ, Turquat C, Soraru GD. Phase separation in an SiCO class studied by transmission electron microscopy and electron energy-loss spectroscopy. *J Am Ceram Soc* **2001**, *84*, 1073-1080.
38. Soraru GD, Pena-Alonso R, Leoni M. C-rich micro/mesoporous Si(B)OC: In situ diffraction analysis of the HF etching process. *Micropor Mesopor Mater* **2013**, *172*, 125-130.
39. Erb D, Lu K. Effects of SiO_2-forming additive on polysiloxane derived SiOC ceramics. *Microporous Mesoporous Mater* **2018**, *266*, 75-82.
40. Sing KSW. Reporting physisorption data for gas solid systems - with special reference to the determination of surface-area and porosity. *Pure Appl Chem* **1982**, *54*, 2201-2218.

Appendix B: Synthesis of SiOC using Solvent-Modified Polymer Precursors

B.1 Abstract

Silicon oxycarbide ceramics are an important class of materials that can be modified to cover a wide range of microstructures and compositions during processing. This study focuses on a polysiloxane precursor to SiOC conversion when crosslinked in the presence of 0, 50, 100, and 200 vol% of 3-pentanone, n-heptane, or isobutylbenzene, relative to the volume of the polysiloxane. The solvent modified samples show a decrease in bulk density and an increase in open porosity. The addition of the solvents facilitates the formation of crystalline SiC, especially for 3-pentanone. The ability of the solvents to encourage SiC formation is directly related to the solvent molecular size, with smaller solvents being more likely to remain trapped within the polymer after drying and subsequently creating more C-C and Si-C bonds after pyrolysis. This work shows the unique function of solvents in modifying the SiOC microstructures and properties.

B.2 Introduction

Silicon oxycarbide (SiOC) is an amorphous ceramic, consisting of SiO_xC_{4-x} bonds, where $0<x<4$, and free carbon when pyrolyzed at temperatures lower than ~1250°C. At >1300°C pyrolysis temperatures, an amorphous/nanocrystalline composite forms. Due to SiOC being a polymer derived ceramic, its properties and compositions are highly configurable simply by controlling the chemistry of the preceramic polymer(s) and the processing conditions. SiOC has a wide range of tailorable properties, such as porosity, high temperature stability, oxidation resistance, and electrical conductivity [1-3]. Porous SiOC has gained much attention for applications such as electrodes in lithium ion batteries, catalyst supports, gas separation membranes, lightweight components, and thermal barriers [4-6]. Likewise, dense SiOC is promising in applications such as coatings and structural components due to its resistance to oxidation/crystallization at elevated temperatures and excellent mechanical properties [1, 7, 8].

Solvents have been widely used during gelation in the fabrication of silica gels [9]. After gelation, the solvent is removed either by supercritical drying, most often using supercritical CO_2, or through subcritical drying, such as drying at ambient temperature and pressure [6, 9-12]. For

polymer derived ceramics, porosity can be introduced through the use of a solvent during crosslinking followed by removal of the solvent by drying. The selection of the solvent and solvent concentration has significant effects on the drying behavior, pore size, and pore morphology of both the polymer and the SiOC after pyrolysis [12-15]. Sasikumar et. al.[12] crosslinked polyhydromethylsiloxane and divinylbenzene in the presence of either acetone or cyclohexane as a solvent, followed by CO_2 supercritical drying. After pyrolysis in argon, the sample crosslinked in acetone had a specific surface area of 215 m^2/g and a pore volume of 0.87 m^3/g, while the sample crosslinked in cyclohexane had a specific surface area of 108 m^2/g and a pore volume of 0.20 m^3/g. Further, the pore size of the acetone sample was between 20-30 nm, while the pore size of the cyclohexane sample was much smaller, around 4 nm. It should also be pointed out that the porosity introduced during crosslinking or the early stages of pyrolysis is transient and usually disappears at temperatures greater than 600-800°C [16, 17].

Although the use of various solvents to alter the polymer pore structure before pyrolysis has been investigated, the effect of solvents on the pyrolysis behavior, structural evolution, and microstructure of SiOC has not been carefully studied. Tamayo et al.[13] investigated the effect of aging polydimethylsiloxane (PDMS) and tetraethyl orthosilicate (TEOS) hybrid gels in acetone, isopropanol, and n-hexane on the properties of the obtained SiOC after pyrolysis. It was claimed that polar solvents, such as acetone and isopropanol, more easily remove non-bonded PDMS molecules from the gel [13, 15]. With increasing aging time, the polar solvents decreased the carbon crystallite sizes within the SiOC after pyrolysis at 1100°C while the non-polar solvent showed the opposite trend [13]. For the SiOC synthesized using polyhydromethylsiloxane and divinylbenzene and crosslinked in the presence of either acetone or cyclohexane. The sample crosslinked in acetone had a slightly smaller carbon domain size compared to the non-polar cyclohexane after pyrolysis at 900°C [12]. Since the properties of SiOC, such as its stability in air, are heavily dependent on its chemical and phase compositions, further understanding of the solvent effects is needed.

In this work, SiOC ceramics are fabricated after pyrolysis of a polysiloxane crosslinked in the presence of three different solvents: 3-pentanone, n-heptane, or isobutylbenzene. The effects of different solvents and the amount of solvents on the resulting pyrolysis behavior, phase evolution, and microstructure of the SiOC ceramics are studied.

B.3 Experimental Procedures

A commercial polysiloxane (PSO, $[-Si(C_6H_5)_2O-]_3[-Si(CH_3)(H)O-]_2[-Si(CH_3)(CH=CH_2)O-]_2$, SPR-684, Starfire Systems, Inc., Gelest Inc., Schenectady, NY) was chosen as the base precursor and 2.1-2.4% platinum-divinyltetramethyldisiloxane complex in xylene (Pt catalyst, Gelest Inc., Morrisville, PA) was used as the catalyst. The three solvents used were 3-pentanone (Fisher Scientific, Pittsburgh, PA), n-heptane (Fisher Scientific, Pittsburgh, PA), and isobutylbenzene (Fisher Scientific, Pittsburgh, PA). The chemical structures of the three solvents are shown in Fig. B.1.

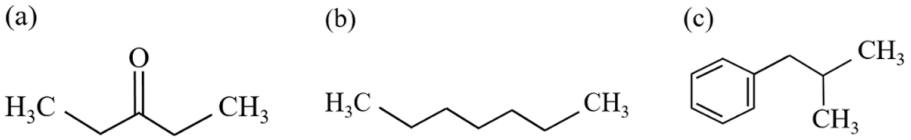

Fig. B.1 Molecular structures of (a) 3-pentanone, (b) n-heptane, and (c) isobutylbenzene.

First, solutions with PSO and either 0, 50, 100, or 200 vol% solvent (relative to the PSO volume) were sonicated for 10 minutes and then mixed in a high energy mill (SPEX 8000M Mixer/Mill, SPEX SamplePrep, Metuchen, NJ) for 10 minutes to form a homogeneous mixture. Next, the Pt catalyst (1 wt% relative to PSO) was added, the mixtures were mixed again in a high energy ball mill for 5 minutes, and then poured into aluminum foil molds. The mixtures were placed into a vacuum chamber and vacuumed for 10 minutes at 200 Torr to remove any bubbles in the solutions. The molds were then sealed in acid digestion vessels to prevent evaporation of the solvents and placed in an oven to crosslink at 50°C for 12 hrs and then at 120°C for 6 hrs. After crosslinking, the molds were removed from the acid digestion vessels and dried at room temperature for 24 hrs, 50°C for 12 hrs, and 120°C for 6 hrs to remove all the solvent. The samples designated as PSO corresponded to the pure PSO composition; the samples with solvent additions were labelled as X-p, X-h, and X-i, where h, p, and i correspond to 3-pentanone, n-heptane, and isobutylbenzene, respectively, and X was the volume percent of solvent (50, 100, or 200).

To prepare the samples for pyrolysis, the crosslinked specimen were cut and polished into square pieces roughly 10 mm in length and 2 mm in thickness. Next, the samples were placed into a zirconia crucible, covered on both sides with graphite mats in order to reduce friction during shrinkage and prevent warping [18, 19], and put into a tube furnace (1730-20 Horizontal Tube

Furnace, CM Furnaces Inc., Bloomfield, NJ). With an Ar flow rate of about 500 std cm^3/min, the samples were heated up to 1300°C at a rate of 1°C/min, held for 2 h, cooled to 400°C with a rate of 1°C/min, and finally cooled to 50°C with a rate of 2°C/min. During heating from 500°C-700°C, the Ar gas flow was bubbled through water at 60°C, giving a gas flow with a Ar:H_2O molar ratio of approximately 5:1; the water vapor injection encourages SiO_2 formation within the SiOC, but was not the focus of this study [20, 21].

The chemical bonding of the polymers was evaluated using Fourier Transform Infrared Spectroscopy (FT-IR) (Nicolet 8700 with Pike GladiATR attachment, Thermo Scientific, Waltham, MA), which recorded light absorbance between 500-4000 cm^{-1} wavenumber with a resolution of 4 cm^{-1} and averaged between 64 scans. The decomposition behavior of the polymer samples was measured using thermogravimetric analysis (TGA) (Q50, TA Instruments, New Castle, DE) with a heating rate of 2°C/min and an argon flow of 40 mL/min. Ceramic yield was calculated by measuring the mass of the samples before and after the pyrolysis. The bulk density and porosity of the resulting SiOCs were measured using the Archimedes method with ethanol as the saturating and submersion medium. The specific surface area and pore volume of micro-/meso-pores within the bulk samples after pyrolysis was measured using nitrogen adsorption at 77 K (NOVA 2200e, Quantachrome Instruments, Boynton Beach, FL). The phase compositions of the pyrolyzed samples were analyzed in an X'Pert PRO diffractometer (PANalytical B.V., EA Almelo, the Netherlands) with Cu Kα radiation. A field emission SEM (LEO 1550, Carl Zeiss MicroImaging, Inc, Thornwood, NY) was used to characterize the microstructures of the pyrolyzed samples.

B.4 Results and Discussion

B.4.1 Pyrolysis Behavior

The ceramic yield values for the pyrolyzed samples are shown in Table B.1. For all the pyrolyzed samples, the ceramic yields range from 67% - 72%. The addition of the solvents makes insignificant difference. In general, the ceramic yield increases slightly with the solvent content.

Table B.1 Ceramic yield, open porosity, and bulk density of the SiOC samples after pyrolysis at 1300°C.

Sample	Ceramic Yield (%)	Open Porosity (%)	Bulk Density (g/cm^3)
PSO	69.38 ± 1.12	6.0 ± 2.3	1.76 ± 0.01
50-p	69.31 ± 0.64	9.5 ± 4.1	1.61 ± 0.01
100-p	69.05 ± 0.49	6.5 ± 2.0	1.67 ± 0.07
200-p	70.25 ± 0.62	4.4 ± 0.5	1.69 ± 0.06
50-h	70.25 ± 1.55	7.9 ± 2.4	1.72 ± 0.02
100-h	70.29 ± 1.04	11.2 ± 2.6	1.65 ± 0.02
200-h	72.35 ± 0.85	14.3 ± 1.6	1.53 ± 0.02
50-i	67.16 ± 0.50	8.8 ± 5.0	1.70 ± 0.07
100-i	69.62 ± 0.39	8.7 ± 1.1	1.54 ± 0.07
200-i	69.63 ± 0.38	7.9 ± 1.5	1.71 ± 0.01

The open porosity of the SiOC samples after pyrolysis at 1300°C ranges from 4.4 vol% – 14.3 vol%. The addition of the solvents increases the open porosity of the SiOC samples relative to the pure PSO sample. For 3-pentanone, the porosity decreases from 9.5 vol% for the 50-p sample to 4.4 vol% for the 200-p sample. For the n-heptane samples, the open porosity increases from 7.9 vol% for the 50-h sample to 14.3 vol% for the 200-h sample. The porosity for the isobutylbenzene samples decreases from 8.8 vol% for the 50-i sample to 7.9 vol% for the 200-i sample. The faster drying of the polymer in this study may have contributed to the lack of a significant amount of porosity compared to those in literature. For example, Aravind et al. [22] sealed the gel using aluminum foil and let it sit for two weeks before making a hole in the aluminum foil seal and further drying for one week at 50°C. Further, there was a lack of micro- and mesoporosity within the samples as measured by nitrogen adsorption (0.001 cm^3/g for 200-p, 0.003 cm^3/g for 200-h, and 0.0007 cm^3/g for 200-i) due to the pore collapse during the aggressive drying.

The bulk density of the samples after pyrolysis ranges from 1.53 g/cm^3 – 1.76 g/cm^3. For all conditions, the addition of the solvents decreases the bulk density of the SiOC samples relative to the pure PSO sample. However, the bulk density trends are somewhat convoluted due to the

inaccessible micropores to the saturating ethanol during testing as discussed earlier, closed porosity, and the differing amounts of SiC in the samples (Section B.4.2). For the n-heptane samples, the density decreases from 1.72 g/cm^3 for the 50-h sample to 1.53 g/cm^3 for the 200-h sample. For the 3-pentanone samples, the density slightly increases from 1.61 g/cm^3 for the 50-p sample to 1.69 g/cm^3 for the 200-p sample. However, the density of the isobutylbenzene samples show no trend and varies between 1.70 g/cm^3 for the 50-i sample, 1.54 g/cm^3 for the 100-i sample, and 1.71 g/cm^3 for the 200-i sample.

B.4.2 Structural Evolution

The FT-IR spectra of the crosslinked polymers with the solvents after drying are compared to that of the PSO sample to determine whether the solvent presence during crosslinking affects the chemical bonding or crosslinking behavior of the polymer. Fig. B.2(a) shows the FT-IR spectra of the pure PSO sample and the 200 vol% condition for each of the three solvents. All the samples show sharp peaks at ~695, 715, 740, and 1130 cm^{-1} wavenumber, which are characteristic of the phenyl side group in the base PSO. The peaks at 1260 and 1426 cm^{-1} wavenumber correspond to the methyl side group, and a broad peak between 1000 and 1100 cm^{-1} wavenumber can be assigned to Si-O-Si [24]. The samples crosslinked with the different solvents show no major differences in their FT-IR spectra, which is to be expected since the solvents should not participate in the crosslinking. Fig. B.2(b) shows the FT-IR spectra for the PSO polymer and the 50, 100, and 200 vol% 3-pentanone polymers. Similar to Fig. B.2(a), there are no significant changes compared to the PSO sample when increasing the solvent content, signifying again that there is no detectable influence from the solvent on the polymer bonding.

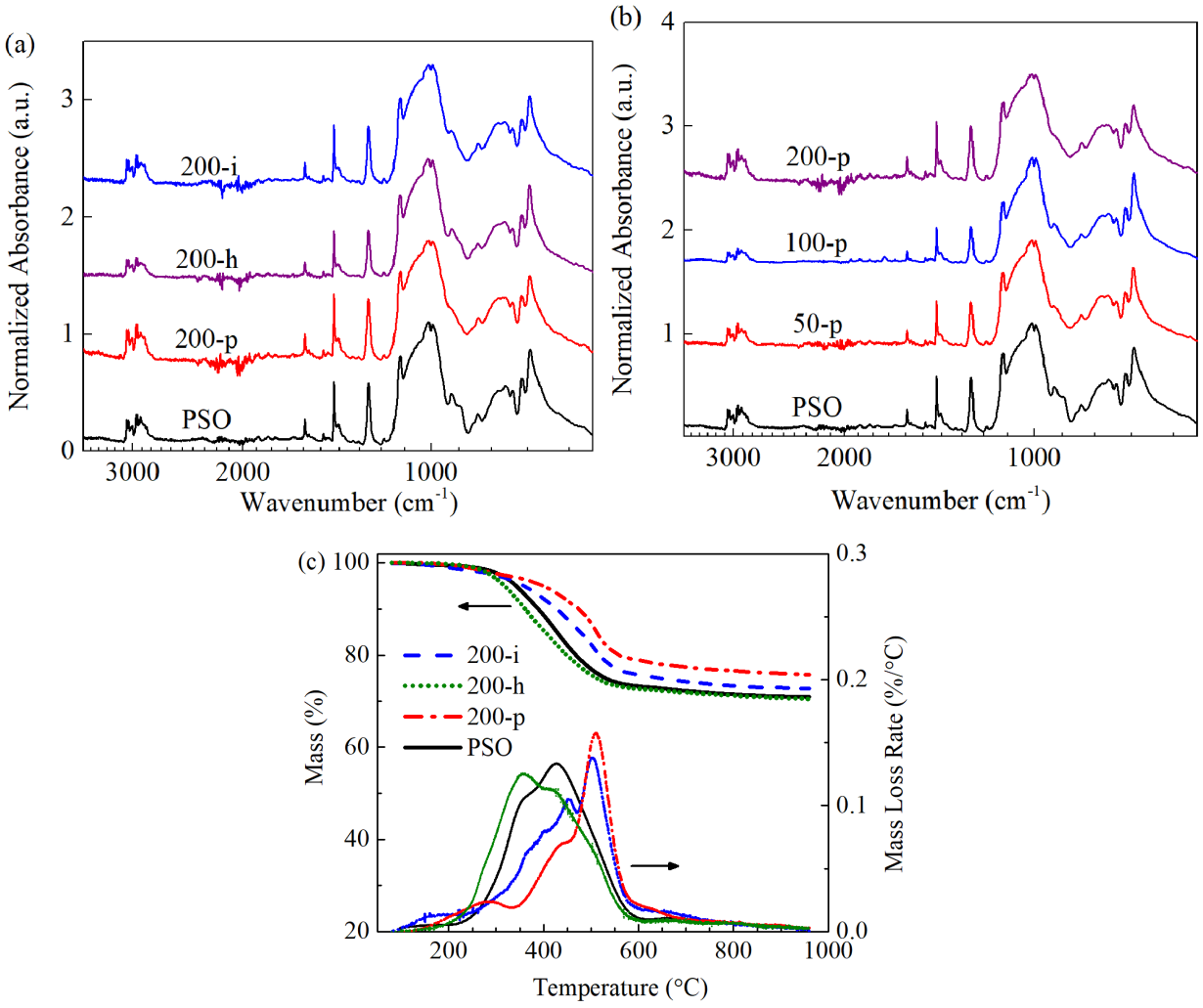

Fig. B.2 FT-IR spectra for the polymer precursors after crosslinking. (a) 200 vol% solvents, and (b) three solvent amounts for 3-pentanone. (c) TGA and dTG of 200 vol% solvent samples.

TGA of the PSO and dried 200 vol% solvent samples was conducted to determine the presence of residual trapped solvent (Figure B.2(c)). For linear polysiloxanes, thermal decomposition first begins at temperatures ~ 350°C due to depolymerization of the siloxane chain forming volatile cyclic siloxane species [25, 26]. Thus, any significant mass loss before 350°C can be attributed to residual solvent trapped within the polymer after drying. From the dTG in Figure 2c, it is apparent that all 200 vol% solvent samples display a slight mass loss between 50°C – 300°C, although the total mass loss for all samples at 300°C is only ~ 3%. Thus, although the residual solvent could not be detected using FT-IR-ATR, TGA shows that there is a small concentration of solvent remaining in the polymers after drying.

Another finding from the thermal decomposition behavior of the polymers in Figure 2c is that n-heptane decreases the overall thermal stability of the PSO, causing a mode peak in the dTG at a ~350°C rather than at ~450°C for the pure PSO. Further, the isobutylbenzene and 3-pentanone increase the thermal stability of the PSO polymer, both increasing the dTG peak mode to 500°C. Typically, an increase in thermal stability of polymers can be attributed to an increase in the crosslink density, due to either chemical bonds or physical entanglements [27, 28]. Given that the solvents do not appreciably change the chemical bonding within the polymers (Figure 2a), the increased thermal stability produced by isobutylbenzene and 3-pentanone is due either to the solvents encouraging physical entanglements during crosslinking or any solvent remaining trapped within the polymer having some synergistic effect on the PSO polymer stability.

Fig. B.3(a) shows the XRD patterns for the pyrolyzed SiOC samples. All the samples show an amorphous SiO_2 halo centered around ~22° [29]. In addition, all the samples exhibit a peak at approximately 44°, corresponding to the (100) plane of turbostratic carbon [29-32]. The 200 vol% conditions for each of the three solvents also display β-SiC peaks at 35.6°, 60°, and 72°, which is not seen for the pure PSO sample. No α-SiC is observed in any of the samples, consistent with previous studies using the same PSO precursor [20, 21, 33]. The 3-pentanone sample shows the greatest amount of SiC, and the isobutylbenzene shows the least SiC formation for the three solvents. Additionally, the peak at 22° is shifted to ~23.5° for the 200-p sample (as shown by the dashed line in Fig. B.3(a). Likely, the lower content of SiO_2 within the 200-p sample leads to the more prominent (002) peak of the turbostratic carbon at ~26° [21, 32] and causes the observed peak shift. A similar shift has been observed for SiOC ceramics after etching out SiO_2 with hydrofluoric acid [20, 21, 33, 34].

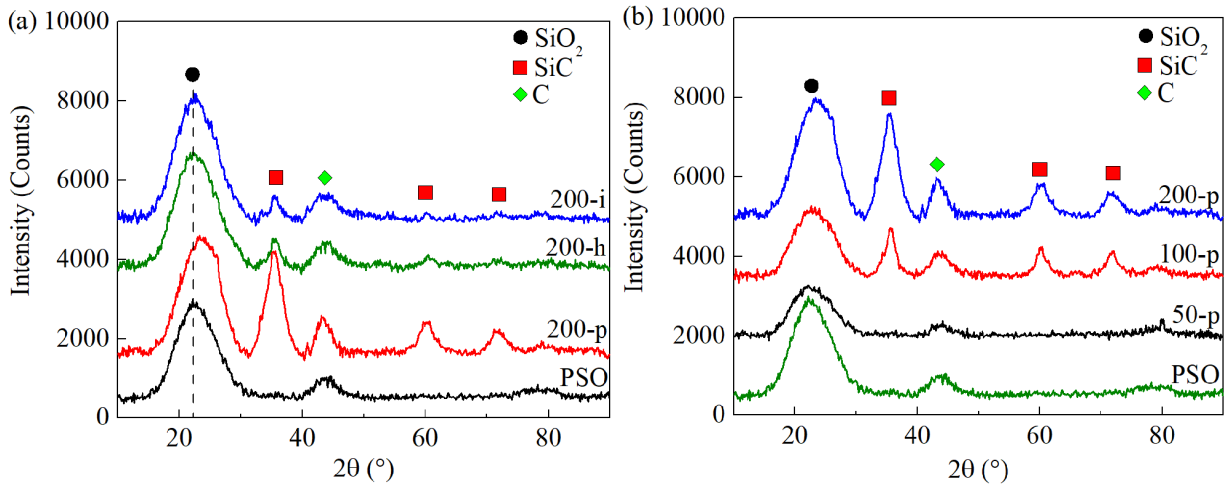

Fig. B.3 XRD patterns for the PSO samples with different solvents after pyrolysis at 1300°C. (a) 200 vol% for each solvent, and (b) different amounts for 3-pentanone.

The XRD patterns for the samples with 50, 100, and 200 vol% 3-pentanone are shown in Fig. B.3(b). The 50-p sample shows diffraction peaks similar to the PSO sample. However, with the addition of 100 vol% or 200 vol% 3-pentanone, the sample shows significant formation of SiC.

The fracture surfaces of the pyrolyzed SiOC samples with 200 vol% solvents are shown in Fig. B.4. All of the fracture surfaces show identical, featureless microstructures despite the differences in phase composition. This is to be expected due to the nanostructure of SiOC, in which the various phases have only single nanometer sizes [19, 35-37]. Thus, the SEM images of the fracture surfaces confirm that the microstructure for the SiOC samples remains in the nanometer size range despite the addition of the various solvents.

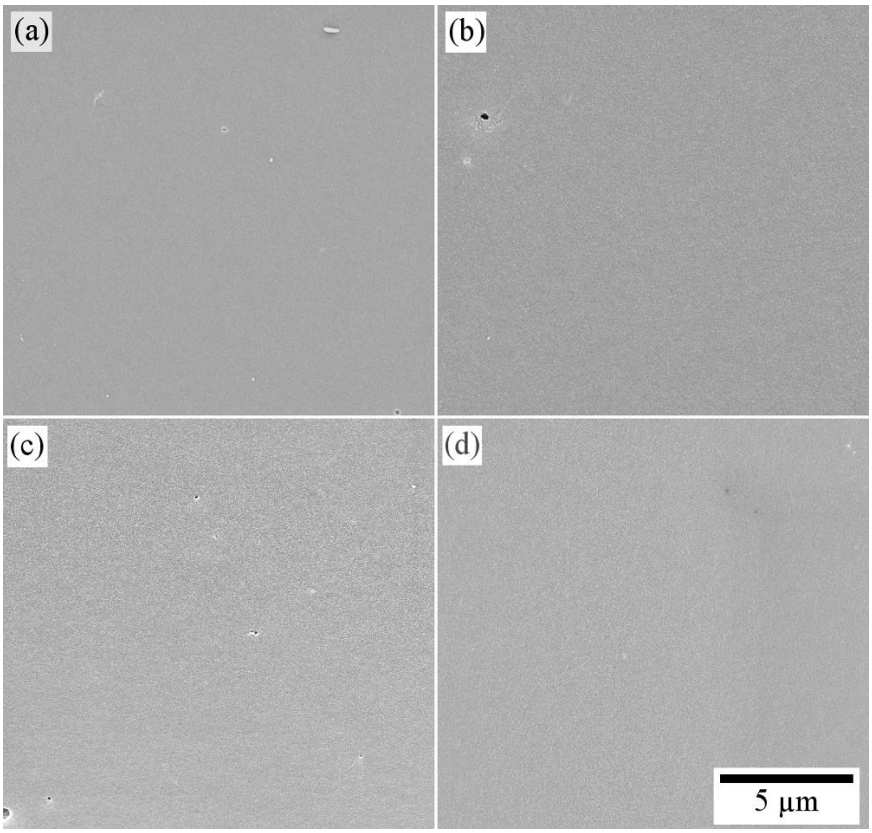

Fig. B.4 Fracture surfaces of the SiOC samples pyrolyzed at 1300°C with (a) PSO, (b) 200-p, (c) 200-h, and (d) 200-i. All images are at the same magnification.

B.4.3 Fundamental Understanding

The preferential formation of β-SiC vs. SiO_2 for the samples with 200 vol% solvents could be due to an increase in carbon from retained solvent molecules based on Eq. (B.2). The presence of the SiO_2, SiC, and carbon diffraction peaks for the samples after pyrolysis occurs due to the phase separation of SiOC, as well as the carbothermal reduction of SiO_2 into SiC. The main reactions that produce SiO_2, SiC, and C within the ceramics are given by [36, 38]:

$$2SiOC \rightarrow SiO_2(\text{amorphous}) + SiC(\beta) + C \quad \text{(B.1)}$$

$$SiO_2(\text{amorphous}) + 3C \rightarrow SiC(\beta) + 2CO\uparrow \quad \text{(B.2)}$$

The fundamental reason for the increased SiC formation when the solvents are used can be understood based on the diffusion and penetration of the solvents in-between the PSO chains, as illustrated in Fig. B.5. 3-pentanone has the smallest molecular volume of the three solvents (3-pentanone: 0.18 nm^3, n-heptane: 0.24 nm^3, isobutylbenzene: 0.26 nm^3), so it would most easily

diffuse within the PSO polymer, be trapped during drying, and thus be retained during pyrolysis. The 3-pentanone molecules would then supply additional carbon and facilitate SiC formation following Eq. (B.2). For n-heptane and isobutylbenzene, their larger sizes hinder their ability to efficiently penetrate in-between polymer chains, likely causing more of the solvent to be lost during drying. At the same time, it should be understood that the trapped solvent amount on the sample surface must be small, as it is undetectable by FT-IR (Fig. B.2). Thus, intimate mixing of the residual solvent with the polymer chains becomes a key factor. Such effect does not directly translate to macroscopic properties as discussed in Section B.4.1.

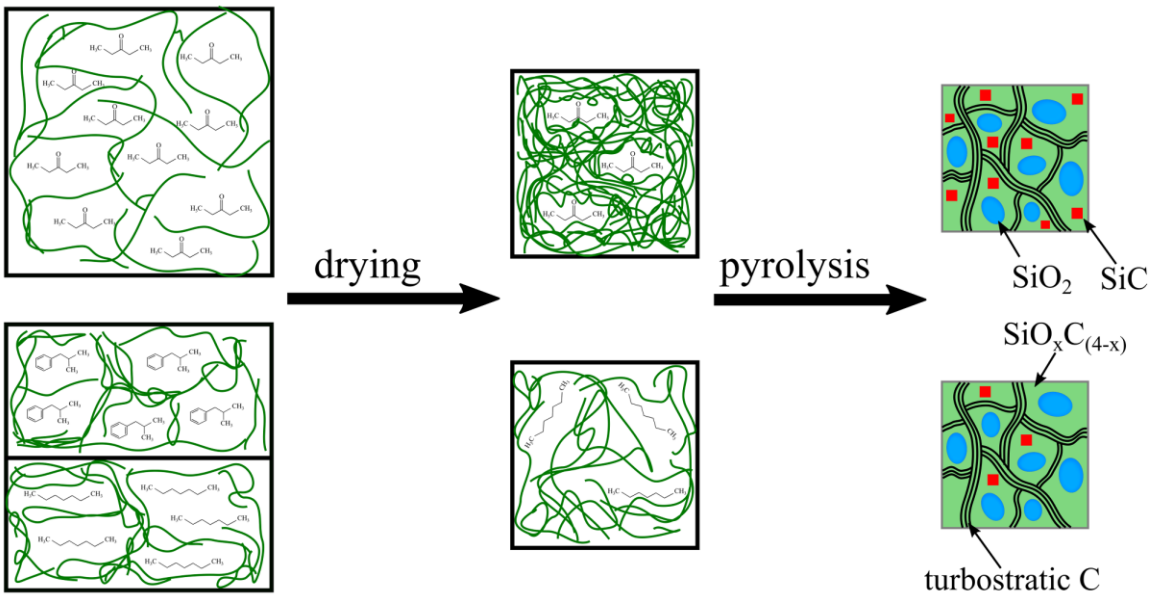

Fig. B.5 Solvent size effect on its ability to penetrate between polymer chains, remain within the polymer after drying, and affect SiC formation.

The more dominant influence of 3-pentanone in forming SiC compared to the other two solvents is shown in Fig. B.6, which displays the integrated area percentages for SiO_2 (21.6°), SiOC (22.7°), SiC (35.6°, 60°, 72°), and C (26°, 43°) for the PSO and 200 vol% solvent samples. It should be noted that the data in Fig. B.6 are not meant as a quantitative measure of the actual phase compositions due to the largely amorphous nature of the SiOC but rather a means to compare the relative phase compositions between the samples. All of the solvent-containing samples contain much less free C, close to half of the C content in the PSO sample. The 200-p sample has the highest SiC content and the lowest SiO_2 and SiOC contents. The 200-h and 200-i samples

contain similar SiOC content; the smaller size n-heptane sample contains more SiC as well as less free C and SiO_2, consistent with the proposed mechanism in Fig. B.5 and Eqs. (B.1) and (B.2).

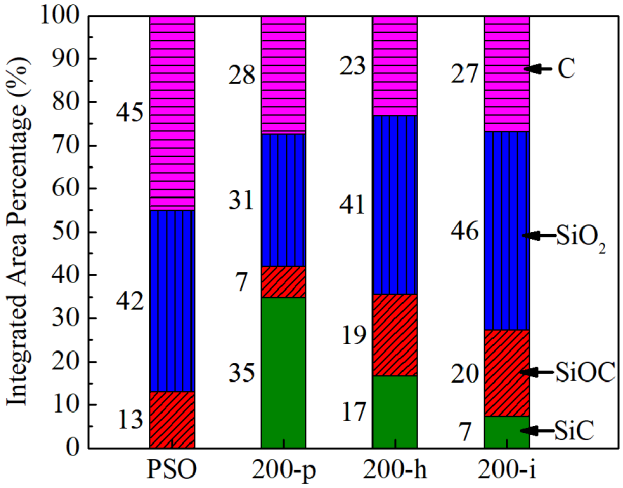

Fig. B.6 XRD intensity ratios of SiO_2 (21.6°), SiOC (22.7°), SiC (35.6°, 60°, 72°), and C (26°, 43°) for the PSO and 200 vol% solvent samples after 1300°C pyrolysis.

B.5 Conclusions

The crosslinking of polysiloxane-based polymers with different solvents and solvent concentrations has been investigated. Compared to the sample crosslinked with no solvent, most of the solvent-containing samples show a decrease in bulk density and an increase in porosity. The presence of the solvents during crosslinking encourages the formation of nanocrystalline SiC, which is absent in the pure PSO sample. The SiC formation is more prominent when high concentrations of solvents are used. Additionally, the SiC formation is dependent on the size of the solvent molecules, with smaller solvent molecules leading to more SiC formation. Based on the concentration and molecular size, the SiC formation can be linked to the retention of the solvent in the crosslinked polymer after drying.

References

1. Colombo P, Mera G, Riedel R, Soraru GD. Polymer-derived ceramics: 40 years of research and innovation in advanced ceramics. *J Am Ceram Soc* **2010**, *93*, 1805-1837.

2. Lu K, Erb D, Liu M. Thermal stability and electrical conductivity of carbon-enriched silicon oxycarbide. *J Mater Chem C* **2016**, *4*, 1829-1837.
3. Lu K, Erb D, Liu MY. Phase transformation, oxidation stability, and electrical conductivity of TiO_2-polysiloxane derived ceramics. *J Mater Sci* **2016**, *51*, 10166-10177.
4. Juttke Y, Richter H, Voigt I, Prasad RM, Bazarjani MS, Gurlo A, Riedel R. Polymer derived ceramic membranes for gas separation. *Chem Eng Trans* **2013**, *32*, 1891-1896.
5. Dibandjo P, Graczyk-Zajac M, Riedel R, Pradeep VS, Soraru GD. Lithium insertion into dense and porous carbon-rich polymer-derived SiOC ceramics. *J Eur Ceram Soc* **2012**, *32*, 2495-2503.
6. Pradeep VS, Ayana DG, Graczyk-Zajac M, Soraru GD, Riedel R. High rate capability of SiOC ceramic aerogels with tailored porosity as anode materials for Li-ion batteries. *Electrochim Acta* **2015**, *157*, 41-45.
7. Torrey JD, Bordia RK. Mechanical properties of polymer-derived ceramic composite coatings on steel. *J Eur Ceram Soc* **2008**, *28*, 253-257.
8. Rouxel T, Massouras G, Soraru GD. High temperature behavior of a gel-derived SiOC glass: Elasticity and viscosity. *J Sol-Gel Sci Technol* **1999**, *14*, 87-94.
9. Smitha S, Shajesh P, Aravind PR, Kumar SR, Pillai PK, Warrier KGK. Effect of aging time and concentration of aging solution on the porosity characteristics of subcritically dried silica aerogels. *Microporous Mesoporous Mater* **2006**, *91*, 286-292.
10. Liu C, Meng XY, Zhang XH, Hong CQ, Han JC, Han WB, Xu BS, Dong S, et al. High temperature structure evolution of macroporous SiOC ceramics prepared by a sol-gel method. *Ceram Int* **2015**, *41*, 11091-11096.
11. Liu CL, Chen HXZ, Komarneni S, Pantano CG. High surface area SiC/silicon oxycarbide glasses prepared from phenyltrimethoxysilane-tetramethoxysilane gels. *J Porous Mater* **1995**, *2*, 245-252.
12. Sasikumar PVW, Zera E, Graczyk-Zajac M, Riedel R, Soraru GD. Structural design of polymer-derived SiOC ceramic aerogels for high-rate Li ion storage applications. *J Am Ceram Soc* **2016**, *99*, 2977-2983.
13. Tamayo A, Rubio J, Rubio F, Oteo JL, Riedel R. Texture and micro-nanostructure of porous silicon oxycarbide glasses prepared from hybrid materials aged in different solvents. *J Eur Ceram Soc* **2011**, *31*, 1791-1801.

14. Tamayo A, Rubio F, Rubio J, Oteo JL. Surface and structural modification of nanostructured mesoporous silicon oxycarbide glasses obtained from preceramic hybrids aged in NH_4OH. *J Am Ceram Soc* **2013**, *96*, 323-330.
15. Tamayo A, Rubio J. Structure modification by solvent addition into TEOS/PDMS hybrid materials. *J Non-Cryst Solids* **2010**, *356*, 1742-1748.
16. Blum Y, Soraru GD, Ramaswamy AP, Hui D, Carturan SM. Controlled mesoporosity in SiOC via chemically bonded polymeric "spacers". *J Am Ceram Soc* **2013**, *96*, 2785-2792.
17. Wan JL, Gasch MJ, Mukherjee AK. In situ densification behavior in the pyrolysis consolidation of amorphous Si-N-C bulk ceramics from polymer precursors. *J Am Ceram Soc* **2001**, *84*, 2165-2169.
18. Janakiraman N, Aldinger F. Fabrication and characterization of fully dense Si-C-N ceramics from a poly (ureamethylvinyl) silazane precursor. *J Eur Ceram Soc* **2009**, *29*, 163-173.
19. Martinez-Crespiera S, Ionescu E, Kleebe HJ, Riedel R. Pressureless synthesis of fully dense and crack-free SiOC bulk ceramics via photo-crosslinking and pyrolysis of a polysiloxane. *J Eur Ceram Soc* **2011**, *31*, 913-919.
20. Erb D, Lu K. Additive and pyrolysis atmosphere effects on polysiloxane-derived porous SiOC ceramics. *J Eur Ceram Soc* **2017**, *37*, 4547-4557.
21. Li JK, Lu K. Highly porous SiOC bulk ceramics with water vapor assisted pyrolysis. *J Am Ceram Soc* **2015**, *98*, 2357-2365.
22. Aravind PR, Soraru GD. Porous silicon oxycarbide glasses from hybrid ambigels. *Microporous Mesoporous Mater* **2011**, *142*, 511-517.
23. Rumble JR. CRC handbook of chemistry and physics. 98th ed. Boca Raton, FL: CRC Press/Taylor & Francis; 2005.
24. Halim M, Hudaya C, Kim AY, Lee JK. Phenyl-rich silicone oil as a precursor for SiOC anode materials for long-cycle and high-rate lithium ion batteries. *J Mater Chem A* **2016**, *4*, 2651-2656.
25. Peña-Alonso R, Sorarù GD, Raj R. Preparation of ultrathin-walled carbon-based nanoporous structures by etching pseudo-amorphous silicon oxycarbide ceramics. *J Am Ceram Soc* **2006**, *89*, 2473-2480.

26. Wilson AM, Zank G, Eguchi K, Xing W, Yates B, Dahn JR. Pore creation in silicon oxycarbides by rinsing in dilute hydrofluoric acid. *Chem Mater* **1997**, *9*, 2139-2144.
27. Pena-Alonso R, Mariotto G, Gervais C, Babonneau F, Soraru GD. New insights on the high-temperature nanostructure evolution of SiOC and B-doped SiBOC polymer-derived glasses. *Chem Mater* **2007**, *19*, 5694-5702.
28. Li ZQ, Lu CJ, Xia ZP, Zhou Y, Luo Z. X-ray diffraction patterns of graphite and turbostratic carbon. *Carbon* **2007**, *45*, 1686-1695.
29. Li JK, Lu K, Lin TS, Shen FY. Preparation of micro-/mesoporous SiOC bulk ceramics. *J Am Ceram Soc* **2015**, *98*, 1753-1761.
30. Dibandjo P, Dire S, Babonneau F, Soraru GD. New insights into the nanostructure of high-C SiOC glasses obtained via polymer pyrolysis. *Glass Technol: Eur J Glass Sci Technol, Part A* **2008**, *49*, 175-178.
31. Saha A, Raj R, Williamson DL. A model for the nanodomains in polymer-derived SiCO. *J Am Ceram Soc* **2006**, *89*, 2188-2195.
32. Kleebe HJ, Turquat C, Soraru GD. Phase separation in an SiCO class studied by transmission electron microscopy and electron energy-loss spectroscopy. *J Am Ceram Soc* **2001**, *84*, 1073-1080.
33. Blum YD, Macqueen DB, Kleebe H-J. Synthesis and characterization of carbon-enriched silicon oxycarbides. *J Eur Ceram Soc* **2005**, *25*, 143-149.
34. Saha A, Raj R. Crystallization maps for SiCO amorphous ceramics. *J Am Ceram Soc* **2007**, *90*, 578-583.